INVESTIGATING MECHANISMS OF TRANSIENT RECEPTOR POTENTIAL REGULATION WITH NUCLEAR MAGNETIC RESONANCE AND ROSETTA COMPUTATIONAL BIOLOGY

by

Nicholas J. Sisco

A Dissertation Presented in Partial Fulfillment
of the Requirements for the Degree
Doctor of Philosophy

Approved November 2018 by the
Graduate Supervisory Committee:

Wade D. Van Horn, Chair
Jeremy H. Mills
Xu Wang
Jeff L. Yarger

ARIZONA STATE UNIVERSITY

December 2018

ABSTRACT

The physiological phenomenon of sensing temperature is detected by transient receptor (TRP) ion channels, which are pore forming proteins that reside in the membrane bilayer. The cold and hot sensing TRP channels named TRPV1 and TRPM8 respectively, can be modulated by diverse stimuli and are finely tuned by proteins and lipids. PIRT (phosphoinositide interacting regulator of TRP channels) is a small membrane protein that modifies TRPV1 responses to heat and TRPM8 responses to cold. In this dissertation, the first direct measurements between PIRT and TRPM8 are quantified with nuclear magnetic resonance and microscale thermophoresis. Using Rosetta computational biology, TRPM8 is modeled with a regulatory, and functionally essential, lipid named PIP_2. Furthermore, a PIRT ligand screen identified several novel small molecular binders for PIRT as well a protein named calmodulin. The ligand screening results implicate PIRT in diverse physiological functions. Additionally, sparse NMR data and state of the art Rosetta protocols were used to experimentally guide PIRT structure predictions. Finally, the mechanism of thermosensing from the evolutionarily conserved sensing domain of TRPV1 was investigated using NMR. The body of work presented herein advances the understanding of thermosensing and TRP channel function with TRP channel regulatory implications for PIRT.

DEDICATION

To my Family.

ACKNOWLEDGMENTS

I am thankful to my committee members for their guidance throughout my career and the members of the Van Horn lab for their scientific collaboration. I also want to thank Brian Cherry and Samrat Amin whose assistance was greatly appreciated through my graduate studies. Additionally, like to thank the Arizona State University Graduate College for their support through the Completion Fellowship.

I would especially like to acknowledge my wife, Rhysa Sisco, for providing solid support throughout my graduate studies, for which none of this would have been possible.

TABLE OF CONTENTS

Page

LIST OF TABLES

Table Page

LIST OF FIGURES

Figure Page

Figure Page

CHAPTER 1

General Introduction

1.1 Transient Receptor Potential Ion Channel Overview

The membrane bilayer acts as a biological capacitor, which can be discharged through the function of specialized proteins residing in the membrane bilayer. This voltage discharge provides cells the driving force for many physiological functions. An electrochemical gradient is established through the action of the sodium and potassium ATPase, which uses ATP to transport two potassium ions intracellularly while concomitantly pumping out three sodium ions for a net negative intracellular charge. In response to a stimulus, this negative charge is discharged with an ion channel membrane protein by opening a pore that allows ions to pass through. While the transporter class of membrane protein typically uses energy to force ions or molecules against a gradient, ion channels typically use mass action or diffusion to pass ions through the membrane. Gating is the action of the ion channel that causes it to open its pore and conductance is

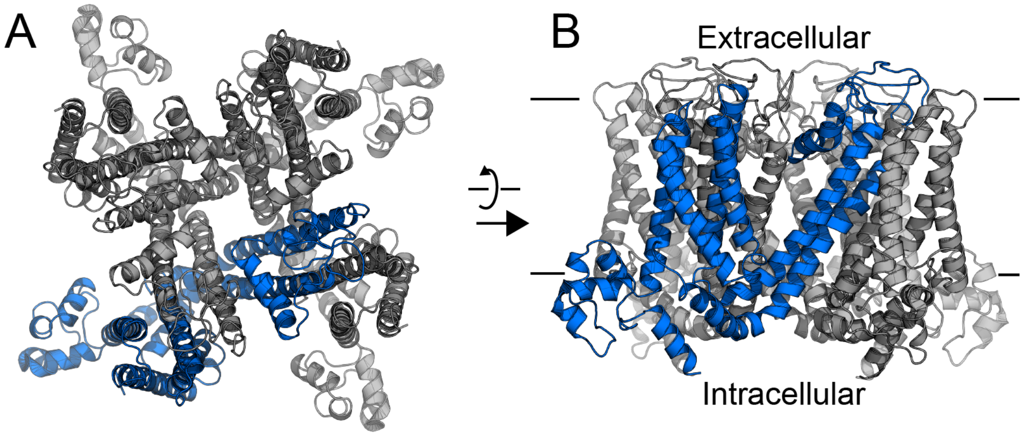

Figure 1.1 The structure of TRPM8 is an axially C4 symmetric ion channel tetramer. A) The channel is oriented from the top looking into the cell through the ion channel pore, which is formed by folding monomers (colored blue) in a domain swapped architecture. B) Flipped 90° to show the orientation of the channel from the view of the membrane bilayer plane.

the flow of ions that are allowed to pass. These ion channels can have altered conductance in response to many different stimuli, but the molecular mechanisms of these ion channels are still an active area of investigation owing to the complexity of channel gating. The primary focus of this dissertation will be an investigation into the molecular details of a specific modulatory protein, PIRT and how it affects a specific ion channel, TRPM8.

Transient receptor potential (TRP) ion channels are a family of membrane proteins that share structural features with voltage-gated ion channels; both comprise six transmembrane α-helices per monomer, with a C4 symmetric tetramer quaternary structure along the central axis (Figure 1.1). Shared across all TRP channels, the structural transmembrane domains comprise a pore domain flanked by sensing domains, which is conserved from voltage-gated potassium channels.

The general mechanism for voltage-gated potassium channel activation relies on the positively charged S4 α-helix that translates away from the extracellular space,

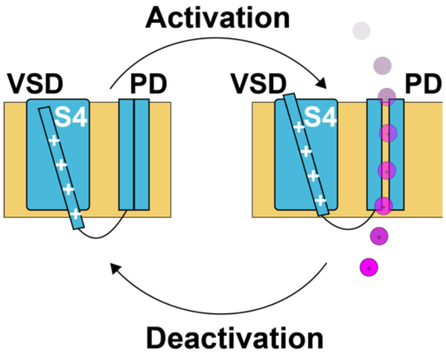

Figure 1.2 Simplified General Mechanism for Voltage-Gated Ion Channels. This cartoon shows the mechanism of action that opens voltage gated ion channels. This mechanism utilizes positively charge amino acids along the S4 helix within the voltage sensing domain (VSD), which opens the tetrameric pore domain (PD) allowing ion flux.

perpendicular to the membrane plane. Coupled to the pore domain, the voltage sensing domain pulls open the pore and thereby opens the channel (Figure 1.2, activation curve).[1] As the Na/P-ATPase repolarizes the cell, the S4 returns to the original position by sliding back down intracellularly following the positive charge inside rule (Figure 1.2, deactivation curve). While TRP channels share structural homology with the potassium channels, the mechanism of action for TRP channel gating is not as well understood.

Functionally, most TRP ion channel family members are polymodally modulated by diverse stimuli and TRPM8 functions in sensory physiology as the primary human cold sensor but has also been implicated in pain, cancer, and obesity.[2-6] TRPM8 is a weakly voltage sensitive nonselective cation channel that is calcium permeable and gates in response to physiologically relevant cold temperatures, the cooling chemical compounds menthol and icilin, changes in intracellular pH, cholesterol, and phosphatidylinositol 4,5-bisphosphate (PIP$_2$) concentrations (Figure 1.3).[7-10] Additionally, TRPM8 function is modulated by proteins including calmodulin (CaM) and PIRT (*p*hosphoinositide

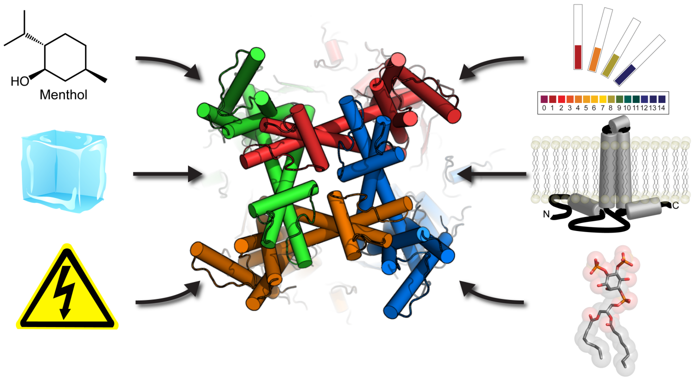

Figure 1.3 The general topology of TRPM8. TRPM8, shown in the center, can be modulated by exogenous ligands like menthol, changes in temperature or voltage, pH sensitivity, subunit proteins like PIRT (see main text), and endogenous lipids and lipid-like molecules such as PIP$_2$ or cholesterol.

*i*nteracting *r*egulator of *T*RPs), which is a small modulatory membrane protein.[7, 8, 11-13]

PIRT is a phosphoinositide binding α-helical membrane protein comprising two transmembrane (TM) helices with intracellular N- and C-termini. PIRT is expressed primarily in the dorsal root and trigeminal ganglia of the peripheral nervous system where it has been shown to modulate mouse temperature sensitivity via interactions with the cold-sensing TRPM8 and the heat-sensing TRPV1 ion channels.[14, 15] Additionally, PIRT–TRPV1 (TRPV1 is the heat sensing TRP channel) interactions have been functionally implicated in histaminergic and nonhistaminergic pruritus (itch) and uterine contraction pain in mice under oxytocin insult.[16, 17] Additionally, recent studies suggest that PIRT modulates function in non-TRP ion channels; for example, it is coexpressed with P2X2 channels in the enteric nervous system and has been reported to endogenously inhibit P2X3 currents to reduce bladder overactivity.[18, 19] Currently, all channels reported to be regulated by PIRT are known to also interact with phosphoinositol (4,5) bisphosphate (herein referred to as PIP_2) and since the identification of PIRT in 2008 by Dong et al., it has been implicated in a variety of physiological contexts.[14] Despite the emerging details on PIRT as a subunit for other membrane proteins, little is known about the molecular mechanisms that underlie PIRT ion channel regulation. Throughout this dissertation, hPIRT is meant to signify research that is specifically from human variants of PIRT, whereas PIRT without a species indication is meant to signify knowledge of PIRT in general where species differences are unknown.

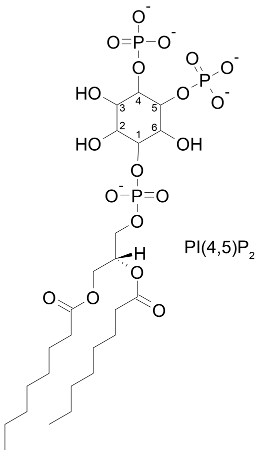

Figure 1.4 The phosphoinositol (4,5) bisphosphate structure. While the chain lengths of PIP_2 can change depending on location within cellular compartment, the chemical composition of the head group comprises an inositol bound to three phosphates at 1, 4, and 5 positions of the inositol ring.

The inner leaflet of mammalian lipid bilayers comprises ca. 1% PIP_2 (Figure 1.4),[20] where it functions as a signaling and modulatory lipid interacting with a wide variety of integral membrane proteins.[21-23] With a few exceptions,[24, 25] the experimentally determined molecular details of PIP_2 binding have remained obscure despite an abundance of functional data showing wide-ranging physiological roles that PIP_2 and other phosphoinositides play.[21, 22, 24, 26] PIP_2 binding proteins typically share a collection of basic amino acids such as arginine or lysine that are thought to bind to the anionic head of these lipids.[22, 23, 27] Proteins like syntaxin-1A and MARCKS (Myristoylated alanine-rich C-kinase substrate) bind, and sequester, PIP_2 creating formations of possible lipid domains made of phosphoinositides similar to cholesterol lipid rafts.[23, 27] With molecular dynamics simulations and super resolution microscopy, syntaxin-1A was shown to enrich these lipid domains with phosphoinositides from 1% to between 3% and 6% total lipids.[23] Similar to syntaxin-

1A and MARCKS, the poly basic amino acid features from these phosphoinositide binding proteins are found in the TRP channel subunit protein PIRT, which has been previously shown to bind phosphoinositides using a shortened construct of PIRT that preserve amino acids from the bottom of TM2 to the C-terminus.[11, 14] Confounding these results; however, is evidence that shortened PIRT may lead to non-functional protein.[28]

Phosphoinositides have been shown to modulate ion channels for decades now, and past studies of specific PIP_2 lipid interactions with membrane proteins show that they bind to, activate, or deactivate ion channels in similar ways where PIP_2 acts as a dynamic membrane anchor stabilizing multiple conformations.[21, 24, 29, 30] Structural studies of the Kir2.2 channel illustrated seminal mechanisms for how PIP_2 binds and experimentally showed how it activated Kir2.2 by directly binding to it and stabilizing the open state.[24] Likewise, human EAG1 (Kv10.1) ion channels utilize PIP_2 to adhere the calcium calmodulin associated EAG domain to the membrane bilayer inner leaflet, promoting several intramolecular domain interactions, and finally causing the channel to close.[30] Recent molecular details of the two pore channel TPC1 structure show another example of how an ion channels utilize a bound phosphoinositide to enhance gating.[31] TPC1 is specific for $PI(3,5)P_2$ and uses the lipid as a cofactor-like molecule by binding to basic residues to stabilize the channel in a conformation that predisposes it to gate under changes in voltage and diminishes gating when $PI(3,5)P_2$ is absent.[31] Similar to TPC1, the TRPM8 mechanism that is thought use PIP_2 to potentiate channel gating.[32] The KCNQ2 voltage-gated potassium ion channel has two PIP_2 binding sites, which have been reported to be conformational state dependent; one PIP_2 binding site in the S2-S3 linker is occupied when the channel is closed and a second site in the S4-S5 linker is occupied, presumably stabilizing the channel when opened.[25] State-dependent and dynamic binding appears to be an emerging role of PIP_2 and our results show that specific and direct overlapping interactions between PIRT, PIP_2, and TRPM8 could cause channel gating to be influenced by shuttling of PIP_2 between alternate binding sites.

In this dissertation, the molecular details of PIRT:PIP_2, PIRT:TRPM8, and PIRT:calmodulin interactions are investigated using a combination of structural biology, computation, and biochemistry. The conclusions herein suggests novel regulatory mechanisms for TRP channels with potentially increased understanding of ion channel regulation in general.

1.2 Nuclear Magnetic Resonance Spectroscopy

1.2.1 General Overview of Nuclear Magnetic Resonance Spectroscopy

Nuclear magnetic resonance (NMR) spectroscopy is a powerful tool that can be used to investigate biological systems. With respect to solution state NMR, the magnetic field of the spectrometer allows researchers to exploit energy differences between spin states of spin ½ nuclei, which include, but is not limited to, ^{1}H, ^{15}N, and ^{13}C. Amino acids polymerize to form the protein amide backbone and can be isotopically enriched in lab with ^{15}N and ^{13}C, which can be interrogated in the NMR spectrometer to provide atomically explicit structural information. One of the most common experiments for protein NMR is the ^{1}H-^{15}N heteronuclear single quantum coherence (HSQC) experiment, where the spectroscopic data collected couples the proton and nitrogen of the amide bond, and provides researchers with amino acid specific information. Signals are converted from the time domain to the frequency domain using a Fourier transform where the resonance frequencies of the interrogated nuclei report the electronic structure of the coupled nuclear spin systems, i.e. H-N bond spin system for this case. In a structured environment, e.g. in a folded protein, the H-N bond of the amino acid exists in unique structural environments relative to other amino acids and the resonances are not degenerate, which makes the HSQC spectrum different for each protein.

The HSQC is the first step in structure determination of proteins using NMR by using a multitude of experiments that couple the H-N bond to the backbone C_α, C_β, and C' atoms. The resonance assignments can then be used to calculate dihedral angles for the protein backbone using software like TALOS-N;[33] however, the assigned HSQC spectrum can also be used in experiments that monitor ligand-dependent chemical shift perturbations,[34] distance information for structure determination,[35] and other experiments measuring protein dynamics.[36-38] Herein, NMR was used to assign the backbone resonances of two membrane proteins and used to: map binding sites from ligand-dependent chemical shift perturbations, extract distance restraints for structure predictions, and quantify thermodynamic information from resonance intensities.

1.2.2 Characterization of Ligand Binding Using NMR

The ligand-dependent chemical shift perturbation can be used to calculate ligand binding affinities to proteins. The reversibility of a protein P binding to the ligand L can be described by:

$$P + L \leftrightarrow PL$$

where the protein:ligand complex PL is in dynamic equilibrium. The equilibrium rate constants k_{on} and k_{off} describe the forward and back reactions where the dissociation constant K_d is equal to [P][L]/[PL], where brackets represent the concentrations of the protein, ligand, and protein:ligand complex. The K_d can be thought of the concentration of the titrant at which half of the available binding sites are occupied. One important aspect of the K_d is that when the system is at equilibrium the K_d can be described by:

$$K_d = \frac{k_{on}[P][L]}{k_{off}[PL]}$$

which implies that K_d is equal to k_{on}/k_{off} at equilibrium. For targets that have sterically available binding sites, the binding can be considered diffusion-controlled where the on rate (k_{on}) is ca. 10^9 M^{-1} s^{-1} and the off rate (k_{off}) is thusly ca. 10^9 and unitless. With NMR-detected ligand binding experiments, if the off rate is slower than the resonance frequencies between the bound and the free state in a titration, the signal for the free state gradually decreases and the bound state increases concomitantly. This type of chemical shift perturbation is called slow-exchange. The fast exchange system is more commonly observed in ligand binding NMR with the off rate much greater than the chemical shift change and therefore the chemical shift is perturbed smoothly throughout the titration.[34]

In a practical titration, the researcher typically knows the ligand and protein concentrations, which can be written with mass balance equations:

$$[L_t] = [L] + [PL] \text{ and } [P_t] = [P] + [PL]$$

where the total concentration of the ligand [L_t] and protein [P_t] in the titration are a sum of the free ([L] or [P]) and bound [PL] states. Considering the fast exchange limit, the observed chemical shift, δ_{obs}, is the chemical shift-weighted average of the fractional-free and -bound states, *f_b* and *f_b* respectively:

$$\delta_{obs} = \delta_f f_f + \delta_b f_b$$

Since the sum of the fractions are equal to one:

$$f_b = \frac{\left(\delta_{obs} - \delta_f\right)}{\left(\delta_b - \delta_f\right)}$$

This equation can be rewritten to arrive at the following expression:

$$\Delta\delta_{obs} = \frac{\Delta\delta_{max}\left\{([P]_t + [L]_t + K_d) - [([P]_t + [L]_t + K_d)^2 - 4[P]_t[L]_t]^{\frac{1}{2}}\right\}}{2[P]_t}$$

relating the total ligand [L_t] at a given chemical shift perturbation, total protein [P_t], max change in chemical shift $\Delta\delta_{max}$, and the relative chemical shift change $\Delta\delta_{obs}$ referenced to the free chemical shift, i.e. $\Delta\delta_{obs} = \Delta\delta_{b,i}$ -$\Delta\delta_f$ where *i* is the chemical shift upon titrant addition. While more rigorous, this equation can be approximated with the adsorption model:

$$\Delta\delta_{obs} = \frac{\Delta\delta_{max} L_t}{(K_d + L_t)}$$

with the assumption that the protein concentration has a small effect on the ligand-dependent chemical shift perturbation.

To calculate the change in chemical shift $\Delta\delta_{obs}$ in an H-N HSQC:

$$\Delta\delta_{obs} = \left((\Delta\delta_H)^2 + \left(\frac{\Delta\delta_N}{5}\right)^2\right)^{1/2}$$

where $\Delta\delta_H$ is the change in proton chemical shift and $\Delta\delta_N$ is the change in nitrogen chemical shift. [34] Quantification of the binding constant K_d for PIRT using $\Delta\delta_{obs}$ for ligands including TRPM8 and PIP_2 in Chapter 2 and calmodulin in Chapter 3.

1.2.3 Using NMR to Extract Thermodynamics from HSQC Spectra

NMR is a uniquely powerful experiment that can be used to determine atomically resolved structures and it can be used to quantify other properties of the interrogated molecule including diffusion constants or thermodynamic quantities. In Chapter 5, the heat sensing TRPV1 enthalpy are quantified using resonance intensity data from HSQC measurements. NMR resonance intensities are inversely proportional to the resonance linewidth ($\Delta\upsilon_{FWHH}$, full-width at half-height). For the Lorentzian shaped signals observed in NMR, the intensities and linewidths reflect the transverse relaxation rates (R_2) of the molecule, which can be estimated from the linewidth, $\Delta\upsilon_{FWHH} = R_2/\pi$.[39] R_2 is in turn sensitive to the dynamic properties of the protein in solution, including nanosecond timescale rotational motion, and picosecond to millisecond internal motions, including protein conformational change. Thus, NMR peak intensity should report on the conformational state of a protein.

We can then use general thermodynamic models to describe a protein that undergoes conformational change in a temperature dependent manor with an equilibrium constant defined by the ratio of molecules in state 1 to state 2:

$$K_{eq} = \frac{[State\ 1]}{[State\ 2]} = \frac{\alpha}{1-\alpha}$$

where the α term represents a measurable quantity for the probability of observing State 1, such as resonance intensity, and State 2 represented as 1-α. When State 1 and State 2 are equal, the $K_{eq} = 1$. Extending to the common relations of Gibb's free energy:

$$\Delta G = -RTln\left(K_{eq}\right)$$

$$\Delta G = \Delta H - T\Delta S$$

when $K_{eq} = 0$, $\Delta G = 0$; and we reach the identity:

$$T_{50} \stackrel{\text{def}}{=} \frac{\Delta H}{\Delta S}$$

with T_{50} described as half maximal activation temperature or melting temperature. Combining these equations, we reach:

$$K_{eq} = \exp\left(\left(\frac{\Delta H}{RT}\right)\left(\left(\frac{T}{T_{50}}\right) - 1\right)\right)$$

and with $\alpha = \frac{K_{eq}}{1+K_{eq}}$, we can replace α with resonance intensity (I) and add a maximum (I_{max}) and minimum (I_{min}) fitting parameter, finally:

$$I = \frac{(I_{max} + I_{min})\exp\left(\left(\frac{\Delta H}{RT}\right)\left(\left(\frac{T}{T_{50}}\right) - 1\right)\right)}{1 + \exp\left(\left(\frac{\Delta H}{RT}\right)\left(\left(\frac{T}{T_{50}}\right) - 1\right)\right)}$$

which is a sigmoidal relationship relating a thermodynamic change in resonance intensity as a function of temperature to the enthalpy and half maximal activation temperature.

1.2.4 Paramagnetic relaxation enhancement

Measurements of distance information for biomolecules is essential for structure determination protocols using NMR. Atom distances in NMR can be measured with the nuclear Overhauser effect (NOE) that relates a distance dependence to the spin-spin coupling of nuclei close in space and spectroscopists can make use of paramagnets that affect the relaxation rate of nuclear spins in a distance dependent manner. Notably, NOE's are challenging to measure in membrane proteins due to inherent physical limitations with NMR caused by the molecular size of the interrogated molecule making measurements of distances from paramagnetic relaxation enhancement a valuable tool for membrane protein structure determination.

Paramagnets arising from an isotropic *g*-tensors, found in systems with unpaired electrons like nitroxide spin labels or chelated Mn^{2+}, induce dipole-dipole (through space) interactions at high magnetic fields (^1H frequencies > 500 MHz) that affect the rate of relaxation of spins in proximity to the paramagnet. The observed transverse relaxation rate (R_2^{eff}) is the sum of the intrinsic relaxation rate (R_2) and paramagnetically enhanced relaxation rate (Γ_2): $R_2^{eff} = \Gamma_2 + R_2$. The distance dependence of a nucleus and an unpaired electron is given by:

$$\Gamma_2 = \frac{1}{15}\left(\frac{\mu_0}{4\pi}\right)^2 \gamma_I^2 g^2 \mu_B^2\, S(S+1) r^{-6}\left(4\tau_c + \frac{3\tau_c}{1+(\tau_c\omega_H)^2}\right)$$

where *r* is the distance between the free electron spin and the observed nucleus, *g* is the electronic g-factor , μ_0 is the vacuum permeability constant, μ_B electron Bohr magneton, τ_c is the PRE correlation time given by $\tau_c^{-1} = \tau_r^{-1} + \tau_s^{-1}$; τ_r is the rotational correlation time, τ_s is the electron relaxation time; ω_H is the nuclear Larmor frequency, γ is the gyromagnetic ratio, and S is the spin quantum number. In practice, Γ_2 is calculated by taking the difference between the measured R_2^{eff} and R_2 from proton relaxation experiments on paramagnetic and matched diamagnetic samples.

1.2.5 Residual Dipolar Coupling

Side chain distance restraints are used quite extensively to provide detailed structural information; however, with the challenges of large systems from membrane proteins these data are not always tractable. RDC restraints can add very useful restraints for structure determination providing highly sensitive structural information. By exploiting anisotropic molecular tumbling, residual dipolar coupling measurements can help molecular biologists restrain biomolecular structure determination. Dipolar coupling is a nuclear dipole-dipole interaction with an angular dependence correlated to the alignment of each nuclear spin pair to the magnetic field. Typically the dipolar coupling is not observed in solution state NMR since the alignment is averaged to zero in an isotopically tumbling molecule. Soluble molecules can be weakly aligned to induce an anisotropic tumbling using polyacrylamide, and other anisotropic inducing media, causing weak alignment to the magnetic field B_0 vector. This weak alignment allows researchers to measure the dipolar coupling of the spins from residual alignment caused by the medium, hence the name residual dipolar coupling. The dipolar coupling (D_{ij}) follows:

$$D_{ij}^{res} = -\left(\frac{\mu_0}{4\pi}\right)\frac{\gamma_i\gamma_j h}{2\pi^2 r_{ij,eff}^3}\left\langle P_2\left(\cos\left(\theta_{ij}(t)\right)\right)\right\rangle$$

where $r_{ij,eff}$ is the vibrationally corrected internuclear distance, h is Plank constant, γ is the gyromagnetic ratio of spin i or j, μ_0 is the permeability constant, and $\left\langle P_2\left(\cos\left(\theta_{ij}(t)\right)\right)\right\rangle$ is the time averaged angular term. This angular term implies that with one alignment medium, the continuum of possible internuclear vectors appears as flattened cone, i.e. one alignment medium is insufficient to reduce the *i-j* bond vectors to a single orientation. Therefore, researchers use multiple alignment media from multiple nuclear spin pairs, e.g. ^{1}H-^{15}N, ^{13}Cα-^{15}N, ^{13}C′-^{15}N, etc., to reduce these angles and provide more refined structural details. Residual dipolar couplings can therefore be used to restrain spin pairs to specific angles and provide accurate structural restraints.[40]

Measurement of RDC can be carried out in various ways. For larger proteins, there are challenges related to the molecular size and inherent loss of signal. Measuring the ^{1}H-^{15}N dipolar coupling $^{1}D_{HN}$ can be carried out using a pulseprogram called ARTSY, which is designed to measure ^{1}H-^{15}N RDC's on larger proteins.[41] Described more in Chapter 4.2.2, ARSY is a modified TROSY-HSQC (transverse relaxation optimized spectroscopy, TROSY) that alters the ^{1}H dephasing duration during the INEPT (insensitive nuclei enhanced by polarization transfer) transfer time, which is used to couple one nucleus to another. The dephasing duration *T* during INEPT alters between a reference measurement where ^{1}H dephasing is active for half of the INEPT time ($T = (2|^{1}J_{NH}|)^{-1} = 5.35$ ms) and an attenuated measurement ($T = (|^{1}J_{NH}|)^{-1} = 10.7$ ms). The resonance intensity ratio from these acquired spectra is related to the dipolar coupling between the H-N bound:

$$Q = \frac{I_A}{I_R} = \frac{\sin\left[\pi\left(\,^{1}J_{NH} - \,^{1}D_{NH}\right)T\right]}{\sin\left[\pi\left(\,^{1}J_{NH} - \,^{1}D_{NH}\right)T/2\right]}$$

Where $^{1}J_{NH} = -92$ Hz and is detailed by Fitzkee, et al. The above equation can be rewritten the above equation as:

$$^{1}D_{NH} = -\frac{1}{T} - {}^{1}J_{NH} + \left(\frac{2}{\pi T}\right)\sin^{-1}\left(\frac{Q}{2}\right)$$

which allows RDC measurements from intensity ratios of attenuate and reference spectra. The two different gels were measured with ARTSY and processed in CCPN to extract resonance intensities.[42]

1.3 Microscale Thermophoresis

There are a variety of tools that can be used to measure ligand affinity for proteins. As mentioned above, ligand-dependent chemical shift perturbations can be used to extract ligand affinity. While NMR-detected ligand binding is detected through small changes in the electronic structure, affinity measurements using microscale thermophoresis exploits thermal gradient-dependent movement of molecules that is described by the Soret coefficient. Thermophoresis was discovered in 1879 by a Swiss scientist by analyzing concentration gradients of salt in a glass tube caused by temperature differences at the ends of the tube, i.e. the salt was more concentrated at the cold end of the tube. At steady state, i.e. unvarying state, the concentration gradient of the salt is caused by the temperature gradient and can be described by the Soret effect.[43] Thermophoresis can be described as molecular flow caused by a temperature gradient:

$$j = -\rho D_T c(1-c)\nabla T$$

where j is molecular flow, c is the concentration of the molecule, D_T is the thermal diffusion coefficient, ρ is the fluid density, and ∇T is the temperature gradient. Balancing the thermal diffusion in steady state is Brownian motion described with Fick's law of diffusion:

$$j = -\rho D \nabla c$$

In the steady state, the mass flux is 0, i.e. $j = 0$, and the Soret coefficient S_t is:

$$S_T \equiv \frac{D}{D_T}$$

$$S_T \equiv \frac{1}{c(1-c)} \frac{\nabla c}{\nabla T}$$

Constant diffusion and thermal diffusion coefficients lead to the exponential depletion law:

$$\frac{c}{c_0} = \exp(-\frac{D_T}{D}(T - T_0))$$

where the concentration depends only on the temperature difference. Where now we can relate the concentrations between hot and cold with the difference in temperature and the Soret effect.[43-45]

$$\frac{c_{hot}}{c_{cold}} = \exp(-S_T\, \Delta \mathrm{T})$$

In practice, thermophoresis can be measured using a fluorescent probe covalently attached to molecule. Thermophoresis can then be used to measure the effect on molecules in a ligand free state and a ligand bound state. Thermophoresis has been used to extract dissociation constants according to a modified function for ligand binding shown above, correlating the fluorescence change from thermophoresis:

$$F_{norm} = \frac{F_{max}\left\{([P]_t + [L]_t + K_d) - [([P]_t + [L]_t + K_d)^2 - 4[P]_t[L]_t]^{\frac{1}{2}}\right\}}{2[P]_t}$$

where $F_{norm} = (1 - f_b)F_{norm,unbound} + (f_b)F_{norm,bound}$ and F is the fluorescence measured from the excitation of a conjugated fluorophore to the interrogated biomolecule. The fluorescence change from bound and unbound state depends on the Soret effect described above.

1.4 Computational Biology with Rosetta

Rosetta was originally designed to predict the structures of proteins from the protein sequence alone.[46] Since then, it has evolved to generate models of protein complexes,[47] predict structure from evolutionarily homologous proteins,[48-51] and integrate sparse experimental data from NMR[52-56] and electron cryo-microscopy[50] to generate predicted structures from otherwise challenging systems.

The success of Rosetta is in part due to the energy scoring function it uses to approximate the energy of a biomolecule fold or conformation and also from the Monte Carlo-style sampling protocols.[51, 57-59] The form of the scoring function is given as a linear combination of the energy terms E_i, which are calculated as the function of the chemical identities *aa* and the degrees of freedom in geometry (Θ) scaled by a weight function *w* for each term:

$$\Delta E_{total} = \sum_i w_i E_i(\Theta_i, aa_i)$$

Contained within the summation is energy terms for the forces of attraction and repulsion that take Van der Waals and electrostatic energies, solvation energy, orientation dependent hydrogen bonding energy, energy scoring for correct Ramachandran dihedral angles of the amide backbone, and other energy scores related to the identity of the specific amino acid.[57] The energy term is periodically optimized with the introduction of improved physical theories, structural data and observations with the most updated score function for the Rosetta energy terms is very well described and detailed by Alford, R. F. et al[57] and will not be described here. However, it is important to note the score functions used in the work described in this dissertation utilizes scoring functions that were optimized for an implicit membrane bilayer,[60] unless specifically noted otherwise.

CHAPTER 2

Competitive Interactions Between PIRT, The Cold Sensing Ion Channel Trpm8, and Pip$_2$ Suggest a Mechanism for Regulation[‡]

[‡] This chapter is under review at *Scientific Reports*.

2.1 Introduction

TRP ion channels are involved in diverse physiological and pathophysiological processes. Functionally, most TRP ion channel family members are polymodally modulated by diverse stimuli. TRPM8 functions in human sensory physiology as the primary cold sensor and is also implicated in functional roles beyond thermosensing such as pain, cancer, and obesity[2-6] and is a weakly voltage sensitive nonselective cation channel. It is calcium permeable and gates in response to physiologically relevant cold temperatures, cooling chemicals, such as menthol, changes in intracellular pH, cholesterol, and phosphatidylinositol 4,5-bisphosphate (PIP$_2$).[7-10] TRPM8 function is also regulated by modulatory proteins, including the membrane protein PIRT (*p*hosphoinositide *i*nteracting *r*egulator of *T*RPs).[10, 11, 61, 62] Modulation of TRPM8 by PIRT follows a trend found in many TRP channels where orthologs often have species dependent functional diversity.[61, 63] For the mice proteins, PIRT increases TRPM8 sensitivity to cold, menthol, and voltage; whereas, for the human proteins PIRT attenuates equivalent TRPM8 currents.[7, 8, 11-13, 61-64]

PIRT is a phosphoinositide binding α-helical membrane protein with two transmembrane (TM) α-helices with intracellular N- and C-termini. It is expressed primarily in the dorsal root and trigeminal ganglia of the peripheral nervous system where it has been shown to modulate thermosensing via interactions with the cold-sensing TRPM8 and the heat-sensing TRPV1 ion channels.[14, 15, 61] Additionally, PIRT–TRPV1 interactions have been functionally implicated in histaminergic and nonhistaminergic pruritus (itch), regulation of neuropathic pain, and uterine contraction pain.[16, 17, 65] Beyond TRP channel modulation, PIRT has been implicated in modulating P2X purinoreceptors where it is coexpressed with P2X2 channels in the enteric nervous system and has been reported to inhibit P2X3 currents to reduce bladder overactivity.[18, 19] Despite emerging roles in ion channel modulation, little is currently known about the molecular mechanisms that underlie PIRT function.

Previously work on truncated constructs of PIRT showed it binds to PIP_2; however little is known about how PIRT–PIP_2 binding and PIRT–TRPM8 modulation are integrated.[14] PIP_2 has also been shown to modulate TRPM8 conductance,[32] and only recently have the structural details of TRPM8 been revealed.[64] Despite functional data showing specific amino acids in the TRP domain being involved,[32] the details of TRPM8 binding to PIP_2 still remain elusive due to insufficient electron density for the structure and an absence of robust computational modeling in the key regions identified by Rohacs, et al. in 2005.[32, 64]

PIRT has recently been shown to interact with the TRPM8 S1 through S4 (hTRPM8-S1S4, residues 672-855, including transmembrane helices S1-S4) and the TRPM8 pore domain with a combination of electrophysiology and NMR.[61] The data from that manuscript identified a 1:1 binding stoichiometry for PIRT with TRPM8-S1S4; however, the exact amino acids that bind to TRPM8-S1S4 were not determined. The data herein, identify the specific amino acids that bind to TRPM8-S1S4 and is placed in context with the interactions with the TRPM8 pore domain, which suggests a potential location for PIRT binding to the tetramer.

Presented here, we used a combination of solution NMR, MST, and Rosetta comparative modeling techniques to probe the molecular mechanism of PIRT modulation of TRPM8. Using solution NMR, we assign the full length hPIRT backbone resonances and use solvent paramagnetic relaxation enhancement studies to experimentally identify its general membrane topology. With assigned resonances, we used NMR-detected titrations to highlight specific PIRT residues that bind PIP_2 and the human TRPM8 ligand-sensing domain (hTRPM8-S1S4). These NMR binding studies identify several PIRT residues that bind both the TRPM8-S1S4 and PIP_2; suggestive of competitive binding. Following up with MST, we validate the NMR-detected binding studies with data that show a classical competitive interaction where hPIRT affinity for hTRPM8-S1S4 is reduced (i.e. a higher K_d value) when PIP_2 is present at saturating conditions. To help contextualize the experimental results, comparative models of the human TRPM8 transmembrane domain (TMD, residues 672-1012) were built using state of the art Rosetta homology modeling, constrained by the electron density map from avian TRPM8 structure (PDB: 6BPQ, EMDB: 7127) recently determined with cryo-EM. Additionally, we used Rosetta ligand docking protocols, guided by loose experimental constraints identified by Rohacs, et al., to computationally probe for a potential PIP_2 binding site with the hTRPM8 computational model. These studies provide molecular insight into hPIRT modulation of hTRPM8 and suggest a mechanism where PIP_2 and hPIRT exert modulatory control on hTRPM8 activity.

2.2 Materials and Methods

2.2.1 Purification and Solublization

Expression and purification of hPIRT follows was done in Hilton, et al.[61] The resulting hPIRT was greater than 95% pure as verified by SDS-PAGE (Figure S1A). Following ion exchange chromatography, the buffer was exchanged and concentrated to NMR buffer (4% D_2O (v/v), 20 mM sodium phosphate (Fisher Scientific) and 0.2 mM EDTA at pH 6.5) and a final volume of 180 μL for NMR studies .The identity of the protein was verified by LC-MS/MS (MS Bioworks) using trypsin digestion. The data cover 62% of hPIRT, including regions spanning both N- and C-termini, indicating full-length protein was expressed and purified (Figure S1C).

2.2.2 Expression and Purification of hTRPM8-S1S4

The expression and purification of the human TRPM8 ligand sensing domain (hTRPM8-S1S4) followed what was done previously by and Rath, et al.[61, 66]

2.2.3 Far-UV Circular Dichroism (CD)

Far-UV circular dichrosim spectrophotometry was used to qualitatively confirm the predicted secondary structure of hPIRT with a Jasco J-715 spectropolarimeter and was used to assess the hPIRT secondary structure in the DPC micelles. The CD buffer conditions were identical to those used in the NMR studies with 0.2 mg/mL hPIRT temperature set to 40 °C, which was maintained with a Jasco peltier device (JASCO PTC-424S). The data was collected from signal averaging five scans from 190 nm to 250 nm in 0.5 nm steps.

2.2.4 Detergent Screening hPIRT

In order to optimize the detergent conditions for solution NMR, hPIRT was reconstituted in six different membrane mimics and screened by ^{15}N –TROSY-HSQC experiments (Figure S2). hPIRT was expressed and purified as described above, except that Empigen was exchanged to a specific candidate detergent. The following micelle and bicelle membrane mimics were evaluated: DHPC, LMPC, DMPG:DHPC q = 0.3, LMPG, TDPC, and DPC.

2.2.5 Amino Acid Resonance Assignment and Secondary Structure Assessement

To assign the hPIRT backbone resonances, a 0.9 mM sample of ^{15}N, ^{13}C labeled hPIRT in a 3 mm diameter NMR tube with 4% D_2O (v/v) was used to collect transverse relaxation optimized spectroscopy (TROSY)[67] versions of traditional protein backbone amide 3D experiments on a Bruker 850 MHz (^1H) Avance III HD spectrometer with a 5 mm TCI Cryoprobe. The experiments collected include TROSY-based HSQC, HNCA, HNCOCA, HNCACB, HNCO, and CBCACONH; parameters for each experiment are listed in Tabel S1 and representative assignment data shown in Figure S3. Uniformly sampled NMR experiments were processed in nmrPipe[68] and analyzed in CcpNMR.[42] Non-uniformly sampled experiments were reconstructed using qMDD,[69] processed in NMRPipe, and analyzed in CcpNMR. The resonance assignments were deposited in the Biological Magneic Resonance Bank (BMRB ref 27438). PIRT secondary structure prediction was generated from the backbone resonance assignements with the TALOS-N software.[70]

2.2.6 Non-covalent Solvent Paramagnetic Relaxation Enhancement (PRE) Studies

Resonance intensities were monitored on a 0.3 mM hPIRT sample by collecting ^{1}H-^{15}N TROSY-HSQC spectra at 850 MHz ^{1}H with 0 mM, 2 mM, 6 mM, 10 mM, and 20 mM Gd(III)-DTPA (Sigma Aldrich) from a stock solution of 150 mM Gd(III)-DTPA stock solution (Santa Cruz Biotechnology), 250 mM EDTA used to chelate any free Gd(III) (Sigma Aldrich), and 25 mM sodium phosphate, pH 6.5. The intensities of individual amino acids resonances were then plotted as a function of the concentration of added Gd(III)-DTPA and fit according to a mono-exponential decay $f(x) = e^{-\varepsilon\, x}$; where ε is the solvent paramagnetic relaxation enhancement, x is the concentration of Gd(III)-DTPA added. The magnitude of ε was then plotted as function of the corresponding residue number.

2.2.7 ^{15}N PIRT-detected NMR titrations with TRPM8-SD and PIP$_2$

^{15}N-hPIRT was titrated with ^{14}N-hTRPM8-S1S4 and a short eight carbon chain PIP$_2$ lipid, (1,2-dioctanoyl-*sn*-glycero-3-phospho-(1'-myo-inositol-4',5'-bisphosphate).The titration with hTRPM8-S1S4:hPIRT follows what was done for Hilton, et al[61] with the exception that the mole ratios are converted to mole percentage of titrated hTRPM8-S1S4 are 3.7×10^{-3}, 7.5×10^{-3}, 14.9×10^{-3}, 29.9×10^{-3}, 37.3×10^{-3}, 59.8×10^{-3}, 74.7×10^{-3}, 112.0×10^{-3}, 149.0×10^{-3}, where mole percent is defined as: $mole\ percent =$

$$100\left(\frac{\text{diC8 PI(4,5)P}_2(M)}{DPC\ (M)+hPIRT\ (M)+\text{diC8 PI(4,5)P}_2\ (M)}\right).$$

The titration with PIP$_2$ was done in a similar fashion as hM8-SD. For each titration point, the desired amount of PIP$_2$ was solubilized with 1 mL of ddH$_2$O and aliquoted into separate microcentrifuge such that when resuspended with hPIRT in DPC, the amount of

PIP_2 used corresponded to mole percentages of 0.05, 0.10, 0.15, 0.20, 0.40, 0.80, and 1.5 calculated as above.

Changes in chemical shift were analyzed according to previously established protocols.[48, 61, 71] Errors in K_d were calculated using the standard deviations of the fit by taking the square root along the diagonal of the nonlinear fit covariance matrix using the function above; i.e. for Matlab R2017a [beta,R,J,CovB,MSE]=*nlinfit(xData,yData,fitFunction,beta0)*, standard deviation = sqrt(diag(CovB)).

2.2.8 Microscale Thermophoresis

Microscale thermophoresis was measured on a Nanotemper Monolith NT.115 nano Blue/Green (MO-G008). Human PIRT was labeled with the Nanotemper green maleimide reactive fluorophore. Before labeling, hPIRT was purified and solubilized in 0.1% DPC in 50 mM HEPES buffer at pH 7.5 as described above, which was then buffer exchanged to remove imidazole using a 10 kDa cutoff Amicon Ultra 5. After which, 100 µL of 20 µM hPIRT was reacted with 2 mM DTT for 3 hr at room temperature. Then fluorophore was added to a final volume of 200 µL and a concentration of 2:1 dye:protein (mol:mol). The maleimide reaction was carried out at room temperature overnight and purified using a gravity flow desalting column. One column volume eluted the labeled protein at 6 µM concentration and a volume of 300 µL.

For the hTRPM8-S1S4 sample, 40 µL of 400 nM hPIRT was used per titration point of 0.1368, 0.0342, 0.0171, 0.0086, 0.0043, 0.0011, 0.0005, and 0.0001 of hTRPM8-S1S4. For the PIP_2 sample, 40 µL of 400 nM of hPIRT was prepared with an initial 0.1

mg/mL of PIP_2 with mole percentages of 0.421, 0.220, 0.110, 0.055, 0.028, 0.007, and 0.004. For competitive studies with saturating PIP_2, the hTRPM8-S1S4 was prepared as above but included 4.05 mole% PIP_2 in each tube. All the samples were run in triplicate with 95% LED power and 40% infrared laser power. As a control, hPIRT was titrated in the same buffer conditions and protein concentration as above with DMSO concentrations ranging from 10 μM to 100 mM with no observable binding identified (Figure S4). Error bars in MST measurements were calculated as fraction bound standard errorors of the mean from three separate measurements.

2.2.9 Rosetta Comparative Modeling of the human TRPM8 Transmembrane Domain (residues 672-1012)

Rosetta protocol captures and the protein data bank formatted centroid structure are provided in the supporting information. Briefly, RosettaCM[50] was used to model the human TRPM8 transmembrane domain (amino acids 672-1012). Using RosettaMembrane,[60, 72] 11,300 decoys were generated using *Fa*TRPM8 (6BPQ) and mTRPM4 (6BQV, 6BCL, 6BCJ, 5WP6, 6BCO) cryo-EM structures as templates, and the EM map for *Fa*TRPM8 as a restraint (EMDB: 7127). To use these structural templates, a sequence alignment was created using CLUSTAL-W between the human TRPM8, flycatcher TRPM8, and the mouse TRPM4 (Figure S6), and manually adjusted to enforce a known functional disulfide bond.[73] The alignment file was then used to thread the human TRPM8 sequence onto each template using the Rosetta partial_thread command. The 9mer and 3mer fragments needed were generated using the ROBETTA server with 200 fragments per amino acid for positions 672-1012 of the human TRPM8 amino acid sequence. The flycatcher TRPM8 cryo-EM structure has no density for the following transmembrane regions: 716-721, 820-822, 889-894, 912-945, and 978-990 and were rebuilt de novo with Rosetta. All atom refinement was carried out on the two biggest clusters identified with Calibur software and expanded to 5600 decoys per cluster. All decoys were rescored with mpframework_fa_2007.wts to the respective lowest energy conformer.

2.2.10 Rosetta Ligand Docking of PIP_2 to TRPM8 Transmembrane Domain (residues 672-1012)

A Rosetta protocol capture is provided in the supporting information. Rosetta has been used in the past to dock ligands to membrane proteins[47] and we used a RosettaScripts[74] protocol to computationally dock PIP_2 (CHARMM small molecule library, CSML: SAPI24) to TRPM8. The initial PIP_2 starting point was manually placed out of contact between two sensing domains from symmetric domain swapped monomers with PIP_2 in a head down (intracellular facing) orientation and translated in the relative position of the inner leaflet bilayer. To efficiently sample PIP_2 conformational space, 1000 conformers were generated using Frog2[75] with the AMMOS energy minimization option selected. Docking with RosettaScripts included the Transform mover that performs low resolution Monte Carlo sampling a within a specified 10 Å sphere by flipping, rotating, translating, and sliding PIP_2 into contact with TRPM8.[74] The next two movers, HighResDocker and FinalMinimizer, sampled rotamers (sampling of side chain rotamers, one side chain at a time) and repacking (simultaneous sampling of rotamers for multiple side chains),[74] made small ligand perturbations from 1000 different PIP_2 conformers, and then finally used a gradient ramp to minimize the docked complex while keeping the backbone of the protein restrained with relatively limited side chain movement.[74] A total of 10,000 decoys were generated using these movers, from which the score vs the ligand RMSD is analyzed to identify clusters of binding modes with cluster centroids manually analyzed in PyMol. From these centroids, a refinement of the most common decoys were seeded to generate an additional 1000 decoys that were guided by experimental constraints where either Lys995 or Arg998 could interact with the head group of PIP_2.[32] In order to limit computational bias, the constraint file did not direct which phosphate should interact with Lys995 or Arg998, nor did it specify whether Lys995 or Arg998 would be favored for the interaction. Separately, docking with PIP_2 constraints guided to Arg1008 was calculated (data not shown) and analyzed with poor results and modes that force PIP_2 into a non-physiological state and it is worth noting that Arg1008 is not near enough to the positively charged pocket where Lys995 and Arg998 to satisfy one PIP_2 molecule per monomer. Additionally, the PIP_2 tails were loosely constrained by enforcing the distal regions of the acyl chains to midpoint of the membrane bilayer in order enforce a physiologically relevant PIP_2 membrane depth. After the constraint guided docking, a small perturbation using the Transform mover was applied to reduce over biasing the mode of docking followed by the HighResDocker and FinalMinimizer. Refined cluster centroids were analyzed as before and 20 PIP_2 conformations from each of the three clusters were used in analysis of TRPM8–PIP_2 complex and the implications for PIRT modulation.

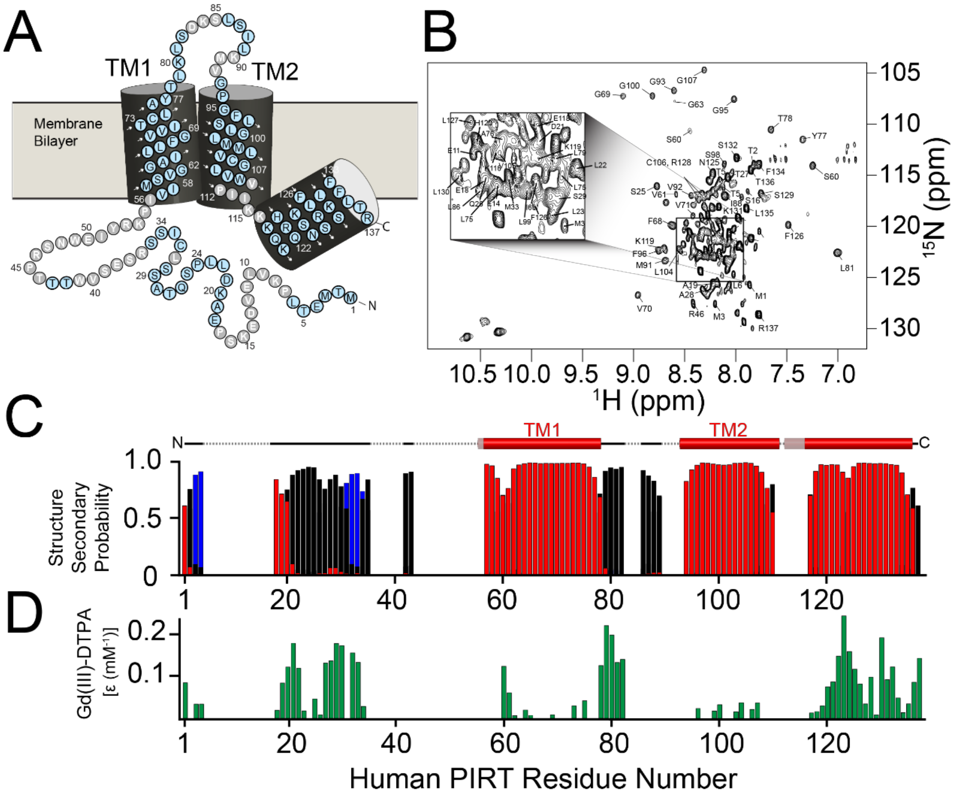

Figure 2.1 NMR derived secondary structure and topology of hPIRT. (A) The general topology consists of a relatively unstructured N-terminus, two transmembrane α-helices, and a C-terminal amphipathic α-helix. The light blue circles indicate assigned residues and the gray circles represent unassigned residues. (B) The TROSY-HSQC of hPIRT reconstituted in DPC shows a well-resolved spectrum with dispersion consistent with a helical membrane protein. (C) The plot of the consensus secondary structure derived from Cα, Cβ, and Co chemical shifts input into TALOS-N. Red, black, and blue bars indicate the probability of α-helix, loop, and β-sheet respectively. (D) Solvent paramagnetic relaxation enhancement from Gd(III)-DTPA (ε mM^{-1}, see Methods section) was used to measure solvent accessibility and confirm the hydrophobic nature of the two transmembrane α-helices and the amphipathic nature of the C-terminal α-helix.

2.3 Results

2.3.1 Optimization of Expression and Purification of Human PIRT

The human PIRT membrane protein was optimized for expression and purification from *E. coli* to an average yield of 3 mg of purified protein per liter of M9 minimal media, following a previously established protocol.[61] The purity of hPIRT was detected by SDS-PAGE (Figure S2.1A), far-UV CD measurements indicate that PIRT is a predominantly α-helical protein with characteristic spectral minima near 210 nm and 222 nm, and a maximum at 194 nm (Figure S2.1C), and finally the protein identity was confirmed with LC-MS/MS (Figure S2.1D).

2.3.2 Optimization of NMR Conditions for Biophysical PIRT Studies

Selection of the PIRT membrane mimic for NMR-based studies was done empirically by screening different detergents and bicelle conditions while monitoring ^{1}H, ^{15}N TROSY-HSQC NMR spectra (Figure S2.2). The optimal NMR spectrum typically has the narrowest linewidths, broadest proton resonance dispersion, and has the expected

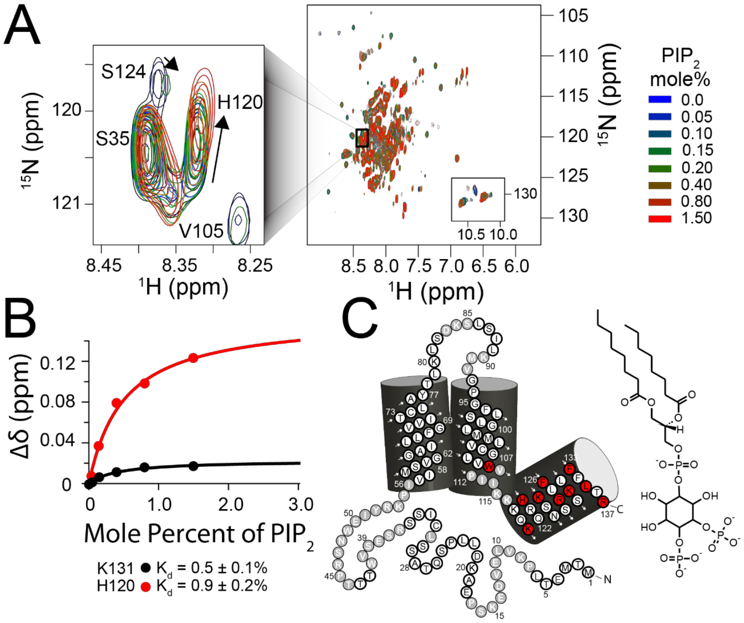

Figure 2.2 NMR titration of hPIRT with the signaling lipid PIP$_2$. (A) Overlay of eight 15N-TROSY HSQC hPIRT NMR spectra that are colored as a function of increasing PIP$_2$ concentration. The left inset shows changes in H120 resonance position as the lipid is titrated. (B) Representative chemical shift perturbation (Δδ) titration plots for hPIRT K131 and H120 which are fit to a single binding site model as described in the methods. (C) hPIRT residues that specifically bind PIP$_2$ are highlighted in red on the topology plot.

number of resonances. In the case of hPIRT there are three expected tryptophan indole amine resonances downfield (ca. 10 ppm) in the ^{1}H dimension and seven glycine backbone amide resonances which are characteristically upfield in the ^{15}N dimension (ca. 105 ppm). Ideally, one should expect a given number of total resonances that correspond to all of the backbone amides in the sequence, except for prolines. Human PIRT was reconstituted in a DPC membrane mimic for NMR studies after several other detergent micelles and bicelle mimics were evaluated. PIRT is stable in DPC for weeks and gives well resolved spectra, for a helical human membrane protein.

In an effort to test the suitabiliy of DPC as a membrane mimic, NMR-detected titrations of hPIRT in DPC micelles with PIP_2 and the human TRPM8 ligand sensing domain (residues 672-855, including helices S1-S4) were shown to saturate hPIRT (Figures 2.2 and 2.3), a hallmark of specific and direct binding. These results indicate that hPIRT is in a biologically relevent structural confirmation; the significance of the affinities are discussed below.

Previous bioinformatic analysis of PIRT predicts a helical two-span membrane protein and the far-UV CD spectrum of DPC reconstituted PIRT in Figure S2.1C provides qualitative agreement. The CD data suggest an α-helical membrane protein with spectral minima at 210 nm and 222 nm and a postive maximum near 195 nm.

2.3.2 Human PIRT Backbone NMR Resonance Assignment and Secondary Structure Prediction

TROSY 3D NMR experiments were used to assign 64% (Figure 1A) out of the 146 hPIRT backbone resonances ((9 residues from the His tag and 137 from the hPIRT construct) ^{15}N, ^{1}H, $^{13}C_{\beta}$, $^{13}C_{\alpha}$, and ^{13}C′) on a U-^{13}C/^{15}N hPIRT sample in DPC micelles at

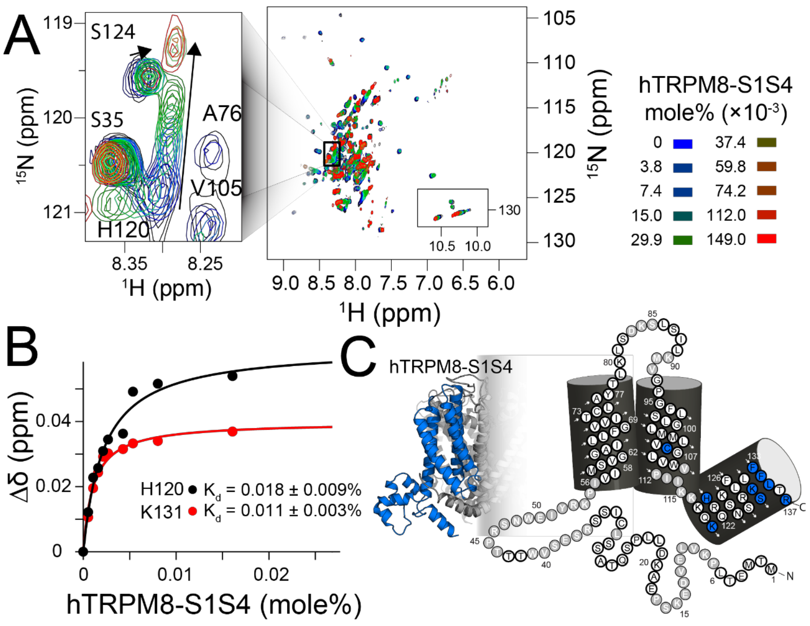

Figure 2.3 NMR titration of hPIRT with the hTRPM8-S1S4 domain. Uniformly 15N labeled hPIRT was titrated with unlabeled (^{14}N, NMR silent) hTRPM8-S1S4 and monitored using 15N-TROSY HSQC experiments. (A) Overlay of ten PIRT NMR spectra as a function of increasing hTRPM8-S1S4 concentration. At about 0.025 mol% hTRPM8-S1S4 the PIRT H120 change in resonance position (inset) saturates while non-binding residues are unperturbed. (B) The chemical shift perturbation was quantified and fit to a standard 1:1 binding model to calculate the affinity (Kd). Representative binding data for H120 and K131 are shown. (C) Individual PIRT residues that specifically bind to the hTRPM8-S1S4 are mapped onto the PIRT topology diagram. The hTRPM8-S1S4 is highlighted in blue next to the hPIRT topology to emphasize the domain being titrated.

40 °C and pH 6.5. Representative assignment data are shown in Figure S3. The resonance assignments (Figure 2.1B) were used as input for TALOS-N, from which secondary structure elements of hPIRT were experimentally predicted (Figure 2.1C). These secondary structure predictions were combined with Gd(III)-DTPA, a hydrophilic paramagnetic probe to experimentally map the hPIRT membrane topology (Figure 2.1D). The data suggest that the start of TM1 is likely near Pro55 as the Gd(III) shows increasing solvent accessibility with the available assigned Val56. TM1 ends at Ala76 from which TM2 starts at Gly93; however, the end of TM2 is not clearly defined.

Nonetheless PsiPred-based bioinformatics predictions suggest that TM2 terminates between Pro112 and Lys115.[76] After TM2, the remaining C-terminal residues comprise an amphipathic α-helix (Asp125 to Arg137), of which the amphipathicity was clearly identified by NMR with the paramagnetic probe studies (Figure 2.1D). The amphipathic C-terminal helix provides a region that can hug the membrane bilayer and allow for interactions at the bilayer interface with lipids or proteins.

Most of the resonance assignments come from the transmembrane α-helices and the putative PIP_2 binding pocket, which are membrane mimic associated and typically less dynamic than soluble loops. Using disorder prediction from PsiPred suggests that the PIRT N-terminus is disordered which hinders resonance assignment from spectral overlap.[76, 77] Indeed this region includes several proline residues (Pro7, Pro16, Pro23, Pro45, and Pro55) that complicate resonance assignment; similarly, there are several repeated amino acids (Leu22-Leu23, Ser29-Ser30, Ser34-Ser35, and Thr42-Thr43-Thr44) making assignment of the N-terminal loop challenging. Nevertheless, the putative PIP_2 binding pocket and the majority of the transmembrane helices have been successfully assigned.

2.3.4 NMR-detected Human PIRT Titrations with PIP_2 and the hTRPM8-S1S4 domain

NMR assignment allows for identificaiton of residue specific information from NMR-based binding studies, and can provide details about affinity and which regions are involved in binding, where saturation of chemical shift perturbation ($\Delta\delta$) is indicative of specific and direct binding.[34] hPIRT-detected titrations of PIP_2 (Figure 2.2) and hTRPM8-S1S4 (Figure 2.3) idenfity several PIRT residues with saturable binding curves.

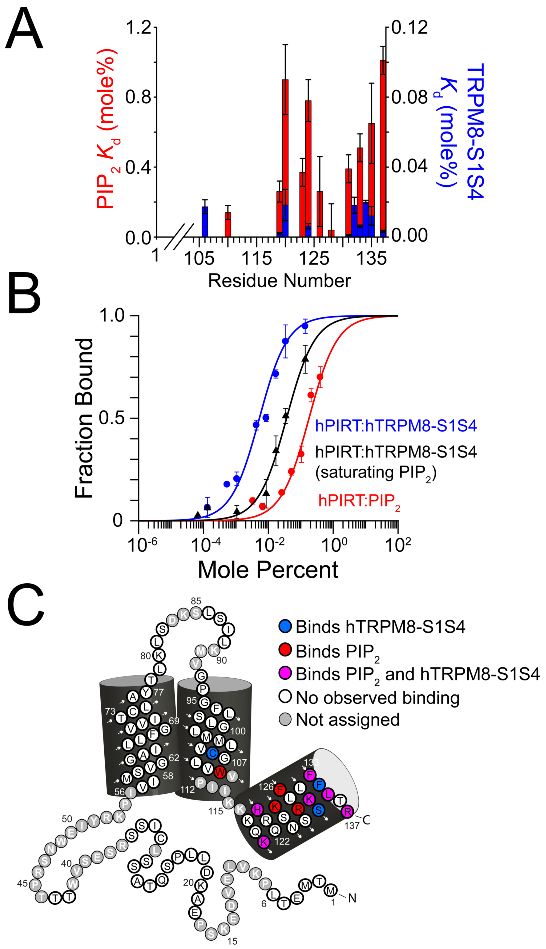

Figure 2.4 Competitive binding between PIP_2 and the TRPM8-S1S4 domain to PIRT. (A) NMR-detected titrations show PIRT residues that bind both to PIP_2 and TRPM8 (magenta) are generally localized to the intracellular amphipathic helix. Residues that exclusively bind PIP_2 (hTRPM8-S1S4) are colored red (blue). The overlapping binding regions indicate a competitive interaction for PIRT. (B) NMR derived PIRT affinities for the two ligands. (C) MST measurements also show a competitive binding relationship between hPIRT, hTRPM8-S1S4, and PIP_2. When hPIRT is titrated with the TRPM8-S1S4 domain in the presence of saturating PIP_2, the affinity shifts rightward, indicative of competition. (D) The histogram shows the affinities determined from the MST competition assay. MST Kd values are 5.3 ± 0.4, 36.5 ± 0.5, and 180 ± 60 millimole percent for hPIRT:hTRPM8-S1S4, hPIRT:hTRPM8-S1S4 + PIP_2, and hPIRT:PIP_2 respectively

Dissociation constants in units of mole percent have been utilized previously in membrane protein studies to show affinities for ligands that strongly partition into the

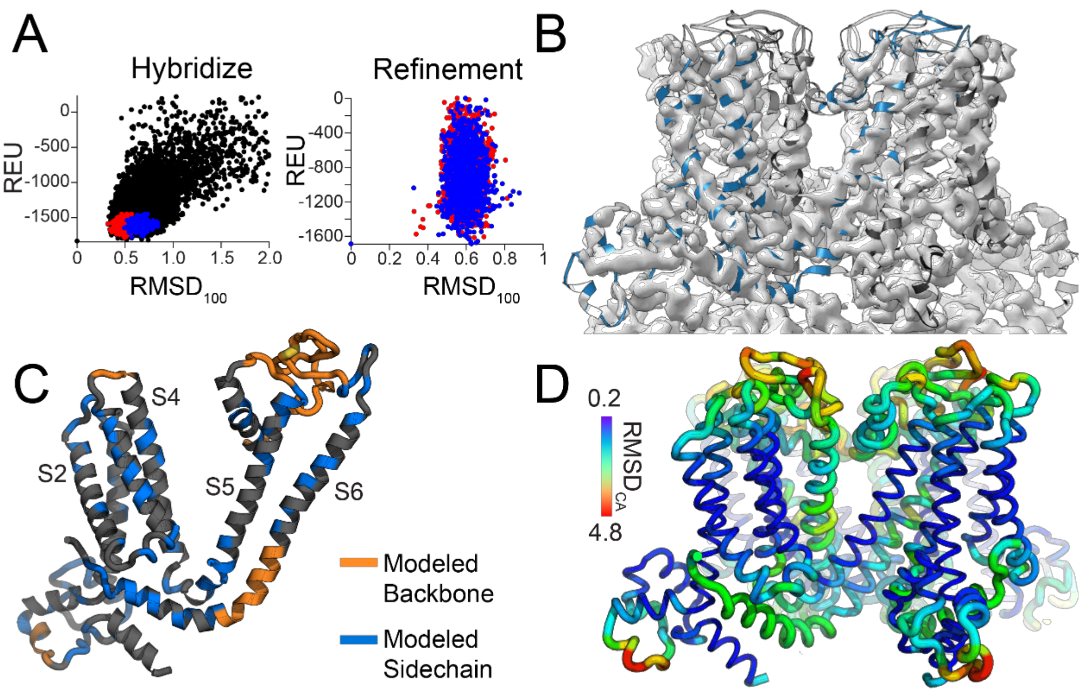

Figure 2.5 Comparative modeling of the human TRPM8 transmembrane domain. The collared flycatcher avian TRPM8 ortholog cryo-EM structure was used as a template with Rosetta Hybridize protocols and refined with the electron density map from FaTRPM8 to generate human TRPM8 TMD comparative models. (A) RosettaCM protocols were used to model human TRPM8 and shows a characteristic energy funnel with the largest clusters highlighted in red and blue. A final refinement was carried out using the EM density map as restraints in Rosetta. (B) The hTRPM8 model tetramer fits well in the cryoelectronic density map with an EM Ringer score of 1.6 indicating the model agrees with the experimental map. (C) A representative monomer from the human TRPM8 transmembrane domain model with organ coloring indicated regions that were built de novo with RosettaCM because of missing density in the FaTRPM8 map. Blue regions indicate locations where sidechains were built that were lacking in the FaTRPM8 structure. (D) Putty representation of the Cα RMSD magnitudes for the top ten human TRPM8 models where the loop thickness and color correlate with RMSD.

membrane or membrane mimics.[66, 71] Previous studies have estimated that the physiological concentration of PIP_2 in the inner leaflet of dorsal root ganglia (DRG) is ca. 1% of membrane mass.[20]

We have shown previously that the titration of hPIRT with the hTRPM8-S1S4 shows that hPIRT also interacts directly and specifically with the hTRPM8-S1S4 (Figure 2.3). Residues that bind specifically to the sensing domain include K119, H120, and R121 that overlap with the putative PIP_2 binding pocket (Figure 2.3C) along with several other residues. The binding units of mole percent here are most useful in comparing relative affinities of hPIRT to PIP_2 and the hTRPM8-S1S4 as these species are isolated to the membrane mimic regions and thus depend on the mimic concentrations and not directly on the aqeous volumes. Previously, it was shown using mole ratio titrations that hPIRT saturates at 0.5:1 hPIRT:hTRPM8-S1S4 suggestive of a 1:1 stoichiometry.[61]

2.3.5 MST Binding Measurements and Competition Assay

NMR studies of TRPM8-S1S4 and PIP_2 binding to PIRT identify the potential for a competative interaction based on overlapping putative binding pockets (Figure 2.4A, 2.4B, and Table S2.1). In order to test a competative model for hPIRT to PIP_2 and the hTRPM8-S1S4, we utilized MST bindind studies. MST has been used previously to measure affinities for TRPM8-S1S4 ligand interactions,[66] PIP_2 protein interactions,[78] and has been shown to be highly sensitive to minor differences in binding.[44] K_d values obtained from MST (Figure 2.4C), corroborate the NMR determined affinities of hPIRT for PIP_2 and hTRPM8-S1S4 with K_d values of 0.18 ± 0.06 mole% and 0.0053 ± 0.0004 mole%, respectively. Competitive hPIRT binding to hTRPM8-S1S4 in the presence of a saturating PIP_2 concentration shows a 7× decrease in affinity to 0.0365 ± 0.0005 mole%. A negative control for the MST studies shows that hPIRT does not to bind DMSO (Figure S2.4).

2.3.6 Rosetta Comparative Modeling of Human TRPM8 Transmembrane Domain

In order to contextualize the hPIRT competition with PIP_2 and TRPM8, RosettaCM was used to generate comparative human TRPM8 comparative models of the transmembrane region (Figure 2.5, residues 672 to 1012). The initial models using the hybridize mover with all atom refinement shows a characteristic funnel of decreasing

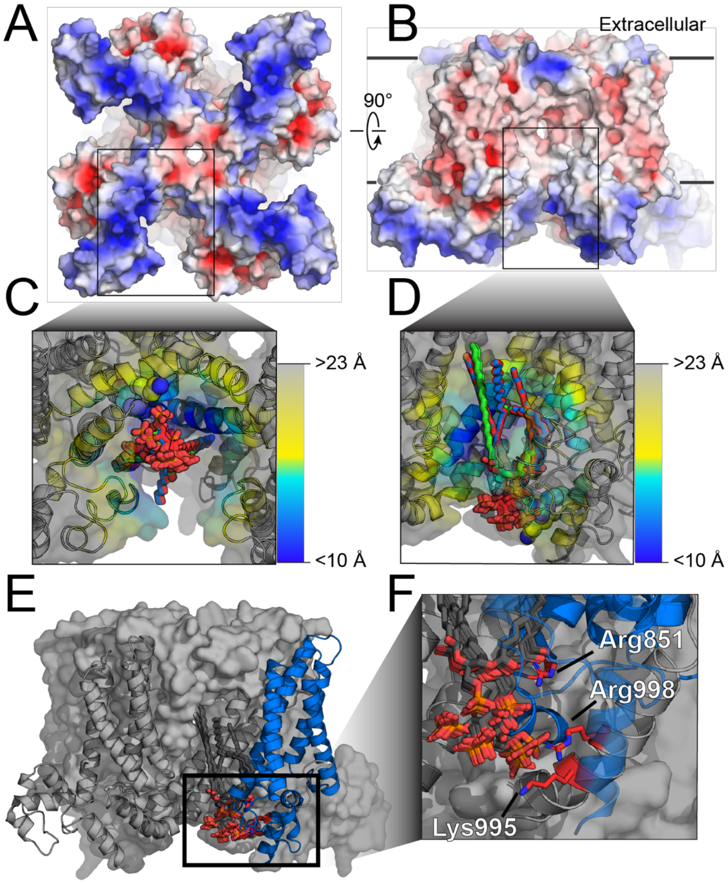

Figure 2.6 Rosetta predicted PIP_2 binding site in TRPM8. (A) The electrostatic surface of the TRPM8-TMD shows a positively intracellular region comprising lysine and arginine residues focused near the TRP domain and Pre-S1 helices. (B) A 90° rotation of (A) shows the electrostatic surface from the membrane plane. (C, D) Rosetta-based algorithms and experimental restraints were used to computationally dock PIP_2. The best scoring PIP_2¬TRPM8 complexes overlaid from the top three cluster centers, showing 60 total PIP_2 conformers. The TRPM8–PIP_2 complex (E) suggests that PIP_2 adopts a conformation that is physiologically relevant and provides insight into how PIP_2 interacts with the channel and competitively with hPIRT. Highlighted in (F) are the charged residues within 4 Å that have potential to form hydrogen bonds with PIP_2.

energy scores as a function of the RMSD, typically consistent with sampling convergence (Figure 2.5A). The relatively tight convergence benefitting from the available electron density map (Figure 2.5B) from the collared fly catcher (*Ficedula albicollis)* TRPM8 (*Fa*TRPM8) from cryo-EM structure.[64] With RosettaCM and the EM map constraints, we have built in loops and side chains that are absent in the *Fa*TRPM8 structure (Figure 2.5C).[64] Using the EM map with RosettaCM restrained the models such that the relative RMSD_{100} is resolved (Figure 2.5D). The centroid, or average, model from the top ten final decoys was put through EMRinger (score = 1.6) and Moleprobitiy (clash score = 4.99, 94th percentile with the number of residues = 1784) to analyze the quality of the model.[79, 80] These scores suggest that the representative model is generally consistent high quality protein structures and specifically agrees with the *Fa*TRPM8 EM data.

The centroid from the hTRPM8-TMD modeling (SI Materials: hTRPM8-TMD.pdb) was used to calculate an electrostatic map with the Adaptive Poisson-Boltzmann Solver plugin within PyMol (Figure 2.6).[81] The electrostatic map shows a basic (positive, blue) area on the intracellular side of the ligand sensing domain (S1-S4) (Figure 2.6A) consistent with the positive inside rule of membrane topology. Our computationally modeled hTRPM8-TMD shows positive residues comprising Arg680, Arg688, Arg851, Lys995, Arg998, and Arg1008 (Figure 2.6), that were previously suggested to potentially interact with the electronegative phosphoryl groups in PIP_2.[32, 64]

2.3.7 Rosetta Ligand Docking Applied to TRPM8–TMD with PIP_2

The ligand docking specific RosettaScripts movers were utilized on the TRPM8 transmembrane domain with PIP_2 and a putative binding mode identified. We generated

10,000 decoys with RosettaScripts to initially probe a binding pocket within the TRPM8-TMD where PIP_2 was found to favor a site that is compatible with previously observed functional data. It is worth noting that in our unrestrained docking the TRPM8-S1S4 was never identified to interact with the PIP_2 phosphoinositol lipid head group moiety, instead PIP_2 interactions were focused to the juxtamembrane region close to the TRP domain. From this initial docking calculation, we selected centroids from the largest clusters (Figure S2.5) to seed the next round of docking where we used experimental constraints to gently guide the docking (Figure S2.5C). The constraint file did not direct which phosphate should interact with Lys995 or Arg998, nor did it specify whether Lys995 or Arg998 would be favored for the interaction as the exact mode of PIP_2 binding is unknown. With 1000 experimentally guided decoys, generated from the 10,000 initial decoys, three PIP_2 clusters were identified near TRPM8 residues Lys995 and Arg998. Interestingly, PIP_2 decoys in the vicinity of TRPM8 Arg1008 were not populated in the large in initial docking of 10,000 PIP_2 decoys. Nonetheless in subsequent studies, PIP_2 was guided near Arg1008 using constraints (data not shown); however, the output from these 1000 decoys did not provide clear convergence. Generally, the Arg1008 guided decoys resulted in the PIP_2 acyl chains navigating to the interior of the S1-S4 domain, which is a relatively polar area. This may suggest that while Arg1008 mutations decrease PIP_2 mediated TRPM8 activity, it may not interact directly with PIP_2. On the other hand, it may suggest that TRPM8 undergoes conformational change that generates a second PIP_2 binding site near Arg1008 that is not accessible in our hTRPM8-TMD model. We note that conformational state dependent PIP_2 binding sites have been suggested for the KCNQ2 voltage-gated ion channel.[25]

2.4 Discussion

Since its identification in 2008, PIRT has been implicated in modulation of TRPM8, TRPV1, P2X3, and P2X2 ion channels with corresponding functional consequences that impact hot and cold temperature sensing, neuropathic and uterine contraction pain sensing, histaminergic and nonhistaminergic itch, enteric nervous system regulation, and overactive bladder disfunction.[11, 14, 16-19, 28, 61, 62, 65] Initial PIRT functional studies, implicated the TRPM8–PIRT complex in thermosensing such that PIRT increased TRPM8 channel conductance in mouse models.[11, 62] Recently, studies identified species dependent effects that recapitulated the mouse PIRT activation of mouse TRPM8 but showed that human PIRT significantly attenuates human TRPM8 conductance.[61] Human PIRT was identified to directly bind to the hTRPM8-S1S4 and the hTRPM8 pore domain.[61] To expand our understanding of human TRPM8 modulation by human PIRT at the molecular level, we used solution NMR to assign the backbone resonances of hPIRT, experimentally determine the hPIRT membrane topology, and characterized the direct binding of hPIRT to both PIP_2 and the hTRPM8-S1S4 domain. These NMR-detected binding data are suggestive of a competitive interaction between PIRT binding PIP_2 and the hTRPM8-S1S4. MST studies confirm a classically competitive binding model between PIP_2 and hTRPM8-S1S4 for PIRT. Using the Rosetta software suite, we constructed a comparative model of human TRPM8 transmembrane domain relying on the electron density map from the avian *Fa*TRPM8 structure and the homologous mouse TRPM4 structure. Additionally, we computationally docked PIP_2 to this model guided by existing experimental data on functional TRPM8 interactions with PIP_2. Taken together, the data presented herein are consistent with a molecular mechanism whereby hPIRT exerts modulatory control of hTRPM8 through a competitive PIP_2 shuttling/sequestering mechanism.

hPIRT screening identifies dodecylphosphocholine (DPC) as a suitable membrane mimic, compatible with high-resolution solution NMR and binding studies to PIP_2 and TRPM8. Under these optimized conditions, far-UV CD qualitatively shows that hPIRT is a predominantly helical protein (Figure S1C) as predicted from bioinformatics analysis. Assignment of backbone NMR resonances, in conjunction with an aqueous paramagnetic probe, we experimentally identify that the PIRT secondary structure and membrane topology includes a relatively unstructured and flexible N-terminal loop, two transmembrane α-helices, and a C-terminal polybasic amphipathic α-helix. The experimentally determined membrane topology agrees with previous studies that suggest that the polybasic PIRT C-terminus is located in the inner membrane bilayer leaflet where PIP_2 is predominantly located and in agreement with other known PIP_2 binding proteins.[21, 22]

NMR-detected binding studies provide insight into residue specific interactions and possible modes of binding,[34] which we used to identify a number of residues focused around the polybasic amphipathic C-terminal helix that specifically bind PIP_2 and hTRPM8-S1S4. We measured the K_d for the PIRT–PIP_2 interaction to be tighter than the DRG PIP_2 concentration of ca. 1% by weight, which is indicative that the interaction is in a physiologically relevant range (Figure 2).[20] Consistent with a previous study,[61] our binding data extend observations that hPIRT binds directly to the hTRPM8-S1S4 domain (Figure 3) by identifying specific hPIRT residues involved in this interaction. The affinity of hPIRT for the hTRPM8-S1S4 domain is higher (lower K_d,) corresponding to tighter binding with a surprising outcome that the putative hPIRT–PIP_2 binding region, while not identical to, has significant overlap with the hPIRT residues that specifically bind the hTRPM8-S1S4 domain (Figure 4A); consistent with a competitive interaction.

MST direct binding studies confirm the NMR binding data that hPIRT interacts with both PIP_2 and the hTRPM8-S1S4 domain (Figure 4C), with significantly higher relative affinity (lower K_d value) for the TRPM8-S1S4 domain that is about 35-fold higher than that for the PIP_2 lipid. While generally in good agreement, the relatively small differences in the affinities observed here are likely explained by the fact that the NMR experiments were carried out at 40 °C and the MST measurements at 25 °C (see Results). Additionally, the TRPM8-S1S4 competitive binding assay in the presence of saturating PIP_2 from MST supports the overlapping residues identified by binding data from NMR. Specifically, in the presence of saturating PIP_2, the affinity between PIRT and TRPM8-SD is decreased by ca. 7-fold. Taking the binding data together, we show a strongly suggestive competitive interaction. In the context of functional regulation, we suggest that the mechanism for hPIRT regulation of hTRPM8, relies at least in part, by modulating channel access to PIP_2.

Despite the recent TRPM8 structure determination, the molecular details of PIP_2 binding are unknown and, as of the writing of this manuscript, have yet to be structurally modeled. Access to PIP_2 has strong modulatory effects on many ion channels, including many TRP channels,[9, 24-26, 30, 31, 82, 83] with recent studies suggesting channel regulation is controlled by access to PIP_2.[31, 83] Structurally homologous to TRPM8, the voltage gated potassium channel KCNQ1 requires PIP_2, which is thought to stabilize the channel open state by maintaining coupling between the voltage-sensing domain (helices S1-S4) and the pore domain (S5-S6).[9, 84] In KCNQ1, functional studies have suggested that positively charged residues are important to PIP_2 regulation, including the post S6 helical region;[85] a region that is structurally homologous to the PIP_2 sensitive TRP domain in TRPM8.[85] The PIP_2 sensitive residues in the TRP domain include Lys995, Lys998, and Arg1008 and are located within the inner leaflet bilayer interface that passes under the TRPM8-S1S4 domain in the tetramer. Low electron density (Figure 5, B and C) in these key areas including backbone and sidechains, of the *Fa*TRPM8 structure were rebuilt using Rosetta comparative modeling and a human sequence for the TRPM8 transmembrane domain. Furthermore, using sparse electrophysiological data identified by Rohacs, et al. as constraints to guide Rosetta docking (Figure 6), we generated a model for PIP_2 binding to the TRP domain with the aliphatic lipid tails potentially interacting with the S1-S4 domain and pore domain (Figure 6, C and D). This PIP_2 binding model is consistent with KCNQ1, and other PIP_2 regulated ion channels, that have charged residues located at the interface of the inner leaflet bilayer (Figure 6, E and F). PIRT-dependent modulation of TRPM8 through PIP_2 access control is potentially homologous to KCNQ1-KCNE1, which is functionally dependent on and regulated by PIP_2.[84, 85] Given our experimental data that PIRT binds both PIP_2 and the hTRPM8-S1S4 competitively (Figure 4) and that functionally, PIRT modulation of TRPM8 depends on the pore domain,[61] these PIP_2–TRPM8 docking studies are consistent with a competitive model of PIRT regulation of human TRPM8.

The PIP_2 shuttling controlled by PIRT in a TRP channel specific fashion is a plausible mechanism based on the multitude of roles that PIP_2 plays in biology[86] and the many regulatory pathways controlling its availability. Some of these pathways include regulation of PIP_2 biosynthesis, interconversion between phosphoinositide species, and degradation (e.g. phospholipase C cleavage of PIP_2 to IP_3 (inositol (1,4,5) tris-phosphate) and diacylglycerol). Additionally, PIP_2 local concentrations can be controlled by sequestration by PIP_2 binding proteins.[27, 87] For example, MARCKS (Myristoylated alanine-rich C-kinase substrate) is a PIP_2 binding protein that is thought to participate in regulating the concentration of free PIP_2 in the membrane.[87, 88] The MARCKS–PIP_2 interaction is reversible such that free PIP_2 concentrations can be dynamically modulated.[87] PIRT like MARCKS and other PIP_2 binding proteins, has a polybasic region that is electrostatically complementary to the PIP_2 headgroup (Figure 1A). As such is seems that PIRT regulation of TRPM8 activity, and ion channels in general, may arise at least in part from the ability of PIRT to shuttle and/or sequester PIP_2.

Our results suggest a mechanism for how human PIRT modulates human TRPM8 activity. Specifically, because TRPM8 activity depends on TRP domain access to PIP_2,[64] regulating PIP_2 availability by hPIRT sequestration explains the outcomes of previous hPIRT-dependent hTRPM8 decreases in conductance.[61] Additionally, our NMR, MST, and computational data suggest that hPIRT is likely positioned in the space flanked by domain swapped ligand sensing domains where it can interact with the pore domain,[61] ligand sensing domain, and PIP_2; homologous to the KCNE3-KCNQ1 complex.[48] In general, PIRT–PIP_2 interactions could lead to increased or decreased local effective PIP_2 concentrations, i.e. a shuttling/sequestering mechanism, that would lead to both positive and negative regulation of PIP_2-dependent protein function, depending on species. In the context of human TRPM8 regulation by human PIRT, we suggest that PIRT modulates TRPM8 activity in part by regulating access to PIP_2, thereby affecting TRPM8 sensitivity to a surfeit of stimuli, which has implications for understanding molecular mechanisms of cold sensation and pain regulation.

2.5 Supplementary Information

Experiment*	**Scans**	**F1 (direct)**		**F2 (indirect)**		**F3 (indirect)**		**NUS %**
		Points	**SW (Hz)**	**Points**	**SW (Hz)**	**Points**	**SW (Hz)**	
^{15}N, ^{1}H HSQC	128	2048	11029.4	128	2843.5	N/A	N/A	0
HNCA	64	2048	10638.3	64	5559.1	128	2585	50
HN(CO)CA	64	2048	10638.3	64	5559.1	128	2585	50
HNCACB	64	2048	10638.3	64	16039.1	128	2585	50
CBCA(CO)NH	64	2048	10638.3	64	16039.1	128	2585	50
HNCO	24	2048	10638.3	64	5559.1	128	2585	50

******All experiments were TROSY-based*

Table S2.1 Human PIRT NMR experimental parameters. NUS is for non-uniform sampling.

NMR Binding Data				
Residue	**PIP_2 (mol%)**		**TRPM8-S1S4 (mol%)**	
	K_d	**Error**	**K_d**	**Error**
106	-	-	0.0173	0.004
110	0.14	0.04	-	-
119	0.26	0.06	0.0021	0.0004
120	0.90	0.20	0.0183	0.009
123	0.37	0.08	-	-
124	0.78	0.12	0.0062	0.0015
126	0.26	0.20	-	-
128	0.04	0.15	-	-
131	0.39	0.08	0.0011	0.0003
132	-	-	0.0182	0.0046
133	0.51	0.08	0.0061	0.0007
134	-	-	0.0203	0.0011
135	0.65	0.23	0.0121	0.0053
136	-	-	-	-
137	1.01	0.08	0.0032	0.0007

Table S2.2 Human PIRT NMR detected K_d. The binding constants are reported in mole% derived from fitting chemical shift perturbations as a function of mole% concentrations of PIP_2 and TRPM8-S1S4 to a standard 1:1 binding isotherm. The hyphen means no observed binding.

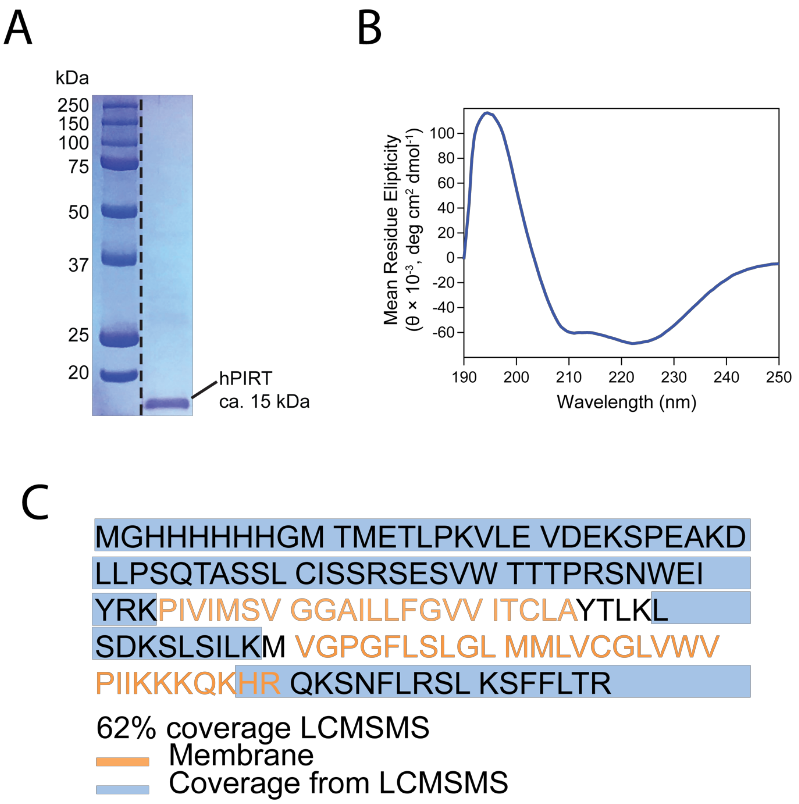

Figure S2.1 SDS-PAGE and far-UV circular dichroism of hPIRT. In (A), a 12% SDS-PAGE gel shows that hPIRT is pure after Ni-NTA and subsequent ion exchange chromatography purification. In (B), circular dichroism of hPIRT at 40 °C (where all NMR experiments were carried out) show a spectrum with two mean residue elipticity minima at 210 nm and 222 nm as well as a mean residue elipticity maximum at 194 nm characteristic of an α-helical protein. (C) Liquid chromatography-tandem mass spectrometry coverage highlighted in blue and the transmembrane regions highlighted in orange showing that the majority of the protein that can be identified except for regions that are typical for membrane proteins, i.e. membrane buried residues.

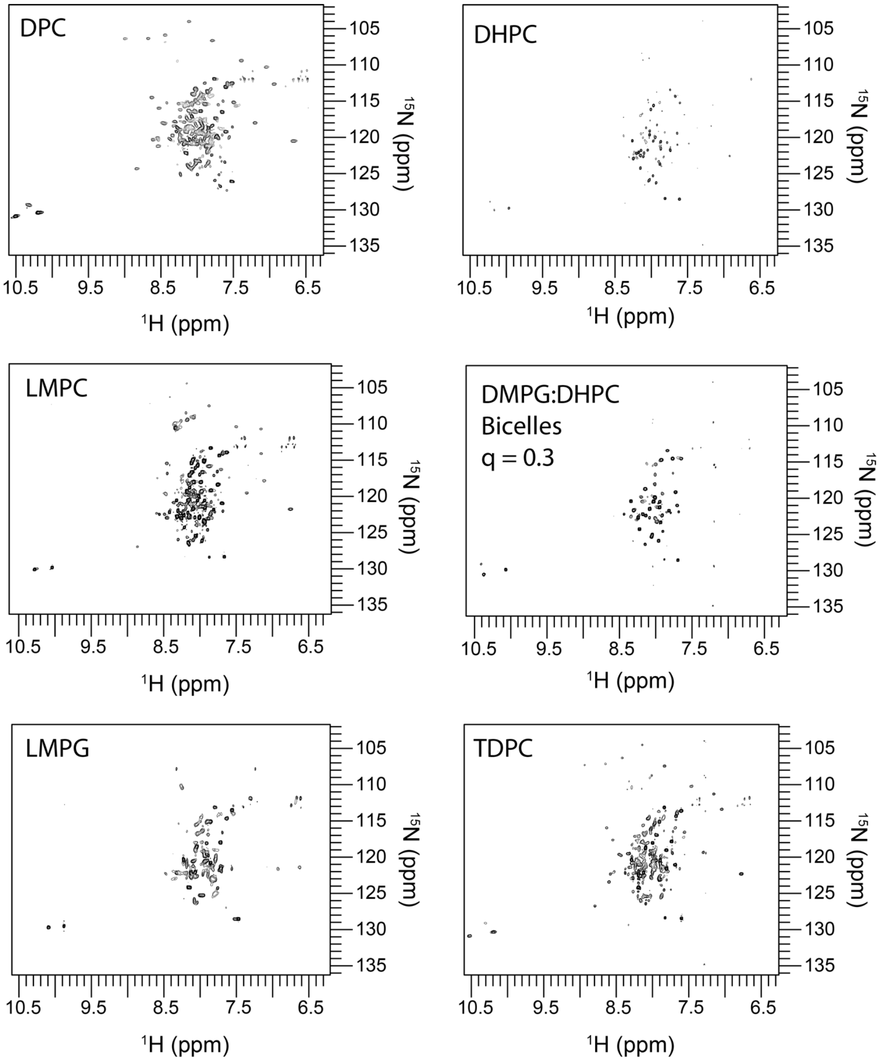

Figure S2.2 Membrane reconstitution detergent screens monitored with two-dimensional NMR experiments. TROSY 1H, ^{15}N HSQC spectra of hPIRT at 40 °C are displayed, from which DPC was chosen as the membrane mimic to use in pursueing structural characterization with NMR. The hPIRT spectrum reconstituted in DPC shows the narrowist line widths as well as the appropriate number of resonances correlated to the amide backbone of hPIRT as well as showing the charactersitic downfield indole amine resonances that correlate to the side chain of tryptophan, which hPIRT sequence is comprised of three.

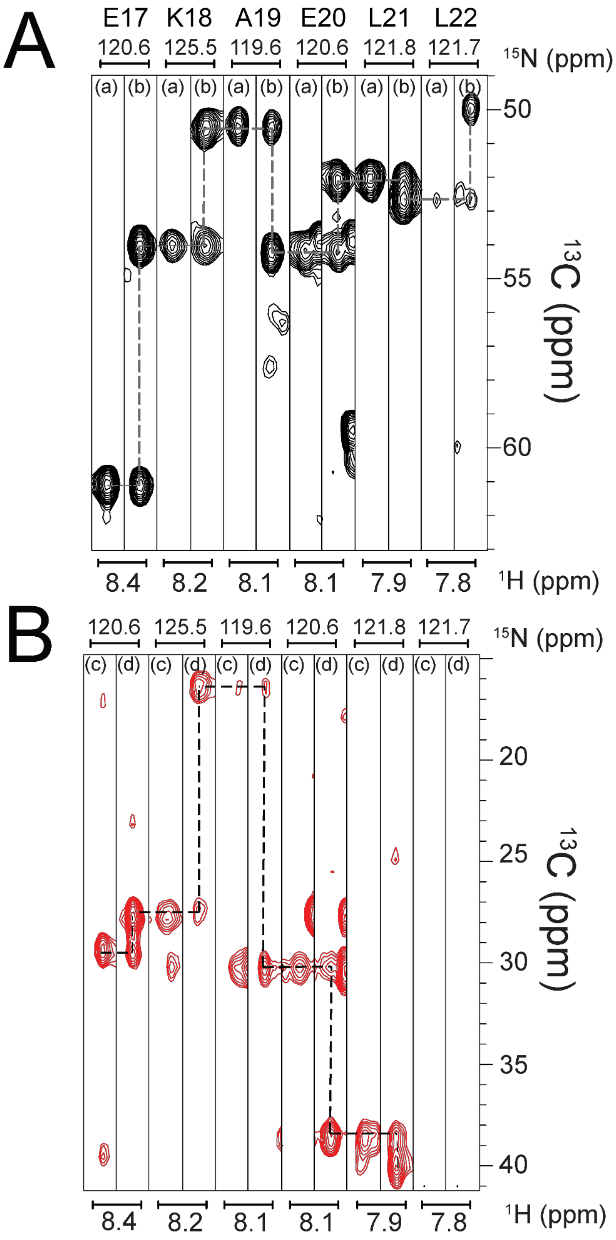

Figure S2.3 (A) Representative triple resonance strip plot showing the connectivity of amino acid resonances. The experiments shown are (a) HN(CO)CA correlating $^{13}C^{\alpha}_{i\text{-}1}$, (b) HNCA correlating $^{13}C^{\alpha}_{i,i\text{-}1}$, (c) CBCA(CO)NH correlating $^{13}C^{\alpha}$ -$^{13}C^{\beta}_{i\text{-}1}$, and (d) HNCACB correlating $^{13}C^{\alpha}$ - $^{13}C^{\beta}_{i,i\text{-}1}$. The A panel are connections of C_{α} ^{1}H, ^{15}N, ^{13}C chemical shift resonances and (B) are connections of C_{β} ^{1}H, ^{15}N, ^{13}C chemical shift resonances. In B, A19 is readily identified by its upfield shift of ca. 12 ppm.

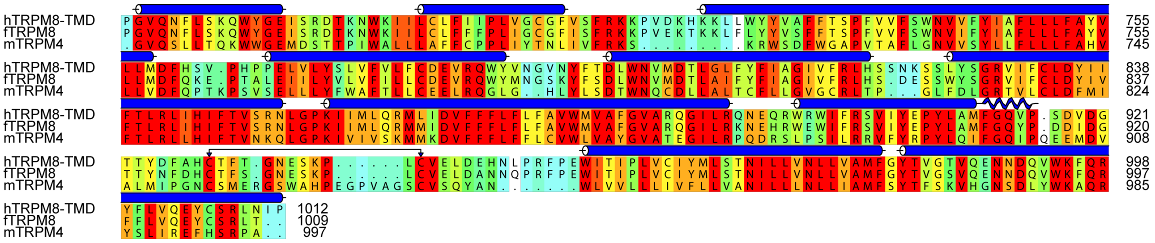

Figure S2.4 The sequence alignment of hTRPM8 to the templates. Sequence of fTRPM8 (PDB: 6BPQ) and mTRPM4 (PDB: 6BQV, 6BCL, 6BCJ, 5WP6, 6BCO) that were used as a template for the homology model generated in this study. Highlighted in blue cylinders are the α-helical section, in blue squiggly is the selectivity filter, and with arrow pointed down is the disulfide that was enforced.

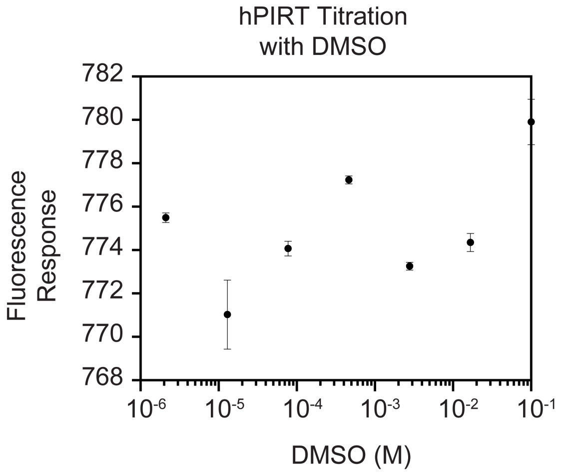

Figure S2.5 DMSO was used as a binding control for microscale thermophoresis. The conditions for this titration were matched to those used in the MST experiments used for PIP_2 and hTRPM8-S1S4 (see Experimental Methods). The lack of thermophoresis in a ligand dependent manor indicates that there is no PIRT binding to DMSO.

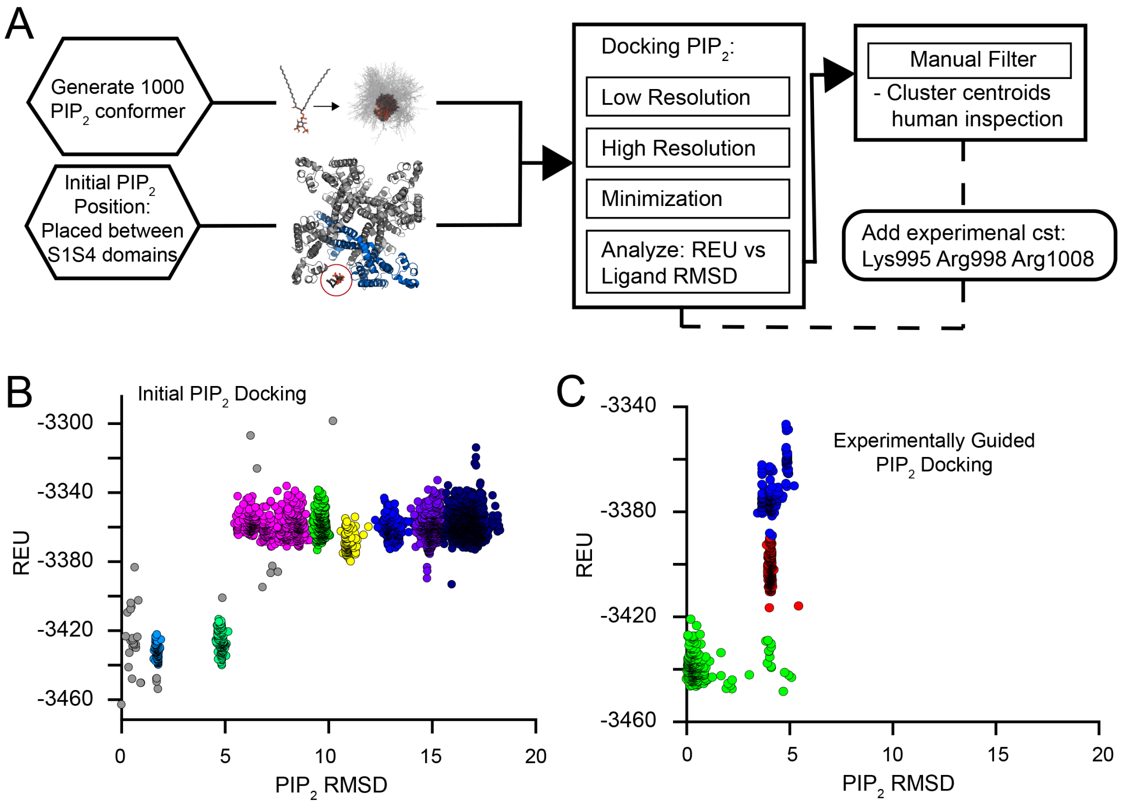

Figure S2.6 The general flow of Rosetta docking and score plots. (A) PIP$_2$ parameters are generated from 1000 conformers and the initial starting position is placed within a 10 Å radius from any contact with the TRPM8-TMD**.** Docking is carried out with 10,000 decoys of unrestrained Rosetta ligand docking in order to probe binding sites in the tetramer. The score vs RMSD (B) shows large coverage of PIP$_2$ conformational space, from which the centroids of the separate clusters (colored by cluster) were analyzed in PyMol. The next round of docking used the first round centroids as seed and enforced experimental evidence of PIP$_2$ sensitive amino acids to guide and refine the docking. In (C), the score vs RMSD shows relatively well converge clusters, from which 20 from each cluster were analyzed in PyMol and used as the TRPM8–PIP$_2$ docked model.

ROSETTA INPUT FILES AND COMMANDS

Rosetta was compiled using Rosetta release 3.8 with GNU compiler collection (gcc) and message passing interface (mpi) on CenOS 7 Linux distribution. The calculations were run on a combination of Intel Xeon Broadwell processors in the Van Horn lab or at the ASU Research Computing facility.

*The numbering for the comparative modeling is based on a starting amino acid P672 renamed to P1 for convenience in the following files and was later renumbered to P672.

-TRPM8 TM Span File-

```
TM region prediction
8 341
antiparallel
n2c
 23  35   23  35
 65  86   65  86
 94 117   94 117
120 145  120 145
157 179  157 179
190 215  190 215
233 244  233 244
285 310  285 310
```

-TRPM8 Disulfide Bond-

```
258 269
```

-Example Grishin Alignment FIle-

Alignment of hTRPM8-TMD to FaTRPM8.

```
## hTRPM8.pdb 6bpq.pdb
#
scores from program: 0
0
PGVQNFLSKQWYGEISRDTKNWKIILCLFIIPLVGCGFVSFRKKPVDKHKKLLWYYVAFFTSPFVV
FSWNVVFYIAFLLLFAYVLLMDFHSV-
PHPPELVLYSLVFVLFCDEVRQWYVNGVNYFTDLWNVMDTLGLFYFIAGIVFRLHSSNKSSLYSG
RVIFCLDYIIFTLRLIHIFTVSRNLGPKIIMLQRMLIDVFFFLFLFAVWMVAFGVARQGILRQNEQRW
RWIFRSVIYEPYLAMFGQVP-SDVDGTTYDFAHCTFT-GNESKP------
LCVELDEHNLPRFPEWITIPLVCIYMLSTNILLVNLLVAMFGYTVGTVQENNDQVWKFQRYFLVQ
EYCSRLNIP
0
PGVQNFLSKQWYGEISRDTKNWKIILCLFFFPLIGCGFISFRKKPVEKTKKLFLYYVSFFTSPFVVFS
WNVIFYIAFLLLFAYVLLMDFQKE-
```

```
PTALEIILYVLVFILLCDEVRQWYMNGSKYFSDLWNVMDTLAIFYFIAGIVFRLHS-
DESSWYSGRVIFCLDYIVFTLRLIHIFTVSRNLGPKIIMLQRMMIDVFFFLFLFAVWMVAFGVARQG
ILRKNEHRWEWIFRSVIYEPYLAMFGQYP-DDIDGTTYNFDHCTFS-GNESKP------
LCVELDANNQPRFPEWITIPLVCIYMLSTNILLVNLLVAMFGYTVGSVQENNDQVWKFQRFFLVQ
EYCSRLT--
```

-Threading-

```
$ROSETTA/bin/partial_thread.default.linuxgccrelease -in:file:fasta hTRPM8_TMD.fasta -in:file:alignment
hTRPM8_6bqv.grishin -in:file:template_pdb 6bqv.pdb

$ROSETTA/bin/partial_thread.default.linuxgccrelease -in:file:fasta hTRPM8_TMD.fasta -in:file:alignment
hTRPM8_6bpq.grishin -in:file:template_pdb 6bpq.pdb

$ROSETTA/bin/partial_thread.default.linuxgccrelease -in:file:fasta hTRPM8_TMD.fasta -in:file:alignment
hTRPM8_6bcj.grishin -in:file:template_pdb 6bcj.pdb

$ROSETTA/bin/partial_thread.default.linuxgccrelease -in:file:fasta hTRPM8_TMD.fasta -in:file:alignment
hTRPM8_6bco.grishin -in:file:template_pdb 6bco.pdb

$ROSETTA/bin/partial_thread.default.linuxgccrelease -in:file:fasta hTRPM8_TMD.fasta -in:file:alignment
hTRPM8_6bcl.grishin -in:file:template_pdb 6bcl.pdb

$ROSETTA/bin/partial_thread.default.linuxgccrelease -in:file:fasta hTRPM8_TMD.fasta -in:file:alignment
hTRPM8_5wp6.grishin -in:file:template_pdb 5wp6.pdb
```

-Creating Symmetric Definition for hTRPM8-TMD-

```
$ROSETTAHOME/source/src/apps/public/symmetry/make_symmdef_file.pl -m NCS -a A -i B -p
6bpq_TMD.pdb -r 1000.0 > TRPM8.symm
```

*where the TMD is the tetramer with residues 672-1012

-Experimental Restraint file for Docking-

```
# Block 1: for Lys or Arg to any Phosphate in PIP2
CST::BEGIN
  TEMPLATE::   ATOM_MAP: 1 atom_type: Phos
  TEMPLATE::   ATOM_MAP: 1 residue3: PIP

  TEMPLATE::   ATOM_MAP: 2 atom_type: Hpol ,
  TEMPLATE::   ATOM_MAP: 2 residue1:  KR
  CONSTRAINT:: distanceAB:   2.00  0.50 100.  0
CST::END
# loosely restraining a hydrogen bond distance
# These are to guide docking. The next option in
# the Rosetta Script is unrestrained perturbations.
# CONSTRAINT:: distance in A, VALUE, SD, Harmonic Weight, 0 = not covalent
# block 2 Constraint to enforce PIP2 depth by restraining
# distal PIP2 carbons in one hydrophobic tail to the middle of
# membrane


# Block 2: Constraint to enforce PIP2 depth by restraining
## distal PIP2 carbons in other hydrophobic tail to the middle of
```

```
## membrane
CST::BEGIN
  TEMPLATE::   ATOM_MAP: 1 atom_name: C15 C14 C16
  TEMPLATE::   ATOM_MAP: 1 residue3: PIP

  TEMPLATE::   ATOM_MAP: 2 atom_type: Hapol ,
  TEMPLATE::   ATOM_MAP: 2 residue1:  VA

  CONSTRAINT:: distanceAB:   5.00 2.00 100.  0
CST::END
# Block 3: Constraint to enforce PIP2 depth by restraining
## distal PIP2 carbons in other hydrophobic tail to the middle of
## membrane
CST::BEGIN
  TEMPLATE::   ATOM_MAP: 1 atom_name: C39 C38 C37
  TEMPLATE::   ATOM_MAP: 1 residue3: PIP

  TEMPLATE::   ATOM_MAP: 2 atom_type: Hapol ,
  TEMPLATE::   ATOM_MAP: 2 residue1:  VA

  CONSTRAINT:: distanceAB:   5.00  2.0 100.  0
#loosely restrained harmonic with large SD.

CST::END
```

-Rosetta CM-

```
# i/o
#
# Assuming Rosetta database path is set as $ROSETTA3_DB is set to
# $ROSETTAHOME/database
#
# Assuming Rosetta was compiled using gcc with MPI extras with
#
# scons -j NP mode=release extras=mpi bin; where NP is number of
# processors available.
#
# Command line to run this script is
#
# mpiexec -n NP rosetta_scripts.mpi.linuxgccrelease @rosetta_cm.options
#


-in:file:fasta fasta/hTRPM8_TMD.fasta
-parser:protocol rosetta_cml.xml

##########################
-nstruct 10000
-default_max_cycles 200 #
-out:file:scorefile 20180303_hTRPM8.fsc
-out:file:silent 20180303_hTRPM8.out
-out:file:silent_struct_type binary
#-out:output
-out::suffix _agave_v4_20180302_3
###########################

-ignore_unrecognized_res
# relax options
-relax:minimize_bond_angles
-relax:minimize_bond_lengths
-relax:jump_move true
-relax:min_type lbfgs_armijo_nonmonotone
-relax:jump_move true
#-relax:default_repeats 2
-score:weights stage3_rlx_membrane.wts
-use_bicubic_interpolation
-hybridize:stage1_probability 1.0
# EM Density
-edensity::mapfile em_map/emd_7127.map
-edensity::cryoem_scatterers
-edensity::mapreso 4.1
-edensity::grid_spacing 1.3
#
# reduce memory footprint
-chemical:exclude_patches LowerDNA  UpperDNA Cterm_amidation SpecialRotamer VirtualBB
ShoveBB VirtualDNAPhosphate VirtualNTerm CTermConnect sc_orbitals pro_hydroxylated_case1
pro_hydroxylated_case2 ser_phosphorylated thr_phosphorylated  tyr_phosphorylated tyr_sulfated
lys_dimethylated lys_monomethylated  lys_trimethylated lys_acetylated glu_carboxylated cys_acetylated
tyr_diiodinated N_acetylated C_methylamidated MethylatedProteinCterm
#Initialize membrane
```

```
-membrane
-in:file:spanfile ./span/hTRPM8_TMD.span
-membrane:no_interpolate_Mpair
-membrane:Menv_penalties
```

-Rosetta_cml.xml-

```
<ROSETTASCRIPTS>
   <TASKOPERATIONS>
   </TASKOPERATIONS>
   <SCOREFXNS>
      <ScoreFunction name="stage1" weights="stage1_membrane.wts" symmetric="1">
         <Reweight scoretype="atom_pair_constraint" weight="0.25"/>
         <Reweight scoretype="elec_dens_fast" weight="10"/>
      </ScoreFunction>
      <ScoreFunction name="stage2" weights="stage2_membrane.wts" symmetric="1">
         <Reweight scoretype="atom_pair_constraint" weight="0.25"/>
         <Reweight scoretype="elec_dens_fast" weight="10"/>
      </ScoreFunction>
      <ScoreFunction name="fullatom" weights="stage3_rlx_membrane.wts" symmetric="1">
         <Reweight scoretype="atom_pair_constraint" weight="0.25"/>
         <Reweight scoretype="elec_dens_fast" weight="25"/>
      </ScoreFunction>
   </SCOREFXNS>
   <FILTERS>
   </FILTERS>
   <MOVERS>
      <Hybridize name="hybridize" stage1_scorefxn="stage1" stage2_scorefxn="stage2"
fa_scorefxn="fullatom" batch="1" stage1_increase_cycles="1.0" stage2_increase_cycles="1.0"
linmin_only="0" realign_domains="0">
         <Fragments three_mers="./frags/hTRPM8_TMD_03_05.200_v1_3"
nine_mers="./frags/hTRPM8_TMD_09_05.200_v1_3"/>
         <Template pdb="../2_threading/threaded/hTRPM8_on_6bqv.pdb" cst_file="AUTO"
weight="1.000" symmdef="../symmetry/TRPM8.symm"/>
         <Template pdb="../2_threading/threaded/hTRPM8_on_6bcl.pdb" cst_file="AUTO" weight="1.000"
symmdef="../symmetry/TRPM8.symm"/>
         <Template pdb="../2_threading/threaded/hTRPM8_on_6bpq_v3.pdb" cst_file="AUTO"
weight="1.000" symmdef="../symmetry/TRPM8.symm"/>
         <Template pdb="../2_threading/threaded/hTRPM8_on_6bcj_v3.pdb" cst_file="AUTO"
weight="1.000" symmdef="../symmetry/TRPM8.symm"/>
         <Template pdb="../2_threading/threaded/hTRPM8_on_5wp6.pdb" cst_file="AUTO"
weight="1.000" symmdef="../symmetry/TRPM8.symm"/>
         <Template pdb="../2_threading/threaded/hTRPM8_on_6bco.pdb" cst_file="AUTO"
weight="1.000" symmdef="../symmetry/TRPM8.symm"/>
         <DetailedControls start_res="289" stop_res="294" sample_template="0" sample_abinitio="1"/>
      </Hybridize>
   </MOVERS>
   <APPLY_TO_POSE>
   </APPLY_TO_POSE>
   <PROTOCOLS>
      <Add mover="hybridize"/>
   </PROTOCOLS>

</ROSETTASCRIPTS>
```

-Refinement Options-

```
#i/o
#
# Assuming Rosetta database path is set as $ROSETTA3_DB is set to
# $ROSETTAHOME/database
#
# Assuming Rosetta was compiled using gcc and MPI extras with
#
# scons -j NP mode=release extras=mpi bin; where NP is number of
# processors available.
#
# Command line to run this script is
#
# mpiexec -n NP relax.mpi.linuxgccrelease @rosetta_cm.options
#
#
#

#### User Input #####
-in:file:l clean_list
-in::file::spanfile ../../3_hybridize/span/hTRPM8_TMD.span #read predicted transmembrane regions
-out:suffix _relax_em_cluster1
-out:file:silent 20180307_relax_cluter1.out
-out:file:scorefile cluster1_score_raw.out
-symmetry:symmetry_definition ../../symmetry/TRPM8_em.symm
-nstruct 1
###################
#
-in:fix_disulf ../disulf.cst #read disulfide connectivity information
-detect_disulf true
-detect_disulf_tolerance 2
-ex1
-ex2
-membrane:no_interpolate_Mpair # membrane scoring specification
-membrane:Menv_penalties       # turn on membrane penalty scores
-score:weights membrane_highres_Menv_smooth.wts
-relax:thorough
-relax:dualspace              #use dualspace relax protocol
-relax:minimize_bond_angles    #dualspace relax protocol setting
-set_weights cart_bonded .5 pro_close 0 #score proline ring closure using energy term for all bond lengths
(pro_close uses virtual atom NV for proline ring scores)
-default_max_cycles 200

# EM Density
-edensity::mapfile ../../3_hybridize/em_map/emd_7127.map
-edensity::cryoem_scatterers
-edensity::fastdens_wt 25.0
-edensity::mapreso 4.1
-edensity::grid_spacing 1.3
-crystal_refine
```

-Rosetta Docking Options-

```
# Adopted from Ligand Docking from
# $ROSETTAHOME/demos/tutorials/ligand_docking/
#Pound signs indicate comments

#-in:file:s option imports the protein and ligand PDB structures
#-in:file:extra_res_fa option imports the parameters for the ligand
#
# Prepare a pdb file that has the ligand and protein in the same file.
-in
 -file
  -s M8_tet_pip2_1_ignorechain.pdb # PIP2 is chain X
  -extra_res_fa PIP.params #location of PIP2 parameter file

# Params file generated by the following script available in Rosetta3
# $ROSETTAHOME/main/source/scripts/python/public/molfile_to_params.py -n PIP -p PIP --conformers-
in-one-file pip2.sdf

#the packing options allow Rosetta to sample additional rotamers for
#protein sidechain angles chi 1 (ex1) and chi 2 (ex2)
#no_optH false tells Rosetta to optimize hydrogen placements
#flip_HNQ tells Rosetta to consider HIS,ASN,GLN hydrogen flips
#ignore_ligand_chi prevents Roseta from adding additional ligand rotamer

-packing
 -ex1
 -ex2
 -ex1aro
 -no_optH false
 -flip_HNQ true
 -ignore_ligand_chi true


#parser:protocol locates the XML file for RosettaScripts

-parser
 -protocol dock_X.xml # change to .xml for initial or restrained

#overwrite allows Rosetta to write over previous structures and scores
-overwrite

#Ligand docking is not yet benchmarked with the updated scoring function
#This flag restores certain parameters to previously published values

-mistakes
 -restore_pre_talaris_2013_behavior true
#
-nstruct 1 # 10000 or 1000 for probe vs refine respectively
-qsar:grid_dir grid_dir/ # Make this directory before running, can speed up docking if
                    # a grid has been used previously.
-run:preserve_header # Add this to enforce the experimental restraints in pdb header
```

-Rosetta Initial Docking XML-

```
<ROSETTASCRIPTS>

  <SCOREFXNS>
   <ScoreFunction name="ligand_soft_rep" weights="ligand_soft_rep">
    Reweighted based on "An integrated framework advancing membrane protein modeling and design
Alford, RF, et al.
    <Reweight scoretype="fa_elec" weight="0.42"/>
    <Reweight scoretype="hbond_bb_sc" weight="2.34"/>
    <Reweight scoretype="hbond_sc" weight="2.2"/>
    <Reweight scoretype="rama" weight="0.2"/>
   </ScoreFunction>
   <ScoreFunction name="hard_rep" weights="ligand">
    <Reweight scoretype="fa_intra_rep" weight="0.004"/>
    <Reweight scoretype="fa_elec" weight="0.42"/>
    <Reweight scoretype="hbond_bb_sc" weight="2.34"/>
    <Reweight scoretype="hbond_sc" weight="2.2"/>
    <Reweight scoretype="rama" weight="0.2"/>
   </ScoreFunction>
  </SCOREFXNS>

  <LIGAND_AREAS>
   <LigandArea name="inhibitor_dock_sc" chain="X" cutoff="6.0" add_nbr_radius="true"
all_atom_mode="false"/>
   <LigandArea name="inhibitor_final_sc" chain="X" cutoff="6.0" add_nbr_radius="true"
all_atom_mode="true"/>
   <LigandArea name="inhibitor_final_bb" chain="X" cutoff="7.0" add_nbr_radius="false"
all_atom_mode="true" Calpha_restraints="0.3"/>
  </LIGAND_AREAS>

  <INTERFACE_BUILDERS>
   <InterfaceBuilder name="side_chain_for_docking" ligand_areas="inhibitor_dock_sc"/>
   <InterfaceBuilder name="side_chain_for_final" ligand_areas="inhibitor_final_sc"/>
   <InterfaceBuilder name="backbone" ligand_areas="inhibitor_final_bb" extension_window="3"/>
  </INTERFACE_BUILDERS>

  <MOVEMAP_BUILDERS>
   <MoveMapBuilder name="docking" sc_interface="side_chain_for_docking" minimize_water="false"/>
   <MoveMapBuilder name="final" sc_interface="side_chain_for_final" bb_interface="backbone"
minimize_water="false"/>
  </MOVEMAP_BUILDERS>

  <SCORINGGRIDS ligand_chain="X" width="15">
   <HbdGrid grid_name="classic" weight="1.0"/> Hydrogen bond donating grid
  </SCORINGGRIDS>

  <MOVERS>
   <Transform name="transform" chain="X" box_size="10.0" move_distance="0.2" angle="20"
cycles="10" repeats="1" temperature="5"  />
   <HighResDocker name="high_res_docker" cycles="50" repack_every_Nth="2"
scorefxn="ligand_soft_rep" movemap_builder="docking"/>
   <FinalMinimizer name="final" scorefxn="hard_rep" movemap_builder="final"/>
   <InterfaceScoreCalculator name="add_scores" chains="X" scorefxn="hard_rep"
native="M8_tet_pip2_1_ignorechain_0193_0001.pdb"/>
```

```
  </MOVERS>

  <PROTOCOLS>
   <Add mover_name="transform"/> Large 10 angstrom Monte Carlo spherical perturbation
   <Add mover_name="high_res_docker"/>
   <Add mover_name="final"/>
   <Add mover_name="add_scores"/>
  </PROTOCOLS>


</ROSETTASCRIPTS>
```

-Rosetta Restrained Docking XML-

```
<ROSETTASCRIPTS>

  <SCOREFXNS>
   <ScoreFunction name="ligand_soft_rep" weights="ligand_soft_rep">
    Reweighted based on "An integrated framework advancing membrane protein modeling and design
Alford, RF, et al.
    <Reweight scoretype="fa_elec" weight="0.42"/>
    <Reweight scoretype="hbond_bb_sc" weight="2.34"/>
    <Reweight scoretype="hbond_sc" weight="2.2"/>
    <Reweight scoretype="rama" weight="0.2"/>
   </ScoreFunction>
   <ScoreFunction name="hard_rep" weights="ligand">
    <Reweight scoretype="fa_intra_rep" weight="0.004"/>
    <Reweight scoretype="fa_elec" weight="0.42"/>
    <Reweight scoretype="hbond_bb_sc" weight="2.34"/>
    <Reweight scoretype="hbond_sc" weight="2.2"/>
    <Reweight scoretype="rama" weight="0.2"/>
   </ScoreFunction>
  </SCOREFXNS>

  <LIGAND_AREAS>
   <LigandArea name="inhibitor_dock_sc" chain="X" cutoff="6.0" add_nbr_radius="true"
all_atom_mode="false"/>
   <LigandArea name="inhibitor_final_sc" chain="X" cutoff="6.0" add_nbr_radius="true"
all_atom_mode="true"/>
   <LigandArea name="inhibitor_final_bb" chain="X" cutoff="7.0" add_nbr_radius="false"
all_atom_mode="true" Calpha_restraints="0.3"/>
  </LIGAND_AREAS>

  <INTERFACE_BUILDERS>
   <InterfaceBuilder name="side_chain_for_docking" ligand_areas="inhibitor_dock_sc"/>
   <InterfaceBuilder name="side_chain_for_final" ligand_areas="inhibitor_final_sc"/>
   <InterfaceBuilder name="backbone" ligand_areas="inhibitor_final_bb" extension_window="3"/>
  </INTERFACE_BUILDERS>

  <MOVEMAP_BUILDERS>
   <MoveMapBuilder name="docking" sc_interface="side_chain_for_docking" minimize_water="false"/>
   <MoveMapBuilder name="final" sc_interface="side_chain_for_final" bb_interface="backbone"
minimize_water="false"/>
  </MOVEMAP_BUILDERS>

  <SCORINGGRIDS ligand_chain="X" width="15">
   <HbdGrid grid_name="classic" weight="1.0"/> Hydrogen bond donating grid
  </SCORINGGRIDS>

  <MOVERS>
   <Transform name="transform_after_cst" chain="X" box_size="1.0" move_distance="0.2" angle="5"
cycles="10" repeats="1" temperature="3"  />
   <HighResDocker name="high_res_docker" cycles="50" repack_every_Nth="2"
scorefxn="ligand_soft_rep" movemap_builder="docking"/>
   <FinalMinimizer name="final" scorefxn="hard_rep" movemap_builder="final"/>
   <InterfaceScoreCalculator name="add_scores" chains="X" scorefxn="hard_rep"
native="M8_tet_pip2_1_ignorechain_0193_0001.pdb"/>
```

```
   <AddOrRemoveMatchCsts name="cst" cst_instruction="add_new" cstfile="pip2_v2.cst" />
  </MOVERS>

  <PROTOCOLS>
   Add mover_name="cst" />
   <Add mover_name="transform_after_cst" /> small 1 angstrom Monte Carlo spherical perturbation after
experimental restraints
   <Add mover_name="high_res_docker"/>
   <Add mover_name="final"/>
   <Add mover_name="add_scores"/>
  </PROTOCOLS>


</ROSETTASCRIPTS>
```

CHAPTER 3

PIRT Ligand Screen Suggests Novel Regulation of Ion Channels

3.1 Introduction

Transient receptor potential (TRP) ion channels respond to a variety of different stimuli with links to pain, obesity, and cancer.[2-6, 89] The heat sensing TRPV1 is modulated by capsaicin, calcium binding proteins S100A1 and calmodulin, PIP_2, and PIRT (phosphoinositide interaction regulator of TRPs).[14, 16, 17, 65, 90, 91] PIRT was originally identified as a TRP channel regulator with evidence showing that it bound phosphoinositides. It was shown to increase mouse sensitivity to TRPV1 stimuli by enhancing TRPV1-dependent currents and it was identified to express in dorsal root ganglia and trigeminal ganglia of the peripheral nervous system with implications in neuropathic pain regulation.[14, 65] PIRT regulates TRPV1-dependent uterine contraction pain and regulates other ion channels including P2X3 with implications in overactive bladder regulation.[17, 18] Additionally, PIRT is a regulatory subunit for the cold sensing ion channel TRPM8, where human PIRT significantly decreases human TRPM8 dependent conductance and that this is due to competitive binding to PIP_2 by sequestering the lipid from TRPM8 described in Chapter 2.[61] Like TRPV1 and many other ion channels, TRPM8 is regulated by calmodulin.[10, 30, 83, 90, 92-94] TRPM8 and TRPV1 are functionally different, yet both respond to PIRT, calmodulin, and PIP_2 to alter their channel activity. Herein, a predicted calmodulin binding site in human PIRT is identified and interrogated with results that suggest a mechanism of calmodulin regulation of TRP channels that includes PIRT. PIRT was also subjected to ligand screening with MST where several binding partners were identified suggesting it regulates TRP channel functions possibly through modulating TRP channel ligand access.

The highly conserved and ancient calcium sensor named calmodulin (CaM) is a known ion channel modulator.[92, 94] In the context of TRP channels, CaM downregulates Ca^{2+}-permeable cation channels including TRP channels,[89] where it acts as a negative feedback mechanism to prevent excessive calcium influx.[89] In TRPV1, CaM competes for a binding site with another calcium binding protein called S100A1. [90] Recently, the TRPV6 structure was determined using cryo-electron microscopy (cryo-EM) with a bound CaM revealing a 2:1 CaM:TRPV6-tetramer stoichiometry.[93] Remarkably, the position CaM occupies in the TRPV6 structure is located in a region where the structurally homologous TRPM8 is thought to bind PIP_2;[32] in Chapter 2 PIP_2 was docked to this region. In TRPM8, CaM desensitizes TRPM8 channel conductance and PIP_2 is essential for CaM-dependent downregulation.[10] Despite this study observing calcium influx leading to CaM and PIP_2-dependent desensitization for TRPM8 currents, it did not address any PIRT specific interactions with CaM or PIP_2. PIRT may have a yet to be determined role in CaM dependent TRPM8 channel regulation.

Shown in Chapter 2, we identified that the structure of PIRT contains an amphipathic α-helix in the C-terminal helix that binds directly to the TRPM8 ligand-sensing domain. In this chapter, this C-terminal helix is identified to contain a conserved calmodulin binding motif, which is tested using microscale thermophoresis (MST) and nuclear magnetic resonance spectroscopy (NMR) to measure the binding affinity of CaM to PIRT. Furthermore, we show that apo-calmodulin (apo-CaM, no bound Ca^{2+}) binds to

PIRT with more affinity than calcium bound CaM (holo-CaM, bound Ca^{2+}) suggesting PIRT releases holo-CaM when intracellular calcium increases.

With the identification of PIRT as a membrane protein capable of binding PIP_2, TRPM8, TRPV1, P2X3, and now calmodulin; we propose that it may have additional binding partners. We used microscale thermophoresis (MST) to perform a ligand screen for hPIRT and identify that it binds to many ligands including: oxytocin (chosen due to observations of PIRT involvement in uterine contraction pain[17]), β-estradiol, cortisol, and cholesteryl-hemisuccinate (cholesterol-like ligands chosen after identification of a conserved cholesterol binding motif[95, 96]). The ability of hPIRT to bind these ligands in isolation suggests that hPIRT is a general ion channel modulator in vivo.

3.2 Materials and Methods

3.2.1 Expression and Purification of hPIRT

The expression and purification of hPIRT was carried out following the established protocols in previous work on hPIRT and described in Chapter 2.

3.2.2 Expression and Purification of Calmodulin

For NMR experiments with 15N-hPIRT titrated with calmodulin, calmodulin was expressed at 37 ˚C with a hexahistidine tag comprising MGHHHHHHG- in a pET29 vector and grown in BL21 (DE3) cells with M9 minimal media. For NMR studies, ^{15}N-ammonium chloride was used as the sole nitrogen source. The cells were induced at $OD_{600} = 0.6$ with an IPTG concentration of 500 mM. The cells were pelleted after five hours of induction at 6000 ×g for 20 min, which resulted in 3 grams of cellular mass per 500 mL.

The cells were resuspended and homogenized by tumbling for one hour in lysis buffer consisting of lysozyme (0.2 mg/mL), RNase (0.02 mg/mL), DNase (0.02 mg/mL), 1 mM phenylmethanesulfonylfluoride (PMSF, Sigma-Aldrich), 5 mM magnesium acetate (Sigma-Aldrich), 50 mM HEPES (Sigma-Aldrich) pH 7.7 and 300 mM NaCl (Sigma-Aldrich). The suspended cells were lysed using a sonicator at 50% duty cycle and 50% amplitude for 7.5 min total on time. Cellular debris was removed with centrifugation of cell lysate at 38,000 ×g for 20 min and the pellet was discarded. The supernatant was used for the following steps. The supernatant was tumbled for 1 hour with 2 mL of lysis buffer (50 mM HEPES (Sigma-Aldrich) pH 7.7 and 300 mM NaCl (Sigma-Aldrich)) preequilibrated Ni-NTA (QIAGEN: 2 mL of resin/g of pellet) in a gravity column. Purification was then carried with a flow-through buffer (50 mM HEPES pH 7.5), low imidazole wash (50 mM HEPES pH 7.5, 10 mM imidazole), and an then an elution buffer (50 mM HEPES pH 7.5, 300 mM imidazole). Following Ni-NTA, size exclusion using Superdex 200 (GE Healthcare Life Sciences) 60 mL column volume was used, to which calmodulin purity was assessed with SDS-PAGE and identity by western blow analysis with a penta-histidine primary antibody and anti-mouse alkaline phosphatase detection. (Figure S3.1)

3.2.3 Nuclear Magnetic Resonance

All U-^{15}N - Human PIRT (180 µL, 3 mm NMR tube) and U-^{15}N - human Calmodulin (550 µL, 5 mm NMR tube) were measured in NMR buffer (4% D_2O (v/v, Sigma Aldrich), 20 mM sodium phosphate (Fisher Scientific), 500 µM DSS (Sigma Aldrich), and 0.2 mM EDTA (Sigma Aldrich) at pH 6.5) on a Bruker 850 MHz ^{1}H magnet with

Avance III console running the latest Topspin patch. 2048 × 128 direct and indirect points, respectively, were collected with 128 transients. Optimization of NMR conditions for hPIRT was previously carried out resulting in dodecylphosphocholine (DPC) as the most suitable detergent for investigations with hPIRT and at a temperature of 40 °C.

3.2.4 Microscale Thermophoresis

Human PIRT was labeled according to previous protocols described in Chapter 2. For the MST measurements, the concentration of hPIRT was kept consistent for all ligands at 200 nM in a reaction buffer comprising 0.1% DPC (w/v) 50 mM HEPES at pH 7.0; apo-CaM had an additional 0.5 mM EDTA.

Cortisol, estradiol, testosterone, menthol, cholesteryl-hemisuccinate, and cholecalciferol were all solubilized to 1M in 100% chloroform. From the 1M stocks of these compounds, the desired amount for MST was pipetted into individual small reaction conical tubes, from which the methanol was evaporated off under N_2(g) at room temperature. The compounds were then resuspended in reaction buffer with 200 nM hPIRT. The disposal of testosterone was carried out according to DEA standards. Water soluble oxytocin and vasopressin stocks were prepared to 20 mM in reaction buffer and aliquoted into small conical reaction tubes (PCR reaction tubes). Calcium chloride, nicotinamide, and DMSO stocks were prepared to 1 M in the reaction buffer and aliquoted to the desired concentrations. Once the ligands were in the reaction tubes, hPIRT was added to 200 nM and incubated for 1 hour. After incubation, a standard MST glass capillary tube from NanoTemper was placed inside the conical vial containing the binding mixtures where approximately 5 μL of sample was drawn into the tube by capillary action. The tubes were then loaded onto the MST tray. The measurements were carried out in triplicate at room temperature with 50% infrared laser power and green channel using 10% excitation power.

All of the data from the MST ligand screen that showed ligand-dependent thermophoresis, ligand-independent thermophoresis is evident in the controls (Figure S3.1), were normalized to free hPIRT and bound hPIRT according to previous protocols,[45, 66] from which the dissociation constant was calculated. Ligand titration concentrations were optimized to show saturation and minima within the bounds of solubility; i.e. the cholesterol-like ligands tended to become insoluble above the concentrations used. The data were fit in MATLAB_R2017a with the nlinfit function where the covariance B matrix output was used to calculate the standard deviation of the fit according to the square root along the diagonal of this matrix.

3.3 Results

3.3.1 hPIRT Ligand Screening with Microscale Thermophoresis

The ligand binding screen on hPIRT was carried out to investigate additional hPIRT binding partners. With our data, we show that hPIRT directly binds to a milieu of ligands that are known regulators of the proteins that hPIRT binds. Table 3.1 summarizes the binding affinities for the new binding partners, as well as our previously identified PIP_2 and hTRPM8-SD affinities. Notably, hPIRT has 10× more affinity to apo-CaM (Figure 3.1A) than for holo-CaM within a buffer containing 10 μM $CaCl_2$ (Figure 3.1B). This suggests that hPIRT may release CaM when in transitions from apo-CaM to holo-CaM (Figure 3.1C and Figure3.1D). As a control, hPIRT does not bind to $CaCl_2$ (Figure S3.1).

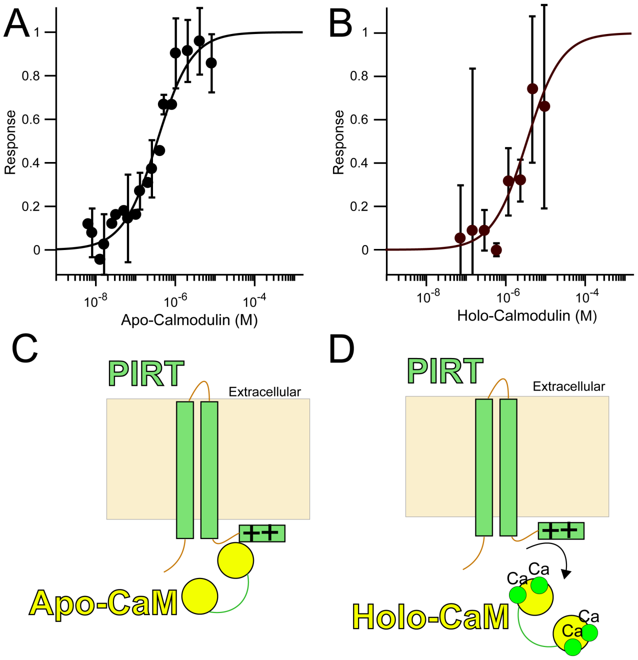

Figure 3.1 MST-detect hPIRT titration with apo-calmodulin and holo-calmodulin. A) Apo-Calmodulin was titrated with hPIRT to investigate the binding affinity for hPIRT with affinity of (351 ± 38.0) × 10^{-9} M. B) With high concentrations of $CaCl_2$, calmodulin is predominately holo-calmodulin and the affinity for hPIRT is right shifted with an affinity of (3.7 ± 0.7) × 10^{-6} M. C) Cartoon depiction of how hPIRT might bind to holo-calmodulin and in D) hPIRT may lose affinity for holo-calmodulin and release hPIRT.

Specificity for hPIRT binding is also evident with respect to oxytocin which shows binding, but Arg8-vasopressin does not (Figure S3.2). TRPM8 and PIP_2 binding were analyzed and discussed in Chapter 2 and are shown here for comparison. The affinity for cholesteryl-hemisuccinate appears to be tighter than that for cortisol and β-estradiol, but this may be due to the added hemisuccinate group to make it more soluble. Menthol binds with low affinity, however this new finding presents interesting avenues of drug development through SAR-NMR.[97]

3.3.2 NMR Titration Identifies Binding Residues that Include the Predicted Calmodulin Binding Site

Table 3.1 Human PIRT MST Detected Ligand Screen Affinities

LIGAND	K_d (M)	ERROR (M)	LIGAND TYPE
APO-CALMODULIN	351×10^{-9}	38×10^{-9}	Intracellular Protein
TRPM8	856×10^{-9}	11×10^{-9}	Membrane Protein
HOLO-CALMODULIN	3.7×10^{-6}	0.7×10^{-6}	Intracellular Protein
OXYTOCIN	7.37×10^{-6}	1.47×10^{-6}	Peptide Hormone
PIP_2	39.3×10^{-6}	5.0×10^{-6}	Secondary Messenger Lipid
CHOLESTERYL	103×10^{-6}	6×10^{-6}	Steroid Hormone Precursor
CORTISOL	785×10^{-6}	54×10^{-6}	Cortical Steroid Hormone
ESTRADIOL	819×10^{-6}	145×10^{-6}	Sex Steroid Hormone
CHOLECALCIFEROL	2.07×10^{-3}	0.37×10^{-3}	Ketosteroid Hormone
MENTHOL	7.49×10^{-3}	1.35×10^{-3}	Topical Drug

NMR titrations of hPIRT with CaM was carried out in 0.5 mM EDTA to chelate any unbound metal ions, including Ca^{2+}, in an attempt to confine CaM to apo-CaM. Chemical shift perturbations for apo-CaM (Figure 3.2A) showing binding within the C-terminal α-helix (Figure 3.2B) with S124 showing perturbations suggestive of slow exchange. The predicted binding site for calmodulin (Figure3.2C). The Calmodulin Target Database[98] was used to predict the calmodulin binding site in hPIRT, which was predicted that hPIRT would bind CaM between 112 and 129. With careful analysis of the sequence, it was identified that hPIRT contains a 1-14 motif with a consensus sequence motif of -(FILVW)xxxxxxxxxxxx(FILVW)-, x is any amino acid and the parentheses signify one of those amino acids at 1 and 14 position in the motif.[99]

3.3.4 hPIRT Contains a Conserved Cholesterol Binding Domain that Binds Cholesterol-like Molecules

The CRAC-CARC domains are conserved membrane protein motifs that bind cholesterol.[95, 96] hPIRT contains a CARC domain located on the N-terminal side of TM1. This region is located in outer leaflet of the membrane bilayer. This was used as incentive to probe hPIRT for binding cholesteryl-hemisuccinate, cortisol, estradiol, and cholecalciferol (Table 3.1, Figure S3.5A, B, F, and H respectively), which are all steroid hormones or steroid-like. Testosterone was investigated as well but was not shown to bind to hPIRT (Figure S3.5A).

3.3.4 hPIRT Ligand Screen Identifies Specificity of Binding Oxytocin over Arg-8-Vasopressin

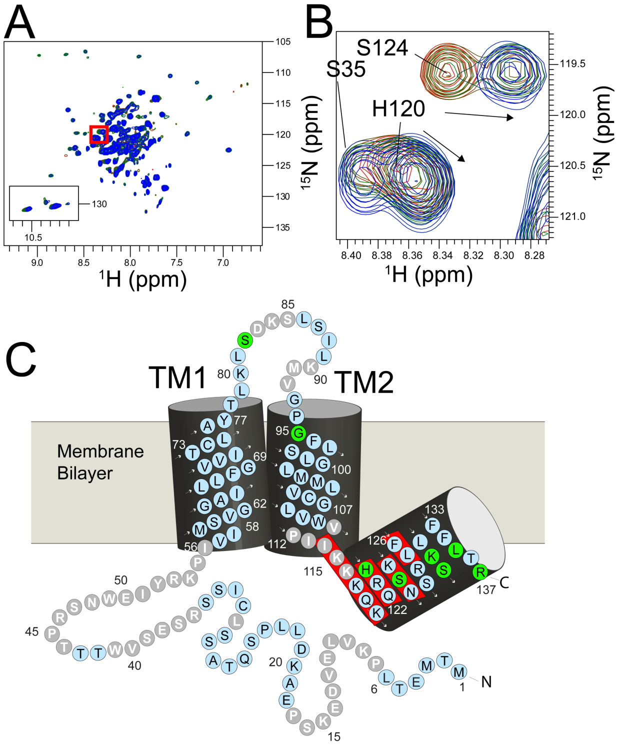

Figure 3.2 NMR-detect hPIRT titration with apo-calmodulin. A) ^{14}N-Calmodulin was titration with ^{15}N-hPIRT to investigate the binding site in hPIRT. B) The MST detected binding suggest tight binding, and residue S124 is apparent slow exchange that is suggestive of tight binding. C) The hPIRT topology with predicted calmodulin binding site shown in red. Blue circles denote assigned amino acid resonances, gray is no assignment, and green indicate tight binding to calmodulin.

The MST ligand binding screen identified that oxytocin binds to hPIRT while the structurally similar vasopressin does not. Oxytocin was chosen as a screening molecule due to a recent study identifying that oxytocin induced uterine contraction pain is reduced in mice with PIRT knocked out.[17] Oxytocin was determined to bind to hPIRT (Table 3.1, Figure S3.5C) while Arg-8-vasopressin did not (Figure S3.3).

3.4 Discussion

Human PIRT was subjected to an MST-detected ligand screen and identified to bind several ligands (Table 3.1). Notably, one of the ligands was CaM, which was predicted to bind to the C-terminal α-helix. We further tested hPIRT binding to CaM with NMR titrations and with our previously assigned resonances from Chapter 2, the specific location of CaM binding was determined to be within this predicted region (Figure 3.1C). With respect to CaM binding, it is notable that hPIRT affinity for CaM is reduced by 10× with high concentrations of $CaCl_2$, suggestive that apo-CaM is binding to Ca^{2+} and releasing hPIRT at high $CaCl_2$ concentrations.

Apo-CaM binding to hPIRT can be used to expand on known CaM downregulation of TRPM8.[10] With the structurally homologous TRPM4 structure as a model, Ca^{2+} is bound to the SD (S1-S4) chelated Ca^{2+} with Glu828, Gln831, Asn865, and Asp868 to prime the channel for voltage gating.[100] These amino acids, as well as Tyr859 and Glu1068 are conserved for all Ca^{2+} dependent TRP channels.[100-103] This conservation for Ca^{2+} dependent TRP channels, and their structural homology, suggest that TRPM8 potentially binds to Ca^{2+} in the same location and potentially has a similar effect on the channel. In TRPM8 channels specially, high levels of intracellular Ca^{2+} causes CaM downregulation of TRPM8 with a mechanism that depends on PIP_2.[10]

We previously showed that hPIRT reduces the human TRPM8-dependent currents by binding directly to the hTRPM8-SD[61] and sequestering PIP_2 (Chapter 2), and this mechanism is plausible for PIP_2 specific inactivation of TRPM8. The data in this Chapter supports a new mechanism that can explain CaM, PIP_2, Ca^{2+}, and hPIRT downregulation of TRPM8 dependent currents. With low intracellular Ca^{2+} levels (inactive TRPM8), apo-CaM binds to hPIRT (Figure 3.2,1) where PIP_2 can be bound to hTRPM8 or hPIRT. As cellular Ca^{2+} levels increase, hTRPM8-SD and apo-CaM bind Ca^{2+} causing holo-CaM to release hPIRT (Figure 3.2, 2). hPIRT shuttles PIP_2 to TRPM8 and then binds to the SD (Figure 3.2,2). Ca^{2+}-dependent channel hTRPM8 conductance is then downregulated by holo-CaM binding to TRPM8 sequestering Ca^{2+} from the SD (Figure 3.2,3). Regeneration of apo-CaM overwhelms the intracellular Ca^{2+} levels causing Ca^{2+} to be released from the SD, apo-CaM then binds to hPIRT, and PIP_2 is regenerated leading to inactive hTRPM8 (Figure 3.2,4). More studies that test the intricacies of the proposed mechanism are needed but our data support a more detailed negative regulation from Ca^{2+} for TRPM8-dependent currents.

The additional results from our binding screen identify several ligands for hPIRT with potential regulatory functions on other ion channels. The conserved cholesterol binding domain CARC[96] was identified in the sequence of hPIRT, which we show binds to cholesterol-like molecules. Interestingly, while β-estradiol (female sex hormone) binds tightly to hPIRT, testosterone (male sex hormone) shows no evidence of binding and may expand the role hPIRT plays in uterine contraction pain.[17] Additionally, cholecalciferol

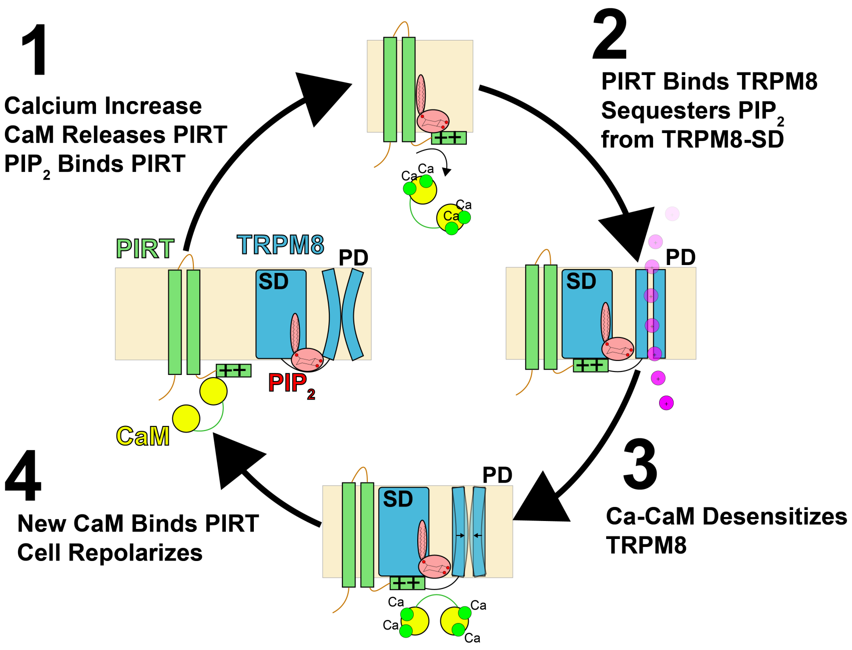

Figure 3.3 The mechanism of TRPM8 negative regulation from calmodulin and PIRT. 1) PIRT binds to apo-calmodulin (CaM). As calcium increases from calcium permeable ion channels, CaM releases PIRT where PIRT binds to PIP_2 (2), which both bind to TRPM8 and potentiate TRPM8. 3) Ca-CaM desensitized TRPM8 by sequestering calcium from binding to the sensing domain. 4) The cycle starts over as new protein is remade.

(Vitamin D_3) was identified to bind to hPIRT, which is a hormone synthesized in skin due to UV radiation from the Sun exposure and is intimately involved in bone formation with recent research on dietary calcium and vitamin D_3 being shown to regulate the epithelial ion channels TRPV6 and TRPV5.[104] It is unknown what role PIRT would directly have on TRPV6 and TRPV5; however, based on emerging evidence of PIRT as a general TRP channel regulator, it is plausible that PIRT regulates TRPV5 and TRPV6 in concert with the calcium sensor CaM.

Binding to cholesteryl-hemisuccinate supports in vivo electrophysiology measurements where PIRT was shown to interact with the TRPM8 pore domain.[61]

TRPM8 is known to interact with cholesterol and partition to micro-domains (cholesterol rich membrane regions),[8] and cholesteryl-hemisuccinate was bound in the cryo-EM structure of the structurally homologous TRPM4.[100] With this physiological and structural data, and our cholesterol binding data and bioinformatics, another layer of PIRT interaction with TPRM8 was identified in a cholesterol-dependent manner.

PIRT was shown to be important for uterine contraction pain under oxytocin inclult during birth in mice.[17] PIRT was identified in this Chapter to bind to oxytocin with data showing the specificity of oxytocin binding over Arg8-vasopressin, of which both are cyclic nona-peptides with a difference of only two amino acids. It is notable that these hormones have drastically different roles in endocrinology controlling birth induction and blood pressure regulation respectively. In fact, oxytocin induced child birth can result in off target effects complicating child birth that are thought to be caused by similarity of these hormone structures.[105, 106] These effects are not fully understood but with the identification of hPIRT specificity between these hormones, potentially new avenues to understand these side effects can be investigated.

The data presented in this Chapter have identified several binding partners for hPIRT with specific endocrinology roles as well as an enhanced model for hTRPM8 regulation. These are the first data to suggest hPIRT binds more than TRP channels or PIP_2 and opens multiple avenues of additional hPIRT research.

3.5 Supplementary Information

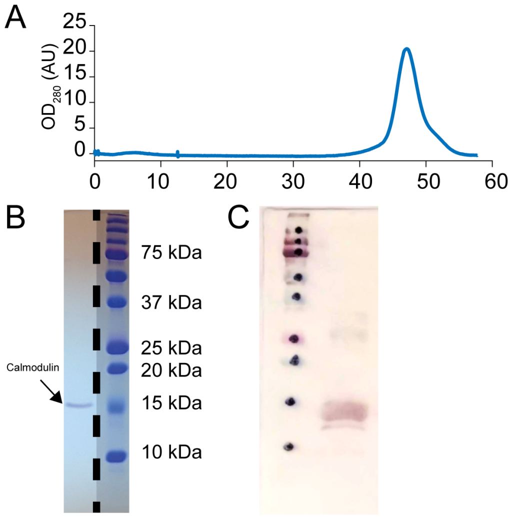

Figure S3.1 Calmodulin purification. A) Size exclusion profile shows a homogeneous calmodulin with a retention volume of 47 mL corresponding to a MW of ca. 16 kDa. B) SDS-PAGE from the SEC purification shows a highly pure protein with C showing His tag antibody detection of calmodulin.

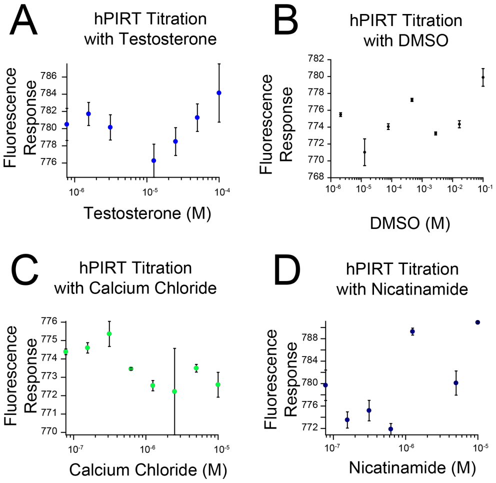

Figure S3.2 Microscale thermophoresis controls. A shows hPIRT titrated with testosterone as a steroid ligand control, B) is a control for DMSO that was used as a vehicle for PIP_2, C) hPIRT titration of $CaCl_2$ as a control for holo-CaM titrations, and D) hPIRT titration with nicotinamide as a biological ligand control.

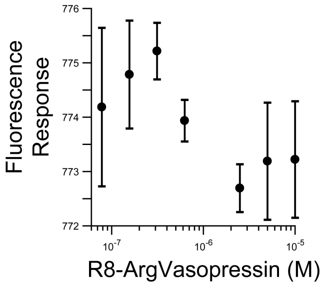

Figure S3.3 Arg8-vasopressin thermophoresis does not appear to be ligand dependent. Arg-8 vasopressin shows thermophoresis, measured in triplicate. Error bars signify the spread of data for each measurement.

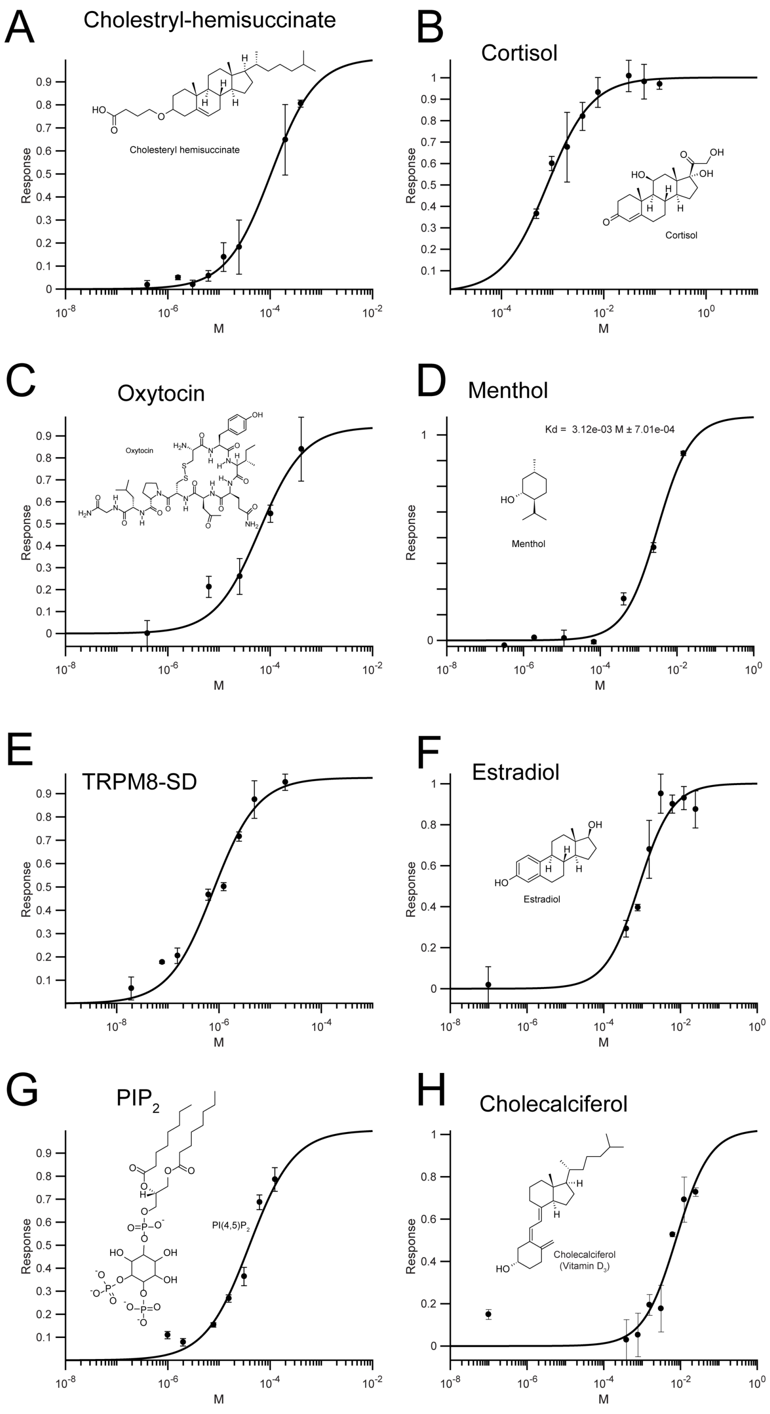

Figure S3.4 All MST binding curves. hPIRT MST binding curves for ligands that showed ligand dependent thermophoresis. A, B, F, and H are steroid ligands that possibly bind to the upper TM1 region that was identified as a cholesterol binding motif. Not shown, is the binding curve with CaM. Error bars signify the spread of data for each measurement.

CHAPTER 4

Experimentally Guided Structure Prediction of hPIRT With Rosetta

4.1 Introduction

Structural predictions using sparse experimental restraints have advanced in recent years. Well-structured membrane proteins comprising α-helical bundles have been determined with as few as one long range restraint and even showed modest predictions with only chemical shift guided restraints.[55] Additionally, electron paramagnetic resonance with double electron electron resonance (DEER) has been a useful tool for spare experimentally guided Rosetta calculations.[107, 108] Additionally, an NMR experiment similar to DEER called paramagnetic relaxation enhancement (PRE), has been combined with residual dipolar couplings (RDC) and chemical shifts to generate model mechanisms for cAMP (cyclic adenosine monophosphate) binding in HCN ion channels (HCN, Hyperpolarization-activated cyclic nucleotide-gated).[56] For hPIRT, NMR data from RDC, PRE, EPR, and chemical shift assignments were used with implicit membrane potentials in Rosetta to predict an experimentally guided hPIRT structure.

The hPIRT structure cannot be used with traditional restrained molecular dynamics due to a low amount of structural restraints per amino acid. With a full data and large number of structural restraints, NMR protein structure determination can be computed through simulated annealing molecular dynamics protocols like Xplor-NIH that start with single high energy extended chains that reduced structural energy by minimization to a local energy minima while satisfying experimental restraints and energy potentials.[109] Without a enough experimental restraints from PRE, nuclear Overhauser effect spectroscopy (NOESY), or RDC measurements from multiple alignments, the structure determination of hPIRT with Xplor-NIH is not likely to produce meaningful solutions.

The hPIRT structure can be predicted using Rosetta based applications and the sparse experimental restraints from NMR. Monte-Carlo sampling software, like Rosetta, use secondary structure predictions from amino acid sequences to guide random sampling of thousands of different predicted structures (called decoys, folds, or poses). These decoys are measured for overall fold quality based on scoring functions derived from physical and statistical terms.[57] Theses scores are weight to account for experimental constraints (Rosetta terms restraints as constraints), backbone conformations, and other physically modeled parameters.[57] When combined with NMR, Rosetta utilizes the secondary structure determination from NMR to generate decoys and has been shown to produce structures from chemical shifts only.[52, 110] The structure of hPIRT is not an ideal α-helical bundle and presents challenges for Rosetta.

The structural challenges with hPIRT structure consist of the amphipathic C-terminal α-helix and a long flexible N-terminal loop. Flexible loops in Rosetta are routinely trimmed out to sacrifice structural information for convergence within well order regions. The C-terminal amphipathic helix is a challenge for the implicit Rosetta membrane score functions since it is scored based on the membrane spanning regions, not including regions that only associate with the membrane, i.e. amphipathic α-helices.[60, 111] Measuring residual dipolar couplings (RDC) that report on the angular dependence of spin pairs with respect to the magnetic field can restrain the orientation of the hPIRT C-terminal amphipathic α-helix with additional long-distance measurements like PRE and EPR aiding the RDC measurements in restraining this region.

Resolution-adapted structural recombination (RASREC) was used to efficiently sample hPIRT structures. For de novo structure predictions, hundreds of thousands of conformations are sampled, which is a computationally demanding problem. RASREC is a highly parallelized code that utilizes parallelization strategies like message passing interface (MPI) to efficiently sample decoys with a master controller directing new decoy generation based on the probability of a unique incoming fold. Once the probability of a new fold is below the threshold set by the user, RASREC moves on to the next stage until the last fullatom stage is finished. The first three stages sample unique folds in centroid mode and the fourth stage takes all of the output from the first stages, remixes and resamples well scored regions within the individual folds. The last fullatom stage optimizes the structure until the energy is minimized to a user specified deviation in the backbone root means square. RASREC has been used to improve convergence of membrane proteins, [55] with NMR restrained Rosetta calculations,[53] and with structure predictions using evolutionarily conserved contact maps.[112] The success of this protocol has been shown with experimental restraints by filtering out violations, which is mostly attributed to its ability to resample well scoring segments from folds that did not score well overall.[52, 53, 55] Using the hPIRT NMR assignments with RASREC were used to generate experimentally guided α-helical templates that were used within the comparative modeling application to make a full length hPIRT structure.

The individual RASREC generated structures were used as templates for the Rosetta comparative modeling application that was used in Chapter 2. In this Chapter, hPIRT structural data from NMR and EPR as well as homology to the transmembrane regions of P2X4 were used to generate a predicted structure of hPIRT. The results suggest that

Rosetta can be used for challenging protein structures by dividing up structural elements, and recombining these with sparse restraints and comparative modeling strategies.

4.2 Materials and Methods

4.2.1 Fragment Generation from Chemical Shift Resonance Assignments

The chemical shift resonance assignments were used from the previously assigned spectra in Chapter 2. The Rosetta de novo structure prediction greatly makes use of backbone bond angle information that can generated by using secondary structure prediction algorithms like PsiPred or Jufo9d.[76, 77, 111] NMR data from chemical shifts were used to experimentally predict the secondary structure of hPIRT, from which 9mer and 3mer fragments for CS-Rosetta were generated using previously optimized protocols.[52] These fragments were used for structure predictions within the Rosetta software.

4.2.2 Residual Dipolar Coupling

The residual dipolar coupling measurements were carried out using two independent alignment media. In order to generate the alignment media we used a 3D printer to make a casting block and lined this with polytetrafluoroethylene (PTFE, Teflon) with an inner diameter of 6 mm. The gel mixtures for each alignment medium is listed in Table 4.1.

Table 4.1 Residual Dipolar Coupling Polyacrylamide Contents

CHEMICAL	**CONCENTRATION**	**EXAMPLE**
ACRYLAMIDE	40%	4 g Acrylamide + 6 g H_2O
BIS-ACRYLAMIDE	2%	2 g methylene-bis-acrylamide + 98 g H_2O
BUFFER	--	250 mM imidazole, pH = 6.5
APTMAC	40%	4 g APTMAC + 6 g H_2O
APS	10%	10 µL
TEMED	--	4 µL

APTMAC is (3-Acrylamidopropyl)trimethylammonium chloride, which copolymerizes with the methylene bis-acrylamide to confer a positively charged copolymer. TEMED is (3-Acrylamidopropyl)trimethylammonium, which stabilizes the free radical generated from ammonium persulfate (APS) for polymerization. For neutral gels, the APTMAC is omitted from the ingredients. The chemicals were mixed in a 15 mL conical vial and vortexed to ensure uniform mixing. Prior to initiating the reaction with TEMED, the solution was sterile filtered with a 0.22 μm filter (Millipore) to eliminate any polymerized acrylamide. The mixture was then pipetted in each well of the casting block with the bottom covered with paraffin film (Parafilm) and each well was covered in a droplet of isopropanol as air inhibits the polymerization. The polymerization was carried out overnight to ensure the reaction is complete.

After the polymerization, the gels slide out of the casting chamber onto PTFE covered Petri dish. These gels were cut to 1.7 cm resulting in a final stretched length of 4 cm in a 5 mm NMR tube. The charged and neutral gels were generated with 4.0% and 3.8% copolymer polyacrylamide, respectively. The gels were dialyzed in 4 L of water over two days to eliminate any unpolymerized chemicals and exchange to NMR buffer.

The purified hPIRT was then added to the cut gels in an Eppendorf tube and incubated at room temperature until the concentration of the excess protein is constant measured by OD_{280}. Once the maximum amount of protein was soaked into the gel, the gel was loaded into a 5 mm NMR tube with open ends, i.e. no bottom, using a syringe attached to Tygon tubing. Gentle suction was applied until the gel was fully inserted into the NMR tube.

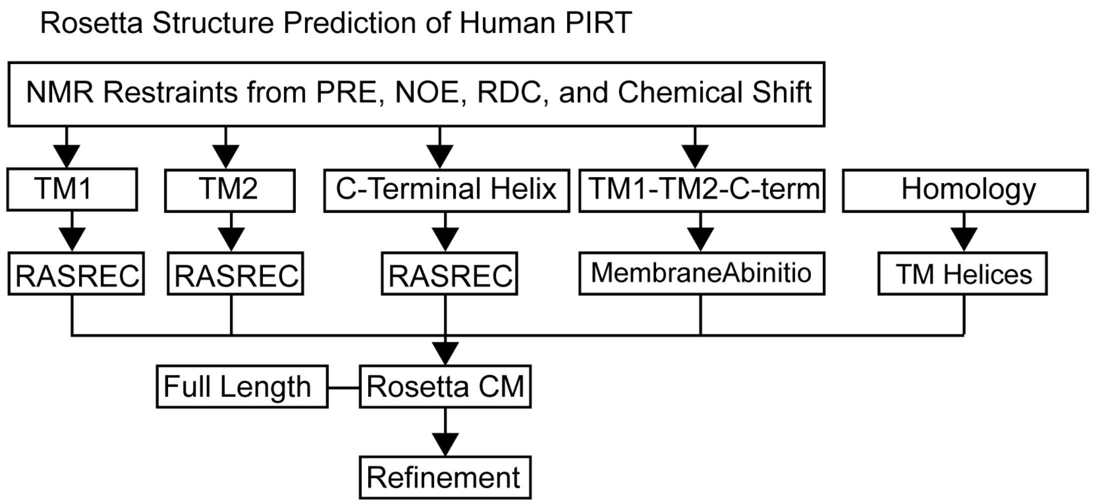

Figure 4.1 Flow chart for PIRT structure with Rosetta. Restraints from NMR were calculated are converted to Rosetta format. RASREC Rosetta was used to calculated structural decoys for the TM1, TM2, and C-terminal Helix structural domains. Separately, a de novo structure was calculated for amino acids comprising the TM1 through the C-terminus using membrane ab initio. These models as well as sparse homology models, long range distance restraints, and RDC restraints were used as inputs for comparative modeling strategies to generate a final PIRT model.

Measuring the RDC's of a membrane protein presents challenges with increased rotational correlation times causing broadened line widths and loss of signal. Therefore, we used a pulse program called ARTSY, discussed thoroughly in Chapter 1.2.5.

Singular value deconvolution was calculated on the two alignment media to estimate the independence of the alignment media for Rosetta calculations.[54] Residual dipolar coupling values were then to a sinusoidal MATLAB script to analyze the periodicity of the α-helices and assess their dipolar wave character.[113]

4.2.3 Paramagnetic Relaxation Enhancement

Site directed mutagenesis was used with Q5 cloning (New England Biolabs, Inc) to generate a cysteine free hPIRT mutant, which was sequence verified with Sanger sequencing at ASU Core Genomics Facility. Once the Cys free hPIRT was made, subsequent Q5 cloning was used to generate single Cys mutants by mutating residues at specific locations: H120C, C106, S124C, S60C, S132C, and S85C.

The mutants were expressed and purified the same as the wild type hPIRT into HEPES pH 7.5 and 0.5% DPC. The purified hPIRT mutants were incubated for 12 hours with 2 mM freshly dissolved DTT (dithiothreitol) to reduce the sulfhydryl side chains of the Cys. After DTT incubation, 10 mM of MTSL (*S*-(1-oxyl-2,2,5,5-tetramethyl-2,5-dihydro-1H-pyrrol-3-yl)methyl methanesulfonothioate) was incubated with the hPIRT mutant for 3 hours at 37 ºC and then overnight at room temperature to attach a paramagnetic nitroxide spin label. After the overnight incubation, the sample was spun down in an Eppendorf tube to eliminate aggregated MTSL or hPIRT, where the supernatant was then loaded onto a pre-equilibrated Ni-NTA column to change buffer conditions to NMR buffer and to eliminate the free/unreacted MTSL.

The labeled protein was measured with proton relaxation experiments consisting of a symmetric delay around the final ^{1}H 180º pulse of 0 ms, 2 ms, 6 ms, and 12 ms times, where each time delay applied corresponds to a separate HSQC. These delay times correspond to ½ of the total delay time, as such the intensities of the amino acid resonances were plot as a function of 0 ms, 4 ms, 12 ms, and 24 ms respectively. After a set of 4 HSQC spectra were acquired with the specified delay times, the labeled sample was reduced with and incubation of one hour with 10 mM ascorbic acid. Then the same experiments were repeated to make PRE match spectra (Figure 4.4).

The data were analyzed in CCPN by extracting resonance intensities and fitting them according to a monoexponential decay. The difference between the relaxation rates correspond to R_2^{eff} for the measured relaxation rate from the oxidized nitroxide spin label and R_2 for the measured relaxation rate from the reduced sample. The R_2^{eff} is the sum of the R_2 and the relaxation rate contribution from the free electron (Γ_2) according to:

$$R_2^{eff} = \Gamma_2 + R_2$$

The distance dependence of a nucleus and an unpaired electron is given by:

$$\Gamma_2 = \frac{1}{15}\left(\frac{\mu_0}{4\pi}\right)^2 \gamma_I^2 g^2 \mu_B^2 \, S(S+1) r^{-6} \left(4\tau_c + \frac{3\tau_c}{1+(\tau_c\omega_H)^2}\right)$$

where *r* is the distance between the free electron spin and the observed nucleus, μ_0 is the vacuum permeability constant, μ_B electron Bohr magneton, τ_c is the PRE correlation time given by $\tau_c^{-1} = \tau_r^{-1} + \tau_s^{-1}$; τ_r is the rotational correlation time, τ_s is the electron relaxation time; ω_H is the nuclear Larmor frequency, γ is the gyromagnetic ratio, and S is the spin quantum number. From this equation, we can derive distances from the MTSL nitroxide spin and the amino acids in the protein.

4.2.4 Electron Paramagnetic Resonance

The electron paramagnetic resonance (EPR) samples are prepared generally in the same way as the PRE samples, the difference here is that double Cys mutants are used instead of single Cys hPIRT for double electron electron resonance (DEER) experiments. DEER was carried out by a collaborator at the Miami University in Ohio. The distance dependence from the paramagnetic centers EPR data can be integrated into Rosetta structure determination with a knowledge-based potential [107, 114] that takes into account the rotamer angles of the spin label as well as the distance from C_β to the spin center.

4.2.5 Nuclear Overhauser Effect Spectroscopy (NOESY) Distance Restraints

Few nuclear Overhauser effect (NOE) distance restraints could be measured on hPIRT, which was due to unfavorable relaxation leading to decreases in all signals including from cross polarization for NOE measurements. Only two long range NOE's were observed, that were assigned for an intramolecular contact between the two α-helices at Gly63 of TM1 and Gly100 of TM2 (Figure 4.3). Cross peak assignments were carried out using [^{1}H-^{15}N]-TROSY-NOSEY-TROSY with mixing time of 90 ms and a [^{1}H-^{15}N]-TROSY-TOCSY (TOCSY, total correlation spectroscopy) with mixing time of 60 ms. From these experiments, $^1H_\delta$ of tryptophan can easily be assigned at a chemical shift resonance position of ca. 7 ppm. Using the distance from the from tryptophan $^1H_\delta$ to $^1H_\varepsilon$ of 2.6 Å and the volume of the cross peak for this resonance as a reference, the distances for other cross peaks can be measured using:

$$r = r_{ref}\left(\frac{I_{ref}}{I}\right)$$

where the r_{ref} is the reference distance and the I_{ref} is the volume for the resonance interatomic cross peak. Resonance volume the integral of the spectrum intensity around a selected peak. The distance r from other interatomic cross peaks can then be measured using their corresponding resonance volumes.

4.2.6 Hydrogen Bonding Determination from NMR Temperature Coefficients

TROSY-HSQC were measured on hPIRT at temperatures 30 to 50 °C in 2.5 °C increments. The change in resonance position for the ^{1}HN were calculated as a $\Delta_{HN} = \left(\delta_{HN,30} - \delta_{HN,i}\right)^2$ where i corresponds to the chemical shift at temperature i in the range 30 to 50 °C in 2.5 °C increments. Fitting the Δ_{HN} to a straight line, the slope of > -4.6 ppb can be used to estimate hydrogen bonded amides.[37] The hydrogen bonded residues were given a constraint from the donor HN to the acceptor C′ of the i+4 amino acid assuming a standard α-helix with a distance of 2.0 Å and a standard deviation of 0.5 Å, representing the average distance of a hydrogen bond.[115]

4.2.7 Incorporation of Experimental Restraints in Rosetta

To use constraints in Rosetta, the function that has been optimized for NOE and PRE based distances is a BOUNDED function. This has the form of a bounded quadratic equation:

$$f(x) = \begin{cases} \dfrac{(x-lb)^2}{sd}, & x < lb \\ 0, & lb \le x \le ub \\ \dfrac{(x-ub)^2}{sd}, & ub < x \le ub + rswitch \times sd \\ \dfrac{1}{sd}\big(x - \big(ub + (rswich \times sd)\big) + (rswitch \times sd)\big)^2, & x > ub + rswitch \times sd \end{cases}$$

where rswitch = 0.5, *sd* is the standard deviation, and *lb* and *ub* are the lower and upper bound, respectively.[108, 110] This function has a shape of an exponential weight as the distance approaches the lower bound and a linear penalty as upper bound is reached (Figure S4.1).

The RDC data was converted to Rosetta readable constraints by making a table of two columns with the first column as the residue number and the second column as the RDC in Hz (supplementary section).

4.2.8 Experimentally Guided Structure Prediction of hPIRT with Rosetta

Rosetta comparative modeling strategies were utilized to incorporate models from separate Rosetta calculations to build a model of hPIRT. First, separate RASREC

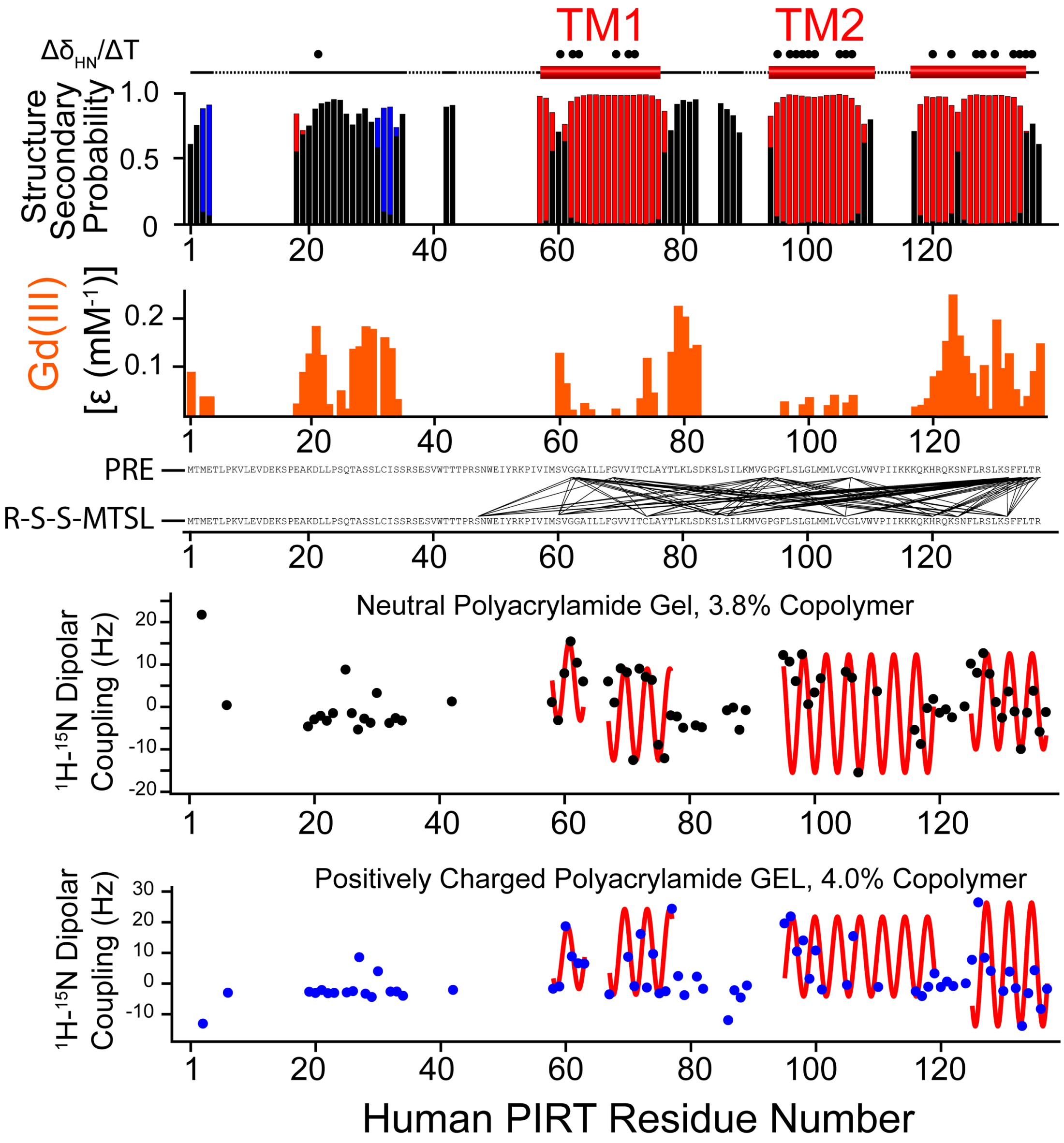

Figure 4.2 The experimental NMR data from hPIRT. From top to bottom, experimentally determined hydrogen bond networks from HN donor and C′ acceptors for helices were measured using temperature gradients from proton chemical shift perturbation. Chemical shift derived secondary structure prediction was used to generate fragments for Rosetta. Solvent accessibility with solvent PRE’s were used for hydrophobicity files. PRE measurements from conjugated spin label MTSL were measured with proton relaxation experiments to several single Cys mutants. RDC restraints, shown here with dipolar wave analysis, in two alignment media were used converted to Rosetta readable files. These were all used in Rosetta structure predictions.

calculations for individual transmembrane α-helices and the C-terminal α-helices were calculated. Then a structural prediction using the membrane ab initio application for residues 54-137 comprising the TM1 through C-terminus was calculated. RASREC calculations using the implicit membrane environment, uses large amounts of random access memory that increases through each stage resulting in calculation crashes and is not practical on anything smaller than 30 amino acids at a time or computer other than a compute cluster with access to large amounts of RAM, e.g. 6 Gigabytes or more per CPU thread. The final models from each of these Rosetta calculations as well as the transmembrane regions of a structurally homologous P2X4 channel were used as templates for the Rosetta comparative modeling application. 30,000 decoys from RosettaCM were calculated and clustered using the protocol shown in Figure 4.1 for flow chart.

4.3 Results

4.3.1 Experimental Structural Restraints Measured Using NMR

Distance restraints were obtained for hPIRT using NOE, EPR, and PRE. The small number of NOEs prevent the calculation of traditional NMR structure determination from Xplor-NIH calculations, but a key interdomain distance from TM1 to TM2 could be determined (Figure4.3). 25 NOE restraints in total were assigned and used in Rosetta with using a BOUNDED constraint function, Figure S4.1. EPR distance for a single double Cys mutant of hPIRT was measured from C74 to H120C with a distance of 50 ± 0.5 Å. Additionally, PRE measurements for several single Cys mutants conjugated to a nitroxide spin label was used to determine long range restraints (Figure 4.4). Resonances

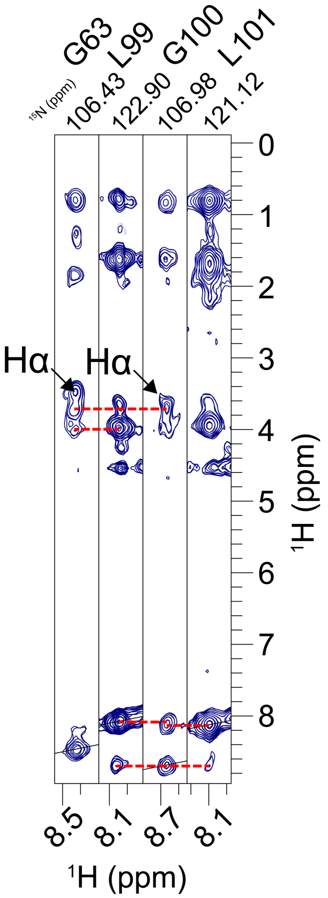

Figure 4.3 NOESY strip plot of hPIRT. The interatomic distance between the hPIRT TM1 and TM2 was measured with NOE cross peaks from Hα Gly63 to HN Gly100 and vice versa, shown here with a red dotted arrow. This strip panel shows cross peaks for Gly100 HN can be detected at HN resonance positions for Leu99 and Leu101 as well. Distances were measured using the Gly63 and Gly100 cross peak resonance volumes and converting them to interatomic distances using the known distance between a tryptophan indole amine to $^1H_\delta$ and its cross peak resonance volume (see methods).

that were clearly resolved and assigned to amino acid residues were used to measure the difference between the oxidized (Figure4.4A, black spectrum) and reduced state (Figure 4.4A, red spectrum) of the nitroxide spin label. Figure 4.4B shows a representative resonance for Arg137 showing differences in relaxation rates caused by the nitroxide free electron. These restraints were converted to Rosetta constraints using a BOUNDED function.

4.3.1 Calculation of individual hPIRT α-Helices Using Rosetta RASREC

Rosetta calculations using RASREC protocols was carried out on hPIRT for the structured elements TM1, TM2, and the C-terminal α-helix identified in previous NMR

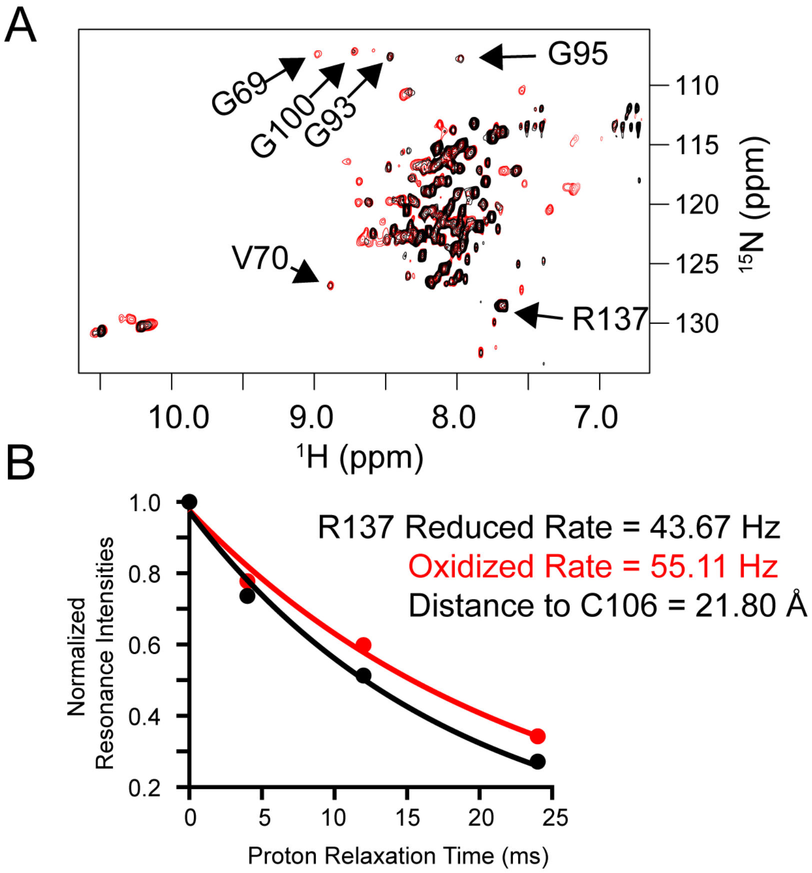

Figure 4.4 Paramagnetic relaxation enhancement derived distance measurements. A) The black spectrum represents an oxidized nitroxide spin label that possesses paramagnetic properties that enhance the relaxation rates of spins in proximity. Show with arrows are resonances that were easily assigned that show differences in resonance intensity between oxidized and reduced (black) spectra. See methods for proton relaxation. B) The proton relaxation rates are fit to monoexponetial functions with relaxation rates converted to distances. Shown in B) is the rates for Arg137 to the nitroxide spin labeled Cys106. For this figure, the intensities were normalized to the max for comparison between oxidized and reduced. No normalization was carried out for distances used in structure calculations.

structure analyses in Chapter 2. The individual RASREC structure calculations were calculated by using fragments and RDC values only. A membrane scoring function (Supplemental 4.5.5) was used to enforce an implicit membrane[60, 111] for each membrane associated α-helical region. The C-terminal α-helix was generated in the same manner; however, since there are no transmembrane regions the implicit membrane was left out since adding the membrane scoring function caused the run to fail immediately.

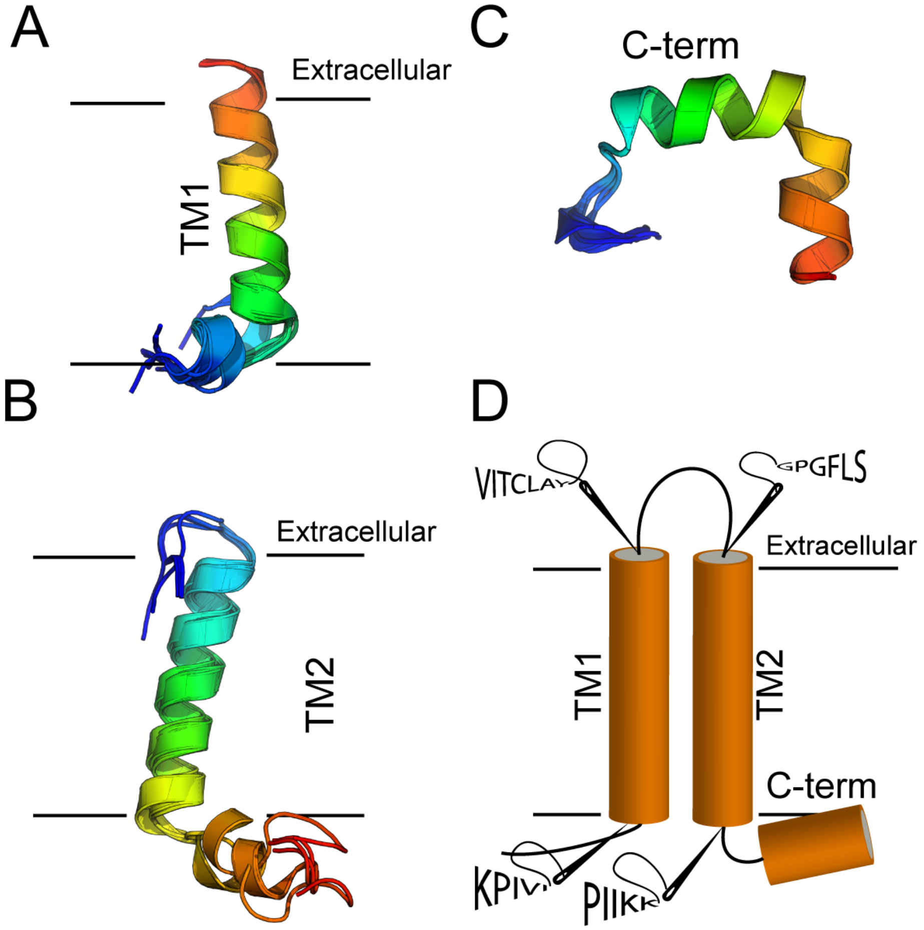

Figure 4.5 The structure predictions from individual rounds of RASREC. A-C) The top 10 from 500 lowest scoring fullatom decoys were selected as representative models for TM1, TM2, and the C-terminus. The TM2 show the most divergence but it generally shows the correct topology that will be used in further structure calculations. D) The cartoon needles are to signify that these structural models will be stitched together by the adjoining loops during the RosettaCM stage.

These calculations converged using Rosetta's automated RASREC protocols and produced the predicted structural components that would be used for further calculations (Figure 4.5, A-C). These decoys were stitched together in later applications using RosettaCM (Figure 4.5, D).

4.3.2 Rosetta Membrane Ab Initio calculations

To make a template of hPIRT that spanned the TM helices to the C-terminus, NMR derived fragments, RDC values, EPR, and spare NOE's were used with implicit membrane scoring applied to the membrane ab initio application, which generated 30,000

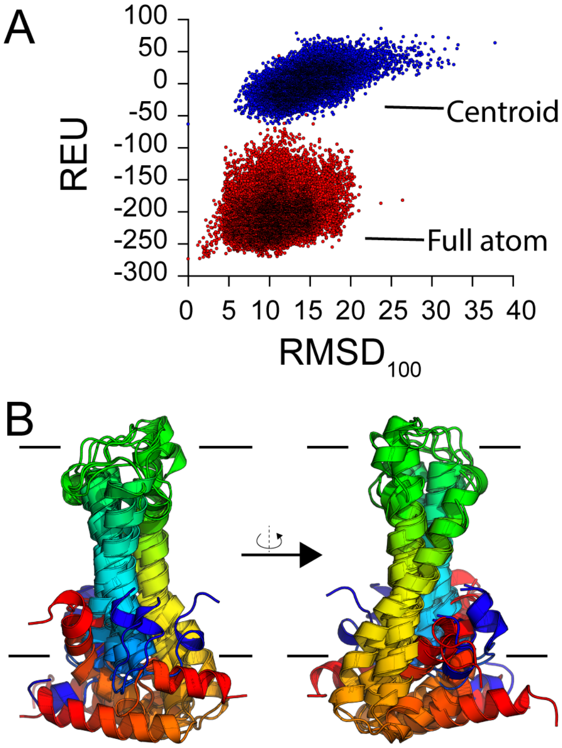

Figure 4.6 The hPIRT membrane ab initio structure predictions. A) The centroid models were calculated showing apparent energy funnel (blue). The best scoring decoys were seeded into full atom refinement (red). B) The top scoring 10 from 30,000 are shown as representative of this stage colored in rainbow from blue to red, N-term starting at residue 54 to the C-term, respectively. It is apparent that the structure did not converge on a single structure and these will be used in the RosettaCM stage as templates.

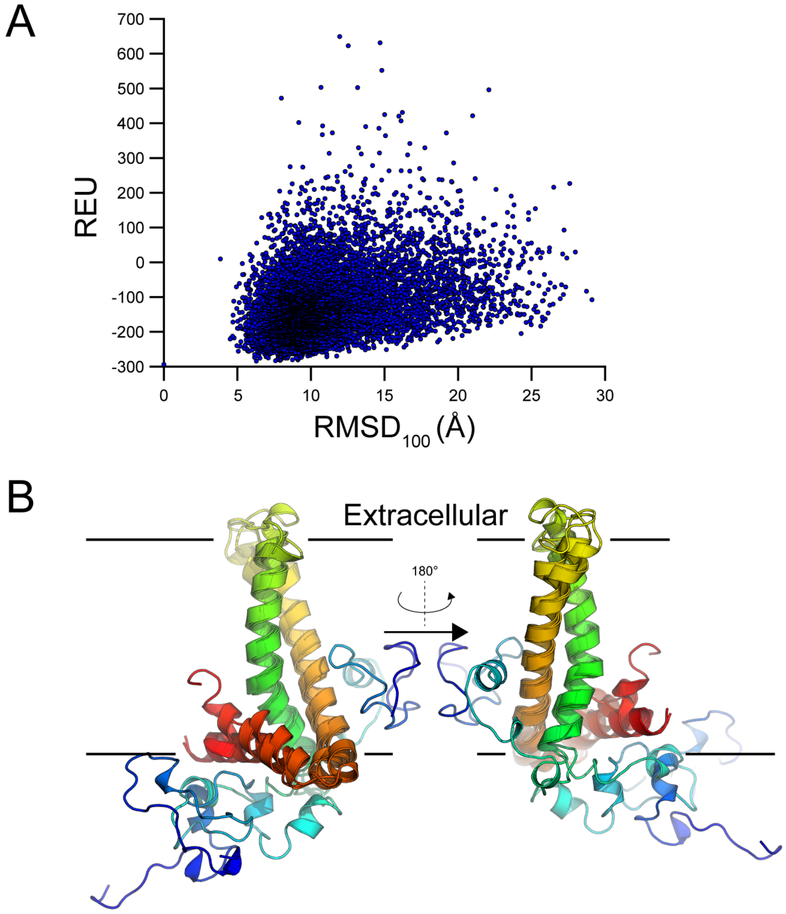

Figure 4.7 Using RosettaCM to combine separate Rosetta predictions. A) The Rosetta prediction of PIRT appears to have succeeded with converging energy function. B) The top 3 lowest scoring decoys from the largest clusters from appears to restrain the C-terminal helix as an amphipath and fold hPIRT into a plausible membrane orientation.

centroid models (Figure 4.6A). The top scoring 100 decoys from these were used as input for refinement with relax to generate 30,000 full atom decoys (Figure 4.6B). This strategy resulted in an apparent energy funnel suggestive of consensus structure calculation.

4.3.3 Rosetta Comparative Modeling

To combine the outputs from successful individual RASREC calculations and an apparent convergence from membrane ab initio, the Rosetta comparative modeling

(RosettaCM) protocols were used that has had success in combining multiple templates from structurally homologous structures.[50] RosettaCM was designed originally for homology modeling but it can be used to resample structures from separate calculations as templates.[116] Homologous structures of hPIRT based on sequence were exhaustively investigated, resulting in one structure from a membrane protein trimer ion channel, P2X4, that shares low sequence identity with hPIRT but potentially high

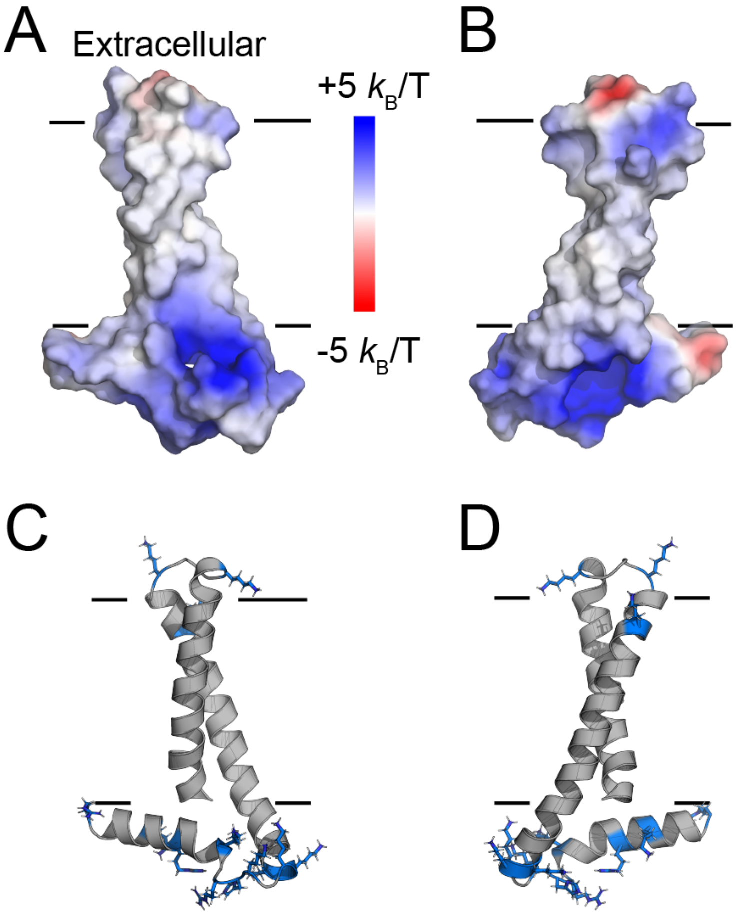

Figure 4.8 PIRT Structure electrostatic map. Examination of hPIRT structure prediction shows two large intracellular positively charge regions. For visualization purposes, the N-terminal (residues 1-54) was hidden. In A and B, Adaptive Poisson-Boltzmann electrostatic mapping shows that there are two positively charge pockets that are located on the intracellular side of the lipid bilayer. In C and D, the electrostatic charges are made of the Lys, Arg, and His show here with blue sticks. These areas provide a mechanism for binding PIP_2 in vivo.

transmembrane structural homology. The representative from the largest clusters from each RASREC (Figure 4.5 A-C) and membrane ab initio (Figure 4.6 B) as well as the homologous structure was used as templates for RosettaCM. 30,000 decoys were calculated showing an apparent energy funnel Figure 4.7A suggestive of convergence. The results from this suggest that RosettaCM can be used for de novo membrane protein structure prediction Figure 4.7B.

4.4 Discussion

Homology modeling using RosettaCM has been used with high success to produce models with electron density restraints and with membrane proteins. In Chapter 2, it was used to produce a C4 symmetric membrane protein ion channel guided by electron density from a homologous protein. With our data in this study we show that RosettaCM can be used with sparse experimental NMR restraints to generate structural models from templates that come from separate Rosetta calculations. A similar protocol has been recently shown with success to generate highly converged structural models on challenging systems.[117] The success of RosettaCM over its predecessor or the original Rosetta comparative modelling, is the ability to include structural information from multiple templates and insert portions of them randomly while also randomly inserting fragment information.[50] This has the benefit of narrowing the sample space to well-ordered structures, which is a boon to structure prediction.

The protocol used here to predict the hPIRT structure took advantage of sparse NMR derived restraints and Rosetta computation applications, resulting in a structural model comprising two transmembrane α-helices and one amphipathic α-helix with an unstructured N-terminal tail. Using adaptive Poisson-Boltzmann electrostatic calculations with PyMol,[118] the hPIRT structure shows two positively charged pockets that could be responsible for PIP_2 interactions (Figure 4.9A-B). These regions do seem to form a pocket that could be amenable to bind of the lipid (Figure 4.9C-D) that reside at the interface of the inner leaflet bilayer. In the context of TRPM8 and PIP_2 binding, this polybasic region appears to explain how the competition may work (Figure 4.9 A-B). The amino acids that bind to TRPM8 and PIP_2 appear on the C-terminal α-helix in two

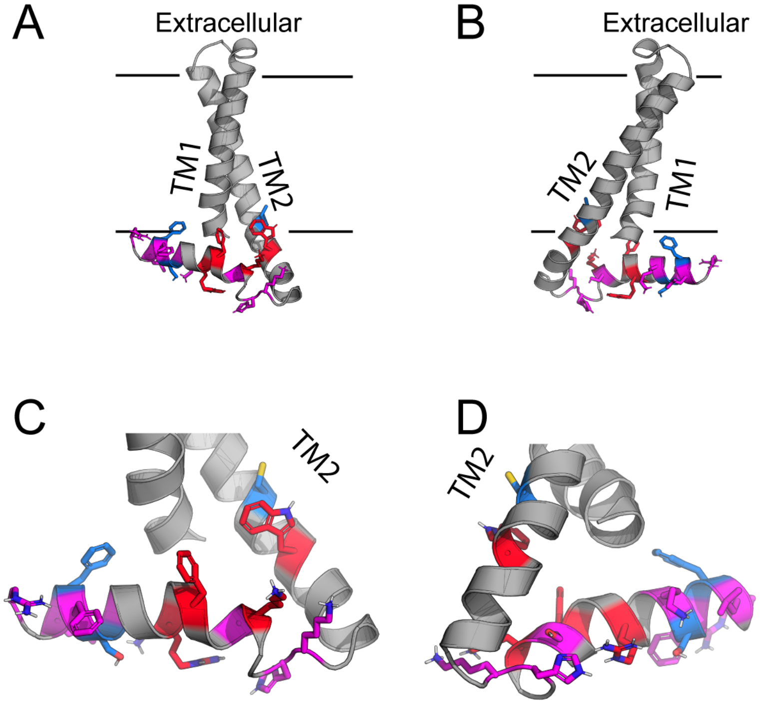

Figure 4.9 Mapping hPIRT binding sites. The binding sites identified in Chapter 2 were mapped on the hPIRT structural model. In A and B, the TM helices are labeled to show the orientations for C and D in the membrane. In C and D, red colored residues represent amino acids binding to PIP_2, blue are binding to hTRPM8-SD, and magenta are binding to both.

positions (Figure 4.9 C-D, magenta). One position is close to the lower portion of the TM2 and the other at the C-terminus. This helix is potentially long enough to interact with R1008 in the TRPM8 TRP domain and can help explain how PIP_2 can interact with this amino acid as well as the region closer to the pore domain. It is possible that PIP_2 is transferred by hPIRT to R1008 to stabilize the open state of the channel as has been shown with KCNQ2 channels.[25] From the calmodulin binding data discussed in Chapter 3, this region is in an opportune region to enhance apo-CaM sequestering of Ca^{2+} and the resulting dissociation from hPIRT can allow hPIRT to bind PIP_2 to shuttle it to R1008.

The ability of this software to generate models of challenging systems using sparse experimental restraints is an exciting extension for structural biology. For example, with a hPIRT structure we can now probe what the complex of hPIRT with a host of other proteins and ligands that can be used to help explain how hPIRT influences ion channel physiology.

4.5 Supplemental Information

4.5.1 MATLAB Codes

--- Modeled BOUNDED Constraint ---

This script is designed to simulate a BOUNDED distance restraint in Rosetta of an upper bound of 25 and lower bound of 18 with a standard deviation of 0.5.

```
rng default
clear
clc
% close all

simulate_xData=linspace(0,35,1000);
lb = 18; % lower bound
ub = 25; % upper bound
sd = 0.5;
rswitch = 0.5; %default
```

```
simulate_yData=zeros(size(simulate_xData));
xy=(simulate_xData < lb  == 1);
x=simulate_xData(xy);

simulate_yData(xy)= power((x-lb)/sd,2);

xy=((lb <= simulate_xData & simulate_xData <= ub)  == 1);
x=simulate_xData(xy);

simulate_yData(xy) = 0;

xy=((ub < simulate_xData & simulate_xData <= (ub+rswitch*sd))  == 1);
x=simulate_xData(xy);

simulate_yData(xy)= power((x-ub)/sd,2);

xy=(simulate_xData > (ub+rswitch*sd))  == 1;
x=simulate_xData(xy);

simulate_yData(xy)=(1/sd).*(x-(ub+rswitch*sd))+power((rswitch*sd)/sd,2);
```

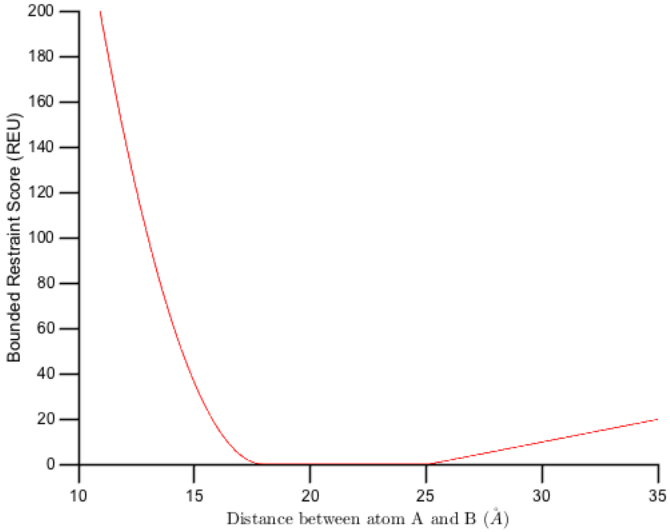

Figure S4.1 The Rosetta constraint BOUNDED model. This model was generated using MATLAB with a lower bound and upper bound of 18 Å and 25 Å respectively, and a standard deviation (SD) of 0.5 Å. The SD will affect the depth of the curve rather than the upper or lower bounds.

---Dihedral Wave Analysis---

```
%***********************************************************************
```

```
%##########
% Make sure you have the file widonwLoop.m and sigfw.m in the path when
% running this.
% This script was modified by Nick Sisco in 2014 to include a periodicity fitting function that can be
appended with period_analysis_v3.m function
%Dipolar Waves as NMR Maps of Protein Structure
%Michael F.Mesleh,Ü Gianluigi Veglia,á Tara M. DeSilva,ß Francesca M. Marassi,| and
%Stanley J. Opella*,Ü
% JACS Comm, 2001

close all
clear all
format compact

global rn
global rdcnh
global rnw
global rdcnhw

%  READ THE INPUT DATA: rn AND rdcnh ARE THE PAIRS THAT ARE FIT
%  ALTERNATIVE READ STATEMENTS FOR DIFFERENT TYPES OF INPUTS
% load('Book2.txt')
Book2=load('initial_Dnh_measurements.txt')
% Book2=load('positive_chargedBook.txt')
rn=Book2(:,1)
rdcnh=Book2(:,2)
N=size(rdcnh);

%  DEFINE THE SIZE OF THE SLIDING WINDOW TO BE USED for the scoring function
wsize=5;wsize=wsize-1;

%  THIS IS THE LOOP OVER ALL OF THE POSSIBLE POSITIONS OF THE WINDOW,
%    INDEXED BY THE COUNTER i.

%*******************************************************************
%*********LOOP TO FIT A SINUSOID TO EACH WINDOW OF THE DATA*************
%*******************************************************************

for i=min(rn):max(rn)-wsize;

%*******************************************************************
%  HERE I MAKE SURE THAT THE WINDOW SIZE IS SET TO THE RIGHT NUMBER OF
%    MEASURED VALUES.
  wmax=i+wsize;
  wcount=0;
  for jcount=1:N(1)
    if rn(jcount) >=i & rn(jcount) <= wmax
      wcount=wcount+1;
    end
  end
rnw=zeros(wcount,1);rdcnhw=zeros(wcount,1);
count=1;
%*******************************************************************
%  HERE I MAKE THE VECTORS rnw, rdcnhw BETWEEN i AND i+wmax BY SORTING
```

```
  for j=1:N(1)
   if rn(j) >= i & rn(j) <= wmax
     rnw(count)=rn(j);rdcnhw(count)=rdcnh(j);count=count+1;
   end
  end

% WITH THIS WINDOW MAKE THE BEST FITTING SINUSOID
   M=size(rnw);Amax=max(rdcnhw);Amin=min(rdcnhw);
   start(1)=0;
   off=0;
   if M(1) > 1
     [x0,y0]=fminsearch('sigfw', start);
     phi=x0(1);
     rn0=linspace(min(rnw), max(rnw), 10*M(1));
     L0=(Amax+Amin)/2+(Amax-Amin)/2*sin(2*pi*rn0/3.6+phi+off);
     diff=(rdcnhw-((Amax+Amin)/2+(Amax-Amin)/2*sin(2*pi*rnw/3.6+phi+off))).^2;
     bphase(i)=phi*(180/pi);
     score(i)=sum(diff)/M(1);
     position(i)=i+(wsize/2);
   end
% FOR MISSING RESIDUES A WINDOW WITH ONE MEASUREMENT OR LESS IS NOT USED
   if M(1) <= 1
     position(i)=i+(wsize/2);diff=1000;score(i)=20;bphase(i)=500;
   end
  i
end

%*****************************************************************
%*****************************************************************
%*****************************************************************

% NOW THAT THE SCORING IS DONE, THE PROGRAM GOES THROUGH AND OVERLAYS
%   THE BEST FITTING SINUSOIDS ON THE EXPERIMENTAL DATA.
disp('                                                        ')
disp('(This program can only handle up to 5 helices, but can be modified to include more)')
disp('(Just put in the number zero if you are not sure yet)          ')
disp('                                                        ')
num=input('Enter the number of sinusoids you want to fit');

%*****************************************************************
%**********NOW I FIT AND SCORE THE HELICAL REGIONS SEPARATELY***********
%*****************************************************************
figure(1)
for k=1:num;
   %*************************************************************
   % DEFINE THE LIMITING VALUES OF THE HELIX IN QUESTION
   disp('Helix Number ');
   k
   hn(k)=input('Enter the number of the first residue of this helix:   ');
   hc(k)=input('Enter the number of the last residue of this helix:   ');
   %*****************************************************************
   % HERE I MAKE SURE THAT THE WINDOW SIZE IS SET TO THE RIGHT NUMBER OF
   %   MEASURED VALUES.
   wfit=0;
```

```
  for jfit=1:N(1)
   if rn(jfit) >= hn(k) & rn(jfit) <= hc(k)
    wfit=wfit+1;
   end
  end
  rnw=zeros(wfit,1);rdcnhw=zeros(wfit,1);
  %*************************************************************************
  count=1;
  for m=1:N(1);
   if rn(m) >= hn(k) & rn(m) <= hc(k)
    rnw(count)=rn(m);rdcnhw(count)=rdcnh(m);count=count+1;
   end
  end
  % PERFORM THE FIT
  start=0;Amax=max(rdcnhw);Amin=min(rdcnhw);
  [x0,y0]=fminsearch('sigfw', start);
  phi=x0(1);
  if k == 1
   rn1=linspace(min(rnw), max(rnw), 10*N(1));
   L1=(Amax+Amin)/2+(Amax-Amin)/2*sin(2*pi*rn1/3.6+phi);
  end
  if k == 2
   rn2=linspace(min(rnw), max(rnw), 10*N(1));
   L2=(Amax+Amin)/2+(Amax-Amin)/2*sin(2*pi*rn2/3.6+phi);
  end
  if k == 3
   rn3=linspace(min(rnw), max(rnw), 10*N(1));
   L3=(Amax+Amin)/2+(Amax-Amin)/2*sin(2*pi*rn3/3.6+phi);
  end
  if k == 4
   rn4=linspace(min(rnw), max(rnw), 10*N(1));
   L4=(Amax+Amin)/2+(Amax-Amin)/2*sin(2*pi*rn4/3.6+phi);
  end
  if k == 5
   rn5=linspace(min(rnw), max(rnw), 10*N(1));
   L5=(Amax+Amin)/2+(Amax-Amin)/2*sin(2*pi*rn5/3.6+phi);
  end
  diff=(rdcnhw-((Amax+Amin)/2+(Amax-Amin)/2*sin(2*pi*rnw/3.6+phi))).^2;
  rmserror=sqrt(sum(diff)/count)
end

%************************************************************************
%************************************************************************
%************************************************************************

% PLOT THE SCORE AS A FUNCTION OF POSITION IN THE SEQUENCE
clf
subplot(3,1,1)
if num == 0
 plot(rn,rdcnh,'-o')
else
plot(rn, rdcnh, 'o')
end
if num >=1
 hold on;plot(rn1, L1, 'm')
```

```
end
if num >=2
  hold on;plot(rn2, L2, 'm')
end
if num >=3
  hold on;plot(rn3, L3, 'm')
end
if num >=4
  hold on;plot(rn4, L4, 'm')
end
if num >=5
  hold on;plot(rn5, L5, 'm')
end
title('DIPOLAR WAVE ANALYSIS OF EXPERIMENTAL DATA')
ylabel('Experimental Data')
axis([min(rn)-5 max(rn)+5 min(rdcnh)-5 max(rdcnh)+5])
subplot(3,1,2)
plot(position,score, '-')
ylabel('Periodicity Score')
axis([min(rn)-5 max(rn)+5 0 max(score)+5])
subplot(3,1,3)
plot(position,bphase, '-')
ylabel('Phase of Sinusoid')
xlabel('Residue Number')
axis([min(rn)-5 max(rn)+5 -200 200])
%%
figure(2)
plot(rn,rdcnh,'bo')
if num >=1
  hold on;plot(rn1, L1, 'r')
end
if num >=2
  hold on;plot(rn2, L2, 'r')
end
if num >=3
  hold on;plot(rn3, L3, 'r')
end
if num >=4
  hold on;plot(rn4, L4, 'r')
end
if num >=5
  hold on;plot(rn5, L5, 'r')
end
% plot(position,score, '-')
title('DIPOLAR WAVE ANALYSIS OF EXPERIMENTAL DATA')
ylabel('Experimental Data')
xlabel('Residue Number')
axis([min(rn)-5 max(rn)+5 min(rdcnh)-5 max(rdcnh)+5])
set(gca,'FontName','Arial','TickDir','out','TickLength',[0.03
0],'LineWidth',1.5,'FontSize',12,'Color','none','XColor',[0 0 0],'YColor',[0 0 0]);
```

--- Dipolar Wave with Periodicity Fitting ---

```
clear
```

```
close all
global rn
global rdcnh
global rnw
global rdcnhw

N=size(rdcnh);
wsize=5;wsize=wsize-1;
windowLoop(wsize);

Book2=load('Book2.txt')
% Book2=load('KCNE3_RDC_20140509.txt')
rn=Book2(:,1)
rdcnh=Book2(:,2)
N=size(rdcnh);

%  DEFINE THE SIZE OF THE SLIDING WINDOW TO BE USED for the scoring function
wsize=5;
wsize=wsize-1;

%  THIS IS THE LOOP OVER ALL OF THE POSSIBLE POSITIONS OF THE WINDOW,
%    INDEXED BY THE COUNTER i.

%**********************************************************************
%*********LOOP TO FIT A SINUSOID TO EACH WINDOW OF THE DATA*************
%**********************************************************************

%%

for i=min(rn):max(rn)-wsize;

%**********************************************************************
%  HERE I MAKE SURE THAT THE WINDOW SIZE IS SET TO THE RIGHT NUMBER OF
%    MEASURED VALUES.
  wmax=i+wsize;
  wcount=0;
  for jcount=1:N(1)
    if rn(jcount) >=i & rn(jcount) <= wmax
      wcount=wcount+1;
    end
  end
rnw=zeros(wcount,1);
rdcnhw=zeros(wcount,1);
%**********************************************************************
%  HERE I MAKE THE VECTORS rnw, rdcnhw BETWEEN i AND i+wmax BY SORTING
count=1;
  for j=1:N(1)
    if rn(j) >= i & rn(j) <= wmax
      rnw(count)=rn(j);
      rdcnhw(count)=rdcnh(j);
      count=count+1;
    end
  end

%  WITH THIS WINDOW MAKE THE BEST FITTING SINUSOID
```

```
  M=size(rnw);
  Amax=max(rdcnhw);
  Amin=min(rdcnhw);
  start(1)=0;
  off=0;
  if M(1) > 1
   [x0,y0]=lsqnonlin('sigfw', start);
   phi=x0(1);
%      per=3.6;
  [per,y0]=period_analysis_v2(rnw,rdcnhw);
   rn0=linspace(min(rnw), max(rnw), 10*M(1));
   L0=(Amax+Amin)/2+(Amax-Amin)/2*sin(2*pi*rn0/per+phi+off);
   diff=(rdcnhw-((Amax+Amin)/2+(Amax-Amin)/2*sin(2*pi*rnw/per+phi+off))).^2;   %
   bphase(i)=phi*(180/pi);
   score(i)=sum(diff)/M(1);
   position(i)=i+(wsize/2);
  end
%  FOR MISSING RESIDUES A WINDOW WITH ONE MEASUREMENT OR LESS IS NOT USED
  if M(1) <= 1
   position(i)=i+(wsize/2);diff=1000;score(i)=20;bphase(i)=500;
  end
 i  ;
end

%%

disp('                                                    ')
disp('(This program can only handle up to 5 helices)'                )
disp('(Just put in the number zero if you are not sure yet)          ')
disp('                                                    ')
num=input('Enter the number of sinusoids you want to fit          :  ');

for k=1:num;
  %***************************************************************
  %  DEFINE THE LIMITING VALUES OF THE HELIX IN QUESTION
  disp('Helix Number ');
  k
  hn(k)=input('Enter the number of the first residue of this helix:   ');
  hc(k)=input('Enter the number of the last residue of this helix:    ');
  %*******************************************************************
  %  HERE I MAKE SURE THAT THE WINDOW SIZE IS SET TO THE RIGHT NUMBER OF
  %    MEASURED VALUES.
  wfit=0;
  for jfit=1:N(1)
   if rn(jfit) >= hn(k) & rn(jfit) <= hc(k);
    wfit=wfit+1;
   end
  end
  rnw=zeros(wfit,1);
  rdcnhw=zeros(wfit,1);
  %*******************************************************************
  count=1;
  for m=1:N(1);
   if rn(m) >= hn(k) & rn(m) <= hc(k)  ;
    rnw(count)=rn(m);
```

```
    rdcnhw(count)=rdcnh(m);
    count=count+1;
   end
  end
  %  PERFORM THE FIT
  start=0;
  Amax=max(rdcnhw);
  Amin=min(rdcnhw);
  [x0,y0]=lsqnonlin('sigfw', start);
  phi=x0(1); % the phase is fit here

%     hold on
  [per,y0]=period_analysis_v2(rnw,rdcnhw)


  if k == 1
    rn1=linspace(min(rnw), max(rnw), 10*N(1));
    [x0,y0]=lsqnonlin('sigfw', start);
    phi=x0(1); % the phase is fit here
    figure(1)
    hold on
    [per,y0]=period_analysis_v2(rnw,rdcnhw)
    L1=(Amax+Amin)/2+(Amax-Amin)/2*sin(2*pi*rn1/per+phi);
    plot(rn,rdcnh,'ko',rn1,L1,'r')
  end
  if k == 2
    rn2=linspace(min(rnw), max(rnw), 10*N(1));

    [x0,y0]=lsqnonlin('sigfw', start);
    phi=x0(1); % the phase is fit here
    [per,y0]=period_analysis_v2(rnw,rdcnhw)
    L2=(Amax+Amin)/2+(Amax-Amin)/2*sin(2*pi*rn2/per+phi);
    hold on
    plot(rn,rdcnh,'ko',rn2,L2,'r')
  end
  if k == 3
    rn3=linspace(min(rnw), max(rnw), 10*N(1));
    L3=(Amax+Amin)/2+(Amax-Amin)/2*sin(2*pi*rn3/3+phi); %changed to 3
  end
  if k == 4
    rn4=linspace(min(rnw), max(rnw), 10*N(1));
    L4=(Amax+Amin)/2+(Amax-Amin)/2*sin(2*pi*rn4/3.6+phi);
  end
  if k == 5
    rn5=linspace(min(rnw), max(rnw), 10*N(1));
    L5=(Amax+Amin)/2+(Amax-Amin)/2*sin(2*pi*rn5/3.6+phi);
  end
  diff=(rdcnhw-((Amax+Amin)/2+(Amax-Amin)/2*sin(2*pi*rnw/3.6+phi))).^2;
  rmserror=sqrt(sum(diff)/count)
end
```

---NEEDS ---

Above script needs windowLoop.m and sigfw.m

```
function [ bphase,score, position] = windowLoop( x )
%UNTITLED4 Summary of this function goes here
%   Detailed explanation goes here
% wsize=5;wsize=wsize-1;
wsize = x
global rn
global rdcnh
global rnw
global rdcnhw
global N
N=size(rdcnh);
for i=min(rn):max(rn)-wsize;

%**********************************************************************
%  HERE I MAKE SURE THAT THE WINDOW SIZE IS SET TO THE RIGHT NUMBER OF
%    MEASURED VALUES.
  wmax=i+wsize;
  wcount=0;
  for jcount=1:N(1)
    if rn(jcount) >=i & rn(jcount) <= wmax
      wcount=wcount+1;
    end
  end
rnw=zeros(wcount,1);rdcnhw=zeros(wcount,1);
count=1;
%**********************************************************************
%  HERE I MAKE THE VECTORS rnw, rdcnhw BETWEEN i AND i+wmax BY SORTING

  for j=1:N(1)
    if rn(j) >= i & rn(j) <= wmax
      rnw(count)=rn(j);rdcnhw(count)=rdcnh(j);count=count+1;
    end
  end

%  WITH THIS WINDOW MAKE THE BEST FITTING SINUSOID
    M=size(rnw);Amax=max(rdcnhw);Amin=min(rdcnhw);
    start(1)=0;
    off=0;
    if M(1) > 1
      [x0,y0]=fminsearch('sigfw', start);
      phi=x0(1);
      per=3.4;
      rn0=linspace(min(rnw), max(rnw), 10*M(1));
      L0=(Amax+Amin)/2+(Amax-Amin)/2*sin(2*pi*rn0/3.0+phi+off);
      diff=(rdcnhw-((Amax+Amin)/2+(Amax-Amin)/2*sin(2*pi*rnw/3+phi+off))).^2;   %
      bphase(i)=phi*(180/pi);
      score(i)=sum(diff)/M(1);
      position(i)=i+(wsize/2);
    end
%  FOR MISSING RESIDUES A WINDOW WITH ONE MEASUREMENT OR LESS IS NOT USED
    if M(1) <= 1
      position(i)=i+(wsize/2);diff=1000;score(i)=20;bphase(i)=500;
    end
```

```
  i  ;
end
end

%%****************SIGW%%** *********************************************
%      FUNCTION sigfw    Michael Mesleh  02/02                        *
%  This function will only allow the phase to vary in attempting to fit a sinusoid to experimentally
measured RDCs.                         *
%*********************************************************************

function z=sigfw(x)

global rn
global rdcnh
global rnw
global rdcnhw

off=0;
Amax=max(rdcnhw);
Amin=min(rdcnhw);
N=size(rdcnhw);

phi=x(1);

L=(Amax+Amin)/2+(Amax-Amin)/2*sin(2*pi*rnw/3.6+phi+off);

z=(L-rdcnhw)'*(L-rdcnhw);
```

--- period_analysis_v2.m Addendum ---

```
global rn
global rdcnh
global rnw
global rdcnhw
  [x0,y0]=fminsearch('sigfw', 0);
    phi=x0(1); % the phase is fit here
N=size(rdcnh);
wsize=5;wsize=wsize-1;
windowLoop(wsize)

ym=phi;
yData=rdcnhw;
xData=rnw;
yu = max(yData);
yl = min(yData);
yr = (yu-yl);     % Range of ëyí

yz=yData-yu+(yr/2)
% yData=(2*(yData-yl)/(yu-yl))-1 % Normalize from -1 to 1
% yr=2 %replace if needed
% zx = xData(yz .* circshift(yz,[0 1]) <= 0);
zx = xData(yz .* circshift(yz,[0 1]) <= median(yz)) % Find zero-crossings
```

```
% zx = xData(yData .* circshift(yData,[-1 0]) <= 0)
clear diff
per = 2*mean(diff(zx,1))                    % Estimate period
% per=3.0999999
% ym = mean(yData);                              % Estimate offset
fit = @(b,x)  b(1).*(sin(2*pi*x./b(2) + 2*pi/b(3))) + b(4);    % Function to fit
fcn = @(b) sum((fit(b,xData) - yData).^2);                             % Least-Squares cost function
s2 = fminsearch(fcn, [yr;  per;  -1;  ym]);
period=per;
% xptm2 = linspace(min(xData),max(xData));
%
% plot(xData,yData,'o', xptm2,fit(s2,xptm2), 'r')
yy=(yData-((yu+yl)/2+(yu-yl)/2*sin(2*pi*xData/per+ym))).^2;
rmserror=sqrt(sum(yy)/1);
```

--- RDC Extraction from Intensity Ratios ---

```
clear data
clc
close all

load('session_20180320_positive_charge.mat')

% ######### Afer sorting
Ia = data(:,2); % attenuated intensity
Ir = data(:,3); % reference int
% Ia2=data(:,4);
% ###################
Q=Ia./Ir; % intensity ratio
% Q2=Ia2./Ir;
T = 10.7/1000;     % ms modified time for INEPT delay, see manuscript
Jnh = -92;         % (value Bax used) scalar coupling for HN bond
Dnh = -1/T-Jnh+2/(pi()*T).*asin(Q/2);

figure(1)
plot(data(:,1),Dnh,'-o')
```

---PRE Modeling ---

```
% Relaxation contribution from the spin label converted to Distance in
% Angstroms. This is to simulated the distance dependence from a nitroxide
% spin label and the effect it has on nearby spins. The x-axis is
% R2sp=R2*-R2. The Distance is converted as described in the listed paper.

clear all
FWHH=50;       %Constant LW for simplicity (Hz)
Del=11.11E-3;   %INEPT delay (sec)(=1/JNH)
MHz=850;        % is the proton (1H)frequency at a given magentic field strength
Tc=25E-9;        %Correlation time (sec)
gammaH=2.67522E8;    %Larmor frequency for proton
K=1.23E-32;          %Group of constants, cm^6/s^2(see Biochemistry 2000, v39, pp5355-5365)
R2=(pi().*FWHH)';     %Transverse Relaxation Rate (1/sec)

B0=0.0235*MHz;      %Magnetic Field Strength in Tesla
```

```
OmegaH=-gammaH*B0;   %in rad/s

R2sp=linspace(5,100);
a=K./R2sp;
b=4*Tc;
c=3*Tc;
d=1+(power(OmegaH,2).*power(Tc,2));
f=1/6;
r=(a.*(b+(c/d))).^(f);
rAng=(r.*1E8);
plot(R2sp,rAng)
set(gca,'FontName','Arial','TickDir','out','TickLength',[0.03 0],...
    'LineWidth',1.5,'FontSize',12,'Color','none','XColor',[0 0 0]...
,'YColor',[0 0 0],'YAxisLocation','origin','Box','off');

xlabel('\Gamma_2 (Hz)')
ylabel('Distance to MTSL Spin Label (Angstom)')
title('Paramagnetic Relaxation Enhancement Distane Model')
```

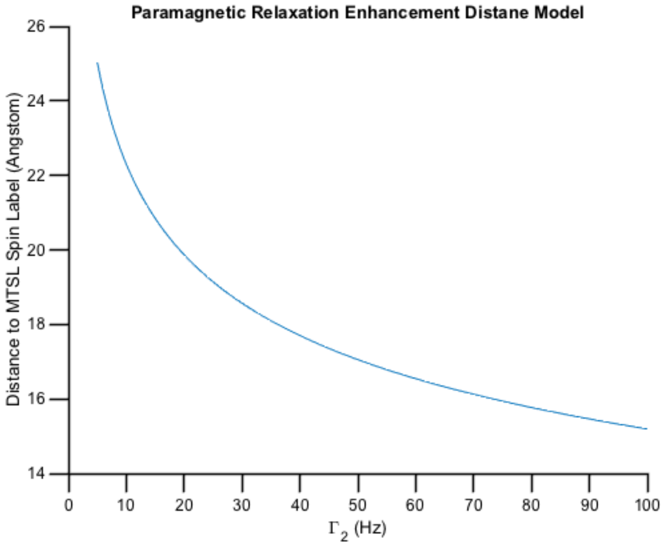

Figure S4.2 PRE distance dependence model. The PRE formula modeled to show the relationship between the relaxation contribution from the spin label (Γ (Hz)) and the distance to the spin label.

--- PRE Relaxation Decay Measurements ---

```
clear
load('matlab.mat')
time=[S60CReduced.VarName3(1,:) S60CReduced.VarName4(1,:) ...
    S60CReduced.VarName5(1,:) S60CReduced.VarName6(1,:)]/1000;
n=size(S60CReduced);
count=0;
for i=2:n(1)
```

```
    count=count+1;
    DATA(count,:)=[S60CReduced.VarName3(i,:),...
        S60CReduced.VarName4(i,:),S60CReduced.VarName5(i,:),...
        S60CReduced.VarName6(i,:)];
end

n=size(DATA);
count=0;
for i=1:n(1)
    count=count+1;
    [xData,yDATA]=prepareCurveData(time,DATA(i,:));
    f=fit(xData,yDATA,'exp1','StartPoint',[max(yDATA) 0]);
    figure(i)
    plot(f,xData,yDATA)
    a=coeffvalues(f);
    Red_decay(i,:)=a(2);
end

time=[S60COxydized.VarName3(1,:) S60COxydized.VarName4(1,:) ...
    S60COxydized.VarName5(1,:) S60COxydized.VarName6(1,:) ...
    S60COxydized.VarName7(1,:)]/1000;

clear DATA
n=size(S60COxydized);
count=0;
for i=2:n(1)
    count=count+1;
    DATA(count,:)=[S60COxydized.VarName3(i,:),...
        S60COxydized.VarName4(i,:),S60COxydized.VarName5(i,:)...
        S60COxydized.VarName6(i,:)...
        S60COxydized.VarName7(1,:)];
end

n=size(DATA);
count=0;
for i=1:n(1)
    count=count+1;
    [xData,yDATA]=prepareCurveData(time,DATA(i,:));
    f=fit(xData,yDATA,'exp1','StartPoint',[max(yDATA) 0]);
    figure(i)
    plot(f,xData,yDATA)
    a=coeffvalues(f);
    Ox_decay(i,:)=a(2);
end
```

--- PRE Distance Measurements from Relaxation Decay---

```
% Theoretical PREs
% clear all
FWHH=50;      %Constant LW for simplicity (Hz)
Del=11.11E-3; %INEPT delay (sec)(=1/JNH)
MHz=850;      % is the proton (1H)frequency at a given magnetic field strength
Tc=25E-9;     %Correlation time (sec)
gammaH=2.67522E8;  %Larmor frequency for proton
```

```
K=1.23E-32;        %Group of constants, cm^6/s^2(see Biochemistry 2000, v39, pp5355-5365)
R2=(pi().*FWHH)';  %Transverse Relaxation Rate (1/sec)

B0=0.0235*MHz;     %Magnetic Field Strength in Tesla
OmegaH=-gammaH*B0; %in rad/s

%% Create a matrix named temp, and paste in relaxation R2sp and res#

res=temp(:,1);
R2sp=temp(:,2);
a=K./R2sp;
b=4*Tc;
c=3*Tc;
d=1+(power(OmegaH,2).*power(Tc,2));
f=1/6;
r=(a.*(b+(c/d))).^(f);

rAng=(r.*1E8);

b=bar(res,rAng);
%Pretty plotting
set(gca,'FontName','Arial','TickDir','out',...
    'TickLength',[0.03 0],'LineWidth',1.5,...
    'FontSize',12,'Color','none','XColor',[0 0 0],...
    'YColor',[0 0 0],'XDir','normal','YDir','normal',...
    'Box','off','XScale','linear');
resi=res-44;
table([resi],[rAng])
T=([resi rAng])
xlswrite('20180905_S60_restraints.xlsx',T)
```

--- Temperature Coefficient Analysis ---

```
clear
close all
clc

load('20180627_tempcoef_session.mat');
HN_30=exportedshifts20180627.VarName7;
HN_325=exportedshifts20180627.VarName9;
HN_35=exportedshifts20180627.VarName11;
HN_375=exportedshifts20180627.VarName13;
HN_40=exportedshifts20180627.VarName15;
HN_425=exportedshifts20180627.VarName17;
HN_475=exportedshifts20180627.VarName19;

temperature_series=[HN_30(1,1) HN_325(1,1)...
    HN_35(1,1) HN_375(1,1) HN_40(1,1) HN_425(1,1)...
    HN_475(1,1) ];

DATA=[HN_30(2:end,1) HN_325(2:end,1)...
    HN_35(2:end,1) HN_375(2:end,1) HN_40(2:end,1) HN_425(2:end,1)...
    HN_475(2:end,1)];
```

```
DdHN=DATA(1:49,:) -DATA(1:49,end); % 49 b/c the first row is the temperature in the original data,
change accordingly


% plot(temperature_series,DdHN,'o');
% The temperature coefficient analysis is coded within the for loop.
close all
n=size(DdHN);
for i = 1:n(1)
% for i = find(residues==127)
   try
%   Fit chemical shift perturbation to line
   [xData,
yData]=prepareCurveData(temperature_series(1,~isnan(DdHN(i,:))),DdHN(i,~isnan(DdHN(i,:))));
   [mdl]=fitlm(xData,yData);
%     figure(i)
%     h=plot(mdl);
   decay(i,:)=mdl.Coefficients.Estimate(2);

%   Fit the residuals from line fit to quadratic equation
   [xData, yData]=prepareCurveData(temperature_series,mdl.Residuals.Raw);
   [quadl]=fitlm(xData,yData,'quadratic');
%     g=plot(quadl);
   coefficients(i,:)=quadl.Coefficients.Estimate(2);
   catch
   end
end
clc
disp('done')
%% Specific for hPIRT
close all
resi=exportedshifts20180627.SeqCode;
residues=resi(2:50,:);
% bar(residues,coefficients) %local dynamics

figure(1)
hold on
b=bar(residues,decay);
yl=(ones(size(decay))*-4.5E-3);
plot(residues,yl,'r--')
set(gca,'FontName','Arial','TickDir','out',...
   'TickLength',[0.03 0],'LineWidth',1.5,...
   'FontSize',12,'Color','none','XColor'...
   ,[0 0 0],'YColor',[0 0 0],'XDir',...
   'normal','YDir','normal');
b.LineStyle='-';
b.FaceColor=[1 0.5 0];
ylabel('\Delta\delta/\DeltaT (ppm/K))')
ylabel('\Delta\delta/\DeltaT (ppm/K)')
title('hPIRT Temperature Titration Analysis 20180627')
xlim([1 139])
```

4.5.2 Rosetta Code for de Novo hPIRT Structure Predictions

--- Modified Lipophilic File Generation Script ---

Add `$url="http://tanto.bioe.uic.edu/lips/lips.txt";`
Instead of `$url="http://gila.bioengr.uic.edu/cgi-bin/lips/script.cgi";`

--- Human PIRT Span File Starting at Residue Number 54 ---

```
TM region prediction for hPirt.octopus predicted using OCTOPUS
2 93
antiparallel
n2c
  11   31   11   31
  52   70   52   70
```

--- Human PIRT lips4 File from Run Lips Script---

The lipophilic file is needed for implicit membrane protocols.[60, 72, 111]

```
Lipid exposed data: resnum mean-lipo lipophil entropy
    15  -1.000   2.760   1.000
    18  -1.000   0.700   1.000
    19  -1.000   0.700   1.000
    22  -1.000   3.420   1.000
    25  -1.000   0.700   1.000
    26  -1.000   3.540   1.000
    29  -1.000   1.440   1.000
    11  -1.000   1.980   1.000
    12  -1.000   2.220   1.000
    11  -0.500   1.980   1.000
    14  -0.500   2.220   1.000
    15  -0.500   2.760   1.000
    18  -0.500   0.700   1.000
    21  -0.500   3.760   1.000
    22  -0.500   3.420   1.000
    25  -0.500   0.700   1.000
    28  -0.500   3.760   1.000
    29  -0.500   1.440   1.000
    12  -0.500   2.220   1.000
    15  -0.500   2.760   1.000
    16  -0.500   1.100   1.000
    19  -0.500   0.700   1.000
    22  -0.500   3.420   1.000
    23  -0.500   3.420   1.000
    26  -0.500   3.540   1.000
    29  -0.500   1.440   1.000
    30  -0.500   2.320   1.000
    17   1.000   3.540   1.000
    20   1.000   1.640   1.000
    21   1.000   3.760   1.000
    24   1.000   3.940   1.000
```

27	1.000	3.540	1.000
28	1.000	3.760	1.000
31	1.000	2.360	1.000
13	1.000	1.960	1.000
14	1.000	2.220	1.000
13	0.500	1.960	1.000
16	0.500	1.100	1.000
17	0.500	3.540	1.000
20	0.500	1.640	1.000
23	0.500	3.420	1.000
24	0.500	3.940	1.000
27	0.500	3.540	1.000
30	0.500	2.320	1.000
31	0.500	2.360	1.000
14	0.500	2.220	1.000
17	0.500	3.540	1.000
18	0.500	0.700	1.000
21	0.500	3.760	1.000
24	0.500	3.940	1.000
25	0.500	0.700	1.000
28	0.500	3.760	1.000
31	0.500	2.360	1.000
52	-1.000	3.140	1.000
55	-1.000	2.360	1.000
56	-1.000	0.700	1.000
59	-1.000	2.040	1.000
62	-1.000	2.020	1.000
63	-1.000	0.700	1.000
66	-1.000	3.300	1.000
69	-1.000	2.220	1.000
70	-1.000	2.220	1.000
55	-0.500	2.360	1.000
58	-0.500	2.040	1.000
59	-0.500	2.040	1.000
62	-0.500	2.020	1.000
65	-0.500	3.540	1.000
66	-0.500	3.300	1.000
69	-0.500	2.220	1.000
56	-0.500	0.700	1.000
59	-0.500	2.040	1.000
60	-0.500	3.420	1.000
63	-0.500	0.700	1.000
66	-0.500	3.300	1.000
67	-0.500	3.540	1.000
70	-0.500	2.220	1.000
52	-0.500	3.140	1.000
53	-0.500	2.360	1.000
57	1.000	3.420	1.000
60	1.000	3.420	1.000
61	1.000	3.540	1.000
64	1.000	3.420	1.000
67	1.000	3.540	1.000
68	1.000	1.300	1.000
53	1.000	2.360	1.000
54	1.000	1.380	1.000

```
53  0.500  2.360  1.000
56  0.500  0.700  1.000
57  0.500  3.420  1.000
60  0.500  3.420  1.000
63  0.500  0.700  1.000
64  0.500  3.420  1.000
67  0.500  3.540  1.000
70  0.500  2.220  1.000
54  0.500  1.380  1.000
57  0.500  3.420  1.000
58  0.500  2.040  1.000
61  0.500  3.540  1.000
64  0.500  3.420  1.000
65  0.500  3.540  1.000
68  0.500  1.300  1.000
```

--- Fragment Generation Flags ---

Specific flags for calculating fragments with chemical shift data.[52]

```
#-mute all
-out:level 300
-in:file:vall
/usr/local/apps/rosetta/cs_rosetta/csrosetta3/frag_picker/csrosetta_vall.2008.apr24/vall.dat.2008.apr24.vCS
-frags:n_frags           200
-frags:frag_sizes         3 9
-frags:describe_fragments frags.fsc.score
#-out:file:frag_prefix     hPIRT_DPC_trimmed.fasta.frags
-out:file:frag_prefix     frags.score
-frags:scoring:config     hPIRT_DPC_trimmed.fasta.scores.cfg
-in:file:checkpoint       hPIRT_DPC_trimmed.fasta.checkpoint
-in:file:fasta            hPIRT_DPC_trimmed.fasta
-frags:ss_pred            hPIRT_DPC_trimmed.fasta.talos/predSS.tab psipred
#-frags:ss_pred           hPIRT_DPC_trimmed.fasta.talos/predSS.tab talos
-in:file:talos_phi_psi    hPIRT_DPC_trimmed.fasta.talos/pred.tab
-frags:sigmoid_cs_A       2
-frags:sigmoid_cs_B       4
```

--- Checkpoint Generation Script ---

This perl script is necessary to output a checkpoint file that needs be present for the fragment generation. This was adapted from the run_lips.pl script above. It needs a file called checkpoint_gen.pl, which is used to convert the check matrix to Fortran and is present in the Rosetta bundle.

```
#!/usr/bin/perl -w
##########################################################################################
###############
# Adapted by Nicholas J Sisco from a similar script by Bjorn Wallner and Vladimir Yarov-Yarovoy  i
#
#                                                                                #
# outputs blast, and checkpoint for fragment generations                                  #
# ab initio protocol                                                                #
##########################################################################################
###############
```

```
if ($#ARGV < 3) {
   print STDERR "usage: $0 <fasta file> <path to blastpgp>  <path to alignblast.pl script> <rosettahome>
<checkpointpath>  \n";
   print STDERR "example: $0 BRD4.fasta /home/nick/csrosetta/cs_rosetta/csrosetta3/frag_picker/blast-
2.2.26/bin/blastpgp
/home/nick/rosetta_ns/rosetta_bin_linux_2017.08.59291_bundle/tools/membrane_tools/alignblast.pl
rosettahome_path checkpoint_gen_path \n";
   exit -1;
}

$seq=$ARGV[0];
$PSIBLAST=$ARGV[1]; # path to blastpgp
$parseblast=$ARGV[2]; #path to alignblast.pl
$Rosettahome=$ARGV[3]; #path to rosetta home
$checkpointpath=$ARGV[4]; #path to checkpoint_gen.pl
$sequence=`grep -v '>' $seq`;
$sequence=~s/\n//g;

$blastout=$seq;
$blastout=~s/fasta/blast/g;

if(!-e $blastout)
{
     $psiblast_command="$PSIBLAST -t T -i $seq -F F -j2 -o $blastout -d nr -v10000 -b10000 -K1000 -
h0.0009 -e0.0009 -C check.chk -Q $blastout.fasta.pssm -a 4";
     print "Running:\n $psiblast_command\n";
     `$psiblast_command`;
}
if(!-e "$blastout.msa")
{
   `$parseblast $blastout $blastout.msa -psi`;
}

# psi-blast

if(!-e "$blastout.msa")
{
   `$parseblast $blastout $blastout.msa -psi`;
}

#$seq=$ARGV[0];
#$Rosettahome=$ARGV[1]; #path to rosetta home
$checkname='check.chk';

open(OUT,">sstmp.pn");
{
  $data = system("echo $checkname > sstmp.pn");
}
close(OUT);
open(OUT,">sstmp.sn");
{
  $data = system("echo $seq > sstmp.sn");
}
close(OUT);
```

```
system("$Rosettahome/tools/fragment_tools/blast/bin/makemat -P sstmp");
system("cp -f $checkname temp.check");
system("$checkpointpath/checkpoint_gen.pl $seq");
system("mv temp.checkpoint $seq.checkpoint");
system("rm -rf sstmp*");
```

4.5.3 RASREC Flags

--- flags_denovo ---

```
-run:protocol broker

-in:file:frag3 frags.score.200.3mers.gz
-in:file:frag9 frags.score.200.9mers.gz
-in:file:fasta hPIRT_DPC.fasta

-constraints:epr_distance


-out:file:silent_print_all_score_headers


#-out:file:silent_struct_type protein_float
#-in:file:silent_struct_type protein_float

-increase_cycles 2.000000

#jumping
-templates::topology_rank_cutoff 0.8
-jumps:ramp_chainbreaks
-jumps:sep_switch_accelerate 0.8
-abinitio:skip_convergence_check
-jumps:overlap_chainbreak

#magic energy fixes
-rsd_wt_helix 0.5
-rsd_wt_loop 0.5
-rg_reweight 0.5

# for loop closing
-overwrite_filter_scorefxn score3

-detect_disulf false

#loop-closing filter in SlidingWindow
-fast_loops:overwrite_filter_scorefxn score3

-abrelax:fail_unclosed

#log-output
-unmute memory_usage
-out:levels core.chemical:error
-out:levels core.io.pdb:error
-out:levels protocols.jobdist:error
```

```
@flags_membrane
@flags_nmr_patches
```

--- flags_membrane ---

```
#i/o
-broker:setup ./setup_membrane.tpb
-abinitio:stage2_patch  ./score_membrane_s2.wts_patch
-abinitio:stage3a_patch ./score_membrane_s3a.wts_patch
-abinitio:stage3b_patch ./score_membrane_s3b.wts_patch
-abinitio:stage4_patch  ./score_membrane_s4.wts_patch

-score:weights membrane_highres_Menv_smooth.wts

-in::file::spanfile ./hPIRT_DPC.span
-in::file::lipofile ./hPIR.lips4


-rg_reweight 0.01
-run:reinitialize_mover_for_each_job

-score:find_neighbors_3dgrid

-abinitio:membrane
-membrane:fixed_membrane
-membrane:no_interpolate_Mpair
-membrane:Menv_penalties
-membrane:Membed_init
-relax

-iterative:fa_score membrane_highres_Menv_smooth.wts
-iterative:cen_score score3
-iterative:cen_score_patch membrane_pool_patch

-membrane:center_search
-membrane:normal_search
```

--- flags_iterative ---

```
# i/o
-iterative:enumerate:skip_half
-iterative:pool_size 500 #100 is quick 1000 sucks the RAM
-iterative:accept_ratio 0.1 0.1 0.1 0.1 0.1 0.1 0.1 0.1
-jumps::max_strand_gap_allowed 10
-jumps:contact_score 0.2
-iterative:rmsf_nstruct 50

-out:level 500
-out:levels all:warning
-out:levels protocols.jd2.MPIArchiveJobDistributor:info
-out:levels protocols.jd2.Archive:debug
-out:levels protocols.iterative:info
-out:levels core.util.prof:info
```

```
#obsolete
-iterative:evaluate_only_on_slaves

-iterative:fa_score talaris2014
-iterative:cen_score score3

#Stages:
# (1)  SS-RANDOM
# (2)  MIX
# (3)  BETA-TOP
# (4)  RESAM
# (5)  NOE-BETA-TOP
# (6)  NOE-RESAM
# (7)  CEN2FULL
# (8)  FULL-REFINE

-iterative:max_nstruct 0 0 0 0 -1 -1 0 0
-iterative:min_diversity 0 0 0 2.0 3.0 2.0 2.0 1.5
-iterative:fullatom
-iterative:force_topology_resampling

-iterative:safety_hatch_scorecut 0.1
-iterative::super_quick_relax_patch ../patches/super_quick_relax.patch

#this is the relative weight the noesy-cst will have for filtering
#the relative weight provided in the following is multiplied with the overall weight for
atom_pair_constraint in the patches
#given by -iterative:cen_score_patch and -iterative:fa_score_patch
-iterative:cenpool_noesy_cst_weight 1
-iterative:fapool_noesy_cst_weight 1

#exit as soon as queue is drained
-jd2:mpi_nowait_for_remaining_jobs
-jd2:mpi_timeout_factor 0

-iterative:flags_fullatom flags_fullatom

#important to obtain intermediate structures for proto-fold resampling (aka stage2 resampling)
-abinitio:debug
-abinitio:debug_structures

-archive:completion_notify_frequency 25
```

--- flags_rasrec ---

```
-broker:setup setup_init.tpb
@flags_cs_rescore

-in:file:rdc RDC_pos.tab
-rdc:fix_normAzz 0.014298
-rdc:fit_method svd

-in:file:rdc RDC_neu.tab
#-rdc:fix_normAzz 0.022637
```

```
-rdc:fit_method svd
```

--- flags_nmr_patches ---

All of the nmr patch files can be located in the Rosetta bundle demo folder under ab initio with chemical shift, RDC, and NOE data.

--- setup_init.tpb ---

```
#i/o

CLAIMER ConstraintClaimer
file NOE_20180822.tab-cen
CENTROID
SKIP_REDUNDANT 0
FILTER_WEIGHT 1.00
FILTER_NAME NOE_restraints
END_CLAIMER

CLAIMER ConstraintClaimer
file NOE_20180822.tab
FULLATOM
NO_CENTROID
SKIP_REDUNDANT 0
FILTER_WEIGHT 1.00
FILTER_NAME NOE_restraints_FA
END_CLAIMER


CLAIMER ConstraintClaimer
file PRE_20180824.tab
CENTROID
SKIP_REDUNDANT 0
FILTER_WEIGHT 1.00
FILTER_NAME pre_restraints
END_CLAIMER

CLAIMER ConstraintClaimer
file PRE_20180824.tab
FULLATOM
NO_CENTROID
SKIP_REDUNDANT 0
FILTER_WEIGHT 1.00
FILTER_NAME pre_restraints_FA
END_CLAIMER

CLAIMER ConstraintClaimer
file COHN.cst
FULLATOM
CENTROID
SKIP_REDUNDANT 0
FILTER_WEIGHT 1.00
FILTER_NAME HydrogenBonding
END_CLAIMER
```

--flags_fullatom ---

```
## Keywords that are replace are listed in ~mtyka/homo_bench/help_keywords.txt

#-relax:sequence
-relax:fast
-relax:ramady
-abinitio:close_loops
-loops:idealize_before_loop_close
-loops:idealize_after_loop_close
-abinitio::clear_pose_cache
-short_frag_cycles 1
-scored_frag_cycles 1
-non_ideal_loop_closing
-alternative_closure_protocol
-fast_loops:window_accept_ratio .01
-fast_loops:nr_scored_sampling_passes 4
-fast_loops:min_breakout_good_loops 5
-fast_loops:min_breakout_fast_loops 80
-fast_loops:min_fast_loops 3
-fast_loops:min_good_loops 0
-fast_loops:nr_scored_fragments 20
-fast_loops:vdw_delta 0.5
-fast_loops:give_up 1000
```

4.5.4 Rosetta Constraint Files

These files are for hPIRT residues from 54 to 137, with numbering 1 through 93.

---COHN.cst---

```
#Hydrogen Bonding in alpha helix
AtomPair  H  18  O  14  BOUNDED  1.5  2.5  0.5 NOE
AtomPair  H  19  O  15  BOUNDED  1.5  2.5  0.5 NOE
AtomPair  H  25  O  21  BOUNDED  1.5  2.5  0.5 NOE
AtomPair  H  27  O  23  BOUNDED  1.5  2.5  0.5 NOE
AtomPair  H  28  O  24  BOUNDED  1.5  2.5  0.5 NOE
AtomPair  H  32  O  28  BOUNDED  1.5  2.5  0.5 NOE
AtomPair  H  51  O  47  BOUNDED  1.5  2.5  0.5 NOE
AtomPair  H  53  O  49  BOUNDED  1.5  2.5  0.5 NOE
AtomPair  H  55  O  51  BOUNDED  1.5  2.5  0.5 NOE
AtomPair  H  56  O  52  BOUNDED  1.5  2.5  0.5 NOE
AtomPair  H  57  O  53  BOUNDED  1.5  2.5  0.5 NOE
AtomPair  H  61  O  57  BOUNDED  1.5  2.5  0.5 NOE
AtomPair  H  62  O  58  BOUNDED  1.5  2.5  0.5 NOE
AtomPair  H  63  O  59  BOUNDED  1.5  2.5  0.5 NOE
AtomPair  H  76  O  72  BOUNDED  1.5  2.5  0.5 NOE
AtomPair  H  79  O  75  BOUNDED  1.5  2.5  0.5 NOE
AtomPair  H  83  O  79  BOUNDED  1.5  2.5  0.5 NOE
AtomPair  H  84  O  80  BOUNDED  1.5  2.5  0.5 NOE
AtomPair  H  86  O  82  BOUNDED  1.5  2.5  0.5 NOE
AtomPair  H  87  O  83  BOUNDED  1.5  2.5  0.5 NOE
AtomPair  H  88  O  84  BOUNDED  1.5  2.5  0.5 NOE
AtomPair  H  89  O  85  BOUNDED  1.5  2.5  0.5 NOE
AtomPair  H  90  O  86  BOUNDED  1.5  2.5  0.5 NOE
AtomPair  H  91  O  87  BOUNDED  1.5  2.5  0.5 NOE
AtomPair  H  92  O  88  BOUNDED  1.5  2.5  0.5 NOE
```

---PRE.cst---

```
# Included are only PRE's from well resolved resonances
# With a BOUNDED constraint
#   C106
AtomPair   CB  62  H   25     BOUNDED 10.2    22.2    6   0.5
AtomPair   CB  62  H   26     BOUNDED 10.6    22.6    6   0.5
AtomPair   CB  62  H   51     BOUNDED 11.7    23.7    6   0.5
AtomPair   CB  62  H   56     BOUNDED 16.5    28.5    6   0.5
AtomPair   CB  62  H   82     BOUNDED 10.4    18.4    6   0.5
AtomPair   CB  62  H   85     BOUNDED 17.2    29.2    6   0.5
AtomPair   CB  62  H   87     BOUNDED 16.1    28.1    6   0.5
AtomPair   CB  62  H   88     BOUNDED 16.5    28.5    6   0.5
AtomPair   CB  62  H   89     BOUNDED 15.5    27.5    6   0.5
AtomPair   CB  62  H   90     BOUNDED 14.5    26.5    6   0.5
AtomPair   CB  62  H   91     BOUNDED 14.0    26.0    6   0.5
AtomPair   CB  62  H   92     BOUNDED 13.8    25.8    6   0.5
AtomPair   CB  62  H   93     BOUNDED 15.8    27.8    6   0.5
#   S124C
AtomPair   CB  80  H   16     BOUNDED 10.8    22.8    6   0.5
AtomPair   CB  80  H   26     BOUNDED 11.8    23.8    6   0.5
AtomPair   CB  80  H   51     BOUNDED 10.2    22.2    6   0.5
AtomPair   CB  80  H   56     BOUNDED 11.9    23.9    6   0.5
AtomPair   CB  80  H   91     BOUNDED 15.2    27.2    6   0.5
AtomPair   CB  80  H   92     BOUNDED 14.5    26.5    6   0.5
AtomPair   CB  80  H   93     BOUNDED 15.1    27.1    6   0.5
#EPR    C74-H120C
AtomPair   CB  30  CB  76  SPLINE  EPR_DISTANCE    50.0    5   0.5
#C74
AtomPair   CB  30  H   91     BOUNDED 20.4    32.4    6   0.5
AtomPair   CB  30  H   92     BOUNDED 20.8    32.8    6   0.5
AtomPair   CB  30  H   93     BOUNDED 22.2    34.2    6   0.5
#S60C
AtomPair   CB  16  H   26     BOUNDED 14.8    26.8    6   0.5
AtomPair   CB  16  H   56     BOUNDED 15.6    27.6    6   0.5
AtomPair   CB  16  H   63     BOUNDED 15.9    22.9    6   0.5
AtomPair   CB  16  H   81     BOUNDED 15.9    24.9    6   0.5
AtomPair   CB  16  H   82     BOUNDED 15.9    25.9    6   0.5
AtomPair   CB  16  H   87     BOUNDED 15.3    23.3    6   0.5
AtomPair   CB  16  H   91     BOUNDED 15.9    25.9    6   0.5
AtomPair   CB  16  H   92     BOUNDED 15.5    23.5    6   0.5
AtomPair   CB  16  H   93     BOUNDED 15.3    24.3    6   0.5
```

---NOE.cst---

```
# NOE Table
AmbiguousNMRDistance H 55 H 56 BOUNDED 3 5 0.3 NOE; rawdata 3.7
AmbiguousNMRDistance H 57 H 56 BOUNDED 3 5 0.3 NOE; rawdata 3.99
AmbiguousNMRDistance HA 55 H 19 BOUNDED 2 4 0.3 NOE; rawdata 3.59
AmbiguousNMRDistance HA 56 H 19 BOUNDED 3 5 0.3 NOE; rawdata 3.91
AmbiguousNMRDistance H 86 H 90 BOUNDED 3 5 0.3 NOE; rawdata 4
AmbiguousNMRDistance H 87 H 89 BOUNDED 3 5 0.3 NOE; rawdata 3.5
AmbiguousNMRDistance H 87 H 88 BOUNDED 2.5 3.5 0.3 NOE; rawdata 3.14
AmbiguousNMRDistance H 86 H 87 BOUNDED 4 6 1.5 NOE; rawdata 4.16
AmbiguousNMRDistance H 87 H 88 BOUNDED 1.5 3 0.3 NOE; rawdata 3.14
```

```
AmbiguousNMRDistance HA 92 H 93 BOUNDED 1.8 3 0.3 NOE; rawdata 2.48
AmbiguousNMRDistance HA 88 H 89 BOUNDED 1.8 3 0.3 NOE; rawdata 2.88
AmbiguousNMRDistance HA 88 H 89 BOUNDED 1.8 3 0.3 NOE; rawdata 2.65
AmbiguousNMRDistance H 51 H 52 BOUNDED 3 5 0.3 NOE; rawdata 3.7
AmbiguousNMRDistance H 18 H 16 BOUNDED 2 4 0.3 NOE; rawdata 3.54
AmbiguousNMRDistance H 16 H 19 BOUNDED 4 6 0.5 NOE; rawdata 3.93
AmbiguousNMRDistance H 25 H 27 BOUNDED 4 6 0.5 NOE; rawdata 3.93
AmbiguousNMRDistance H 28 H 25 BOUNDED 4 6 0.5 NOE; rawdata 3.94
AmbiguousNMRDistance H 29 H 28 BOUNDED 2 4 0.3 NOE; rawdata 3.69
AmbiguousNMRDistance H 54 H 53 BOUNDED 4 6 0.5 NOE; rawdata 3.73
AmbiguousNMRDistance H 53 H 54 BOUNDED 4 6 0.5 NOE; rawdata 3.83
AmbiguousNMRDistance H 54 H 55 BOUNDED 4 6 0.5 NOE; rawdata 3.83
AmbiguousNMRDistance H 55 H 56 BOUNDED 4 6 0.5 NOE; rawdata 3.7
AmbiguousNMRDistance H 56 H 57 BOUNDED 4 6 0.5 NOE; rawdata 3.99
AmbiguousNMRDistance H 56 H 53 BOUNDED 4 6 0.5 NOE; rawdata 3.9
AmbiguousNMRDistance H 80 H 81 BOUNDED 2 4 0.3 NOE; rawdata 3.53
```

---RDC.cst---

```
#Positive
14  N   14  H   -1.7646127
15  N   15  H   -1.0446426
16  N   16  H   18.585933
17  N   17  H   8.7710583
18  N   18  H   6.5230368
19  N   19  H   6.3926234
23  N   23  H   -3.6143211
26  N   26  H   8.6319827
27  N   27  H   -0.93977779
28  N   28  H   16.066476
29  N   29  H   -1.3840656
30  N   30  H   9.5970169
31  N   31  H   -3.2794322
32  N   32  H   -2.5950404
33  N   33  H   24.308671
34  N   34  H   2.3538311
35  N   35  H   -3.8763066
37  N   37  H   2.1789549
38  N   38  H   -1.7877628
42  N   42  H   -12.020208
43  N   43  H   -2.2739729
44  N   44  H   -4.6463766
45  N   45  H   -0.72544411
51  N   51  H   19.531078
52  N   52  H   21.812302
53  N   53  H   10.42342
54  N   54  H   13.96968
55  N   55  H   1.4802333
56  N   56  H   10.698924
57  N   57  H   -2.0272648
61  N   61  H   -0.53821656
62  N   62  H   15.361684
66  N   66  H   -1.2014526
72  N   72  H   -2.6273005
73  N   73  H   -4.1700327
```

```
74 N 74 H -1.1385044
75 N 75 H 3.2239537
76 N 76 H -1.2163819
77 N 77 H 0.57430541
78 N 78 H -0.88673102
80 N 80 H -0.027875488
81 N 81 H 7.6721989
82 N 82 H 26.392434
83 N 83 H 8.3517835
84 N 84 H 4.0365085
86 N 86 H -2.5338485
87 N 87 H 3.8079525
88 N 88 H -1.5986879
89 N 89 H -13.914392
90 N 90 H -3.2398277
91 N 91 H 4.2599849
92 N 92 H -8.3619642
93 N 93 H -1.8314676
#Neutral
14 N 14 H 1.0721
15 N 15 H -3.199
16 N 16 H 7.8731
17 N 17 H 15.387
18 N 18 H 10.374
19 N 19 H 5.946
23 N 23 H 5.9532
24 N 24 H 0.9782
25 N 25 H 9.0401
26 N 26 H 8.0938
27 N 27 H -12.58
28 N 28 H 8.9581
29 N 29 H 7.0422
30 N 30 H 6.2976
31 N 31 H -8.987
32 N 32 H -12.16
33 N 33 H -2.048
34 N 34 H -2.32
35 N 35 H -4.956
37 N 37 H -4.409
38 N 38 H -4.856
42 N 42 H -0.86
43 N 43 H -0.206
44 N 44 H -5.454
45 N 45 H -0.81
51 N 51 H 12.176
52 N 52 H 10.625
53 N 53 H 6.0175
54 N 54 H 12.351
55 N 55 H 0.5737
56 N 56 H 3.3471
57 N 57 H 6.6924
61 N 61 H 8.2258
62 N 62 H 6.8411
63 N 63 H -15.5
```

```
66  N   66  H   3.6117
72  N   72  H   -5.467
73  N   73  H   -8.802
74  N   74  H   -0.334
75  N   75  H   1.8051
76  N   76  H   -1.433
77  N   77  H   -0.628
78  N   78  H   -2.517
80  N   80  H   0.0558
81  N   81  H   10.147
82  N   82  H   7.9906
83  N   83  H   12.618
84  N   84  H   7.7695
85  N   85  H   1.0812
86  N   86  H   -2.61
87  N   87  H   3.5687
88  N   88  H   -1.113
89  N   89  H   -9.998
90  N   90  H   -1.399
91  N   91  H   3.738
92  N   92  H   -5.898
93  N   93  H   -1.273
```

--- Membrane Ab Intitio Flags ---

```
#i/o
# all of these patches can be found in the demo folder
-abinitio:stage2_patch  ./score_membrane_s2.wts_patch
-abinitio:stage3a_patch ./score_membrane_s3a.wts_patch
-abinitio:stage3b_patch ./score_membrane_s3b.wts_patch
-abinitio:stage4_patch  ./score_membrane_s4.wts_patch

-score:weights membrane_highres_Menv_smooth.wts

-in::file::spanfile hPIRT_DPC.span
-in::file::lipofile hPIR.lips4

-rg_reweight 0.01
-run:reinitialize_mover_for_each_job
-score:find_neighbors_3dgrid

-abinitio:membrane
-membrane:fixed_membrane
-membrane:no_interpolate_Mpair
-membrane:Membed_init
-relax

-membrane:Menv_penalties

-membrane:center_search
-membrane:normal_search
```

--- Rosetta Comparative Modeling, rosetta_cm.options ---

```
# i/o
# Notice that EPR distance is used
```

```
-in:file:fasta inputs/pirFL.fasta
-parser:protocol rosetta_cm.xml
-nstruct 30000
-out:prefix hPirt_FL
-out:file:silent 20180825_hPIRT_FL_RosettaCM_agave.out

# relax options
-relax:minimize_bond_angles
-relax:minimize_bond_lengths
-relax:jump_move true
-default_max_cycles 200
-relax:min_type lbfgs_armijo_nonmonotone
-relax:jump_move true
-score:weights stage3_rlx_membrane.wts



-use_bicubic_interpolation
-hybridize:stage1_probability 1.0

#-keep_pose_constraint=1
-constraints:epr_distance

# reduce memory footprint
-chemical:exclude_patches LowerDNA  UpperDNA Cterm_amidation SpecialRotamer VirtualBB
ShoveBB VirtualDNAPhosphate VirtualNTerm CTermConnect sc_orbitals pro_hydroxylated_case1
pro_hydroxylated_case2 ser_phosphorylated thr_phosphorylated  tyr_phosphorylated tyr_sulfated
lys_dimethylated lys_monomethylated  lys_trimethylated lys_acetylated glu_carboxylated cys_acetylated
tyr_diiodinated N_acetylated C_methylamidated MethylatedProteinCterm

#Initialize membrane
-membrane
#-in:file:spanfile hPIRT_DPC.span
#-in:file:lipofile hPIR.lips4
-membrane:no_interpolate_Mpair
-membrane:Menv_penalties

-in:file:lipofile ./inputs/hPIR.lips4
-in:file:spanfile ./inputs/hpirt.span
```

--- Rosetta Comparative Modeling, rosetta_cm.xml ---

```
<ROSETTASCRIPTS>
   <TASKOPERATIONS>
   </TASKOPERATIONS>
   <SCOREFXNS>
      <ScoreFunction name="stage1" weights="stage1_membrane.wts" symmetric="0">
         <Reweight scoretype="atom_pair_constraint" weight="1"/>
      </ScoreFunction>
      <ScoreFunction name="stage2" weights="stage2_membrane.wts" symmetric="0">
         <Reweight scoretype="atom_pair_constraint" weight="0.5"/>
      </ScoreFunction>
      <ScoreFunction name="fullatom" weights="stage3_rlx_membrane.wts" symmetric="0">
         <Reweight scoretype="atom_pair_constraint" weight="0.5"/>
```

```
        </ScoreFunction>
    </SCOREFXNS>
    <FILTERS>
    </FILTERS>
    <MOVERS>
        <Hybridize name="hybridize" stage1_scorefxn="stage1" stage2_scorefxn="stage2"
fa_scorefxn="fullatom" batch="1" stage1_increase_cycles="2.0" stage2_increase_cycles="2.0"
linmin_only="1" frag_weight_aligned="0.2" fa_cst_file="PRE_20180613.tab" >
            <Fragments three_mers="./inputs/aapirFL03_05.200_v1_3"
nine_mers="./inputs/aapirFL09_05.200_v1_3"/>
            <Template pdb="extended" weight="1.0" cst_file="PRE_20180613.tab" />
            <Template pdb="hPIRT_to_relax_ignorechain.pdb" cst_file="AUTO" weight="0.10" />
            <Template pdb="Cterm_model_20180816.pdb" cst_file="AUTO" weight="1.000" />
            <Template pdb="tm1_model.pdb" cst_file="AUTO" weight="1.0" />
            <Template pdb="tm2_model.pdb" cst_file="AUTO" weight="1.0" />
            <Template pdb="hPIRT_on_p2x.pdb" cst_file="AUTO" weight="1.0" />
        </Hybridize>
    </MOVERS>
    <APPLY_TO_POSE>
    </APPLY_TO_POSE>
    <PROTOCOLS>
        <Add mover="hybridize"/>
    </PROTOCOLS>

</ROSETTASCRIPTS>
```

4.5.5 Rosetta Scoring Functions

These scoring patches and weights are part of the Rosetta3.8 bundle.

--- nmr_patch ---

```
atom_pair_constraint = 5.0
rdc    = 5.0
```

--- nmr_patch ---

```
chainbreak = 1
linear_chainbreak = 1.33
overlap_chainbreak = 1
atom_pair_constraint = 10
rdc    = 10
```

--- nmr_relax_patch ---

```
atom_pair_constraint = 0.1
rdc    = 0.1
```

--- score_membrane_s2.wts_patch---

```
pair = 0.0
Mpair = 1.0
env = 0.0
Menv = 2.019
cbeta = 0.0
```

```
Mcbeta = 0.0
Menv_non_helix = 2.019
Menv_termini = 2.019
Menv_tm_proj = 2.019
Mlipo = 1.0
```

--- score_membrane_s3a.wts_patch---

```
pair = 0.0
Mpair = 1.0
env = 0.0
Menv = 2.019
cbeta = 0.0
Mcbeta = 0.5
Menv_non_helix = 2.019
Menv_termini = 2.019
Menv_tm_proj = 2.019
Mlipo = 1.0
```

--- score_membrane_s3b.wts_patch---

```
pair = 0.0
Mpair = 1.0
env = 0.0
Menv = 2.019
cbeta = 0.0
Mcbeta = 0.5
Menv_non_helix = 2.019
Menv_termini = 2.019
Menv_tm_proj = 2.019
Mlipo = 1.0
```

--- score_membrane_s4.wts_patch---

```
pair = 0.0
Mpair = 1.0
env = 0.0
Menv = 2.019
cbeta = 0.0
Mcbeta = 2.5
Menv_non_helix = 2.019
Menv_termini = 2.019
Menv_tm_proj = 2.019
Mlipo = 1.0
```

--- super_quick_relax_patch---

```
atom_pair_constraint = 0.1
rdc = 0.1
```

--- membrane_highres_Menv_smooth.wts ---

```
# @file: membrane_highres_Menv_smooth
# @desc: All atom energy function for membrane proteins: combines Rosetta's
# all atom energy function with membrane environment and solvation from the
# lazaridis-karplus implicit membrane model.
# @note: continuous for minimization, deprecated - use mpframework instead
```

```
# @cite: Barth, 2007, PNAS
METHOD_WEIGHTS ref  0.16 1.7 -0.67 -0.81 0.63 -0.17 0.56 0.24 -0.65 -0.1 -0.34 -0.89 0.02 -0.97 -0.98
-0.37 -0.27 0.29 0.91 0.51
fa_atr 0.8
fa_rep 0.44
fa_sol 0.00
fa_intra_rep 0.004
fa_pair 0.49
fa_plane 0
fa_dun 0.56
fa_mbenv 0.3
fa_mbsolv 0.35
Menv_smooth 0.5
ref 1
hbond_lr_bb 1.17
hbond_sr_bb 1.17
hbond_bb_sc 2.34
hbond_sc 2.2
p_aa_pp 0.32
dslf_ss_dst 0.5
dslf_cs_ang 2
dslf_ss_dih 5
dslf_ca_dih 5
pro_close 1.0
rama  0.2
omega  0.5
```

CHAPTER 5

Beyond PIRT: Using NMR to Illuminate Evidence for an Evolutionarily Conserved Mechanism for TRPV1 Thermosensing[†]

[†]This chapter contains data and writing that will be included in a manuscript to be published at a later date. The data and writing here represent my own contributions.

5.1 Introduction

While PIRT and TRPM8 has been the focus for the majority of this dissertation, PIRT also interacts and regulates the heat sensing TRPV1. This chapter focuses work that was done on the TRPV1 ligand sensing domain (hTRPV1-SD) using NMR.

TRPV1, from the vanilloid subfamily, is responsive to various chemical and physical stimuli including vanilloid ligands, elevated temperature, changes in physiological pH, endogenous lipids, calcium sensing proteins including calmodulin and S100A1, and small modulatory membrane proteins. [14, 90, 119-121] In group C unmyelinated neurons of the peripheral nervous system, TRPV1 has been shown to be integral to nociception. [122, 123] Alternative avenues in nociception therapy have become a significant societal issue with overdoses in 2015 from opiate-derived therapies becoming a leading cause of accidental death in in the United States, when adjusted for age.[124] As causes of death become available from the CDC for 2016 and 2017, the rate is likely to increase as many states declare opioid abuse to be an epidemic. Consequentially, there is interest in TRPV1 therapeutic intervention for various pain indications.[122] Beyond nociception, an increasing number of studies provide emerging evidence that TRPV1 is involved in diverse human physiology: deletion in mice exacerbates systemic inflammatory response syndrome, it modulates energy homeostasis and affects obesity, neuronal ablation of

TRPV1 mitigates inflammation to islet cells of Langerhans and destruction of β cells in type 1 diabetes, TRPV1 inhibition of calcitonin gene-regulated peptides (CGRP) enhances longevity associated with decreases in metabolic output, TRPV1 activation contributes to apoptosis in cancer treatment with respect to astrocytoma, and TRPV1 is involved in airway hypersensitivity and inflammation affecting asthma.[125-132]

Like TRPM8, described previously in this dissertation, we predict that the hTRPV1-SD contributes to TRPV1-dependent channel conductance based on research on capsaicin activated TRPV1 channel conductance thought to be driven by this domain.[133] Given the role of the TRPV1-SD in ligand activation and the structural similarity to voltage-sensing domains in VGICs, we propose that the TRPV1-SD contributes to the thermosensitivity of TRPV1.

The work here shows that NMR can be used to probe the temperature sensitivity of a structural domain in TRPV1. This data is the first to structurally and biophysically investigate the thermodynamic properties of thermosensitive TRP channels without the use of mutagenesis, where mutagenesis has resulted in conflicting results for TRP channels.[63, 134]

5.2 Materials and Methods

5.2.1 Growth, Purification, and Optimization

The growth, purification, and optimization of hTRPV1-SD follows a similar protocol as hPIRT described in Chapter 2. Briefly, the over expression hTRPV1-SD was carried out using pET16b transformed BL21 (DE3) cells and purified using a combination of a Ni-NTA affinity column chromatography and size exclusion purification protocols.

Membrane mimic optimization was carried out using several detergents with lyso-palmitoylphosphatidylglycerol (LPPG, Anatrace) showing the best spectra (Figure 5.1). The full purification protocol was optimized and carried out by Minjoo Kim, and will be presented in the corresponding manuscript.

5.2.2 Nuclear Magnetic Resonance Data Collection and Amino Acid Resonance Assignments

The backbone resonance assignment (Figure 5.1) of the hTRPV1-SD was carried out at 45 °C on a 900 μM uniformly ^{15}N, ^{13}C labeled sample in a Bruker shaped NMR tube (Part Number Z106898) with 4% D_2O (v/v). TROSY versions of HSQC, HNCA, HNCOCA, HNCO, HNCACO, HNCACB, and CBCACONH as well as 4D HNCACO and 4D HNCOCA experiments were utilized. Additionally, ^{15}N-edited HSQC-NOESY with a 90 ms mixing time (τ) was used for sequential assignments. Table 5.1 details specific experimental parameters.

The spectra were collected on an a Bruker Avance III HD 850 MHz ^{1}H spectrometer equipped with a 5 mm TCI Cryoprobe. The nonuniformly sampled data were reconstructed with qMDD[135] and processed in nmrPipe,[68] with analysis and resonance assignment carried out in the CcpNMR [42] software. The chemcial shift assignments at 45 °C were deposited in the Biological Magnetic Resonance Bank (BMRB entry 27029).

5.2.3 Secondary Structure Calculations and Analysis

Table 5.1 NMR Parameters Used for hTRPV1-SD Amino Acid Resonance Assignments

Experiment, (TROSY)	**Transients**	**F1 (direct)**		**F2 (indirect)**		**F3 (indirect)**		**F4**		**NUS %**
		Points	**SW (Hz)**	**Points**	**SW (Hz)**	**Points**	**SW (Hz)**	**Points**	**SW (HZ)**	
[^{15}N ^{1}H] HSQC	128	2048	10204	128	2843	N/A	N/A			0
HNCA	64	2048	10204	64	2197	128	5559			40
HNCOCA	64	2048	10204	64	2197	128	5559			40
HNCACB	128	2048	10204	64	2197	96	16038			35
CBCACONH	64	2048	10204	64	16039	128	2585			50
HNCO	16	2048	10204	64	2197	128	3427			45
HNCACO	32	2048	10204	64	2197	128	3849			50
HNCACO	16	2048	10204	40	2197	64	5559	40	3421	15
HNCOCA	16	2048	10204	32	2197	40	3421	64	5559	12.5
[^{15}N ^{1}H] HSQC NOESY	64	2048	10204	64	2197	128	10204			45

The secondary structure of the hTRPV1-SD was determined using TALOS-N.[33] From the output of TALOS-N, the secondary structure was plotted as secondary structure probability vs residue number (Figure 5.2).

5.2.4 Temperature Dependent Chemical Shift Perturbations

^{1}H-^{15}N TROSY-HSQC NMR studies of purified hTRPV1-SD were recorded from 15 °C to 50 °C, at 5 °C increments. The temperature for these experiments was calibrated using 99% ^{2}H methanol where the difference in chemical shifts (ppm) arising from the two methanol resonances is used as a temperature standard according to $T[K] = 419.1381 - 52.5130\Delta\delta - 16.7467(\Delta\delta)^2$. [136] These temperature dependent resonances were used to extract thermodynamic information according the methods describe in Chapter 1 relating resonance intensities to enthalpy and T_{50} (T_m).

$$I = 1 + \frac{\left(I_{active} + I_{resting}\right) e^{\left(-\frac{\Delta H}{R}\left(\frac{1}{T}-\frac{1}{T_m}\right)\right)}}{1 + e^{\left(-\frac{\Delta H}{R}\left(\frac{1}{T}-\frac{1}{T_m}\right)\right)}}$$

From this equation, the enthalpies of 66 residues for WT hTRPV1-SD and 52 residues for Arg557Ala-hTRPV1-SD were obtained. From the enthalpies, a histogram with bins of 5 kcal/mol was fit to a Gaussian function, $f(\Delta H) = a_{max}\, exp\left(-\frac{(\Delta H-\mu)^2}{2\sigma^2}\right)$, for both WT- and Arg557Ala-hTRPV1-SD, where μ and σ are the ensemble average enthalpy and standard deviation respectively.

5.2.5 <u>T</u>ROSY for <u>R</u>otational <u>C</u>orrelation <u>T</u>imes (TRACT)

The manuscript that will be submitted will contain information on distances derived from paramagnetic relaxation enhancement (PRE) data. To accurately quantify the PRE-derived distances between individual indole amine (Trp549 and Trp427) residues and the MTSL-labeled Cys443, accurate rotational correlation times (τ_c) are needed at 20 °C and 50 °C.

The amide cross-correlation between the chemical shift anisotropy (CSA) and dipole-dipole (DD) relaxation can be used to estimate the correlation time (τ_c) of a protein. With an assumption that the N-H bond and its ^{15}N chemical shift tensor is axially symmetric with and angle θ, the relaxation rates for the (TROSY, R_α) α-spin state and (anti-TROSY, R_β:) β-spin state are:

$$R_\alpha = \lambda - \eta_{xy} + R_H + R_{CS}$$

$$R_\beta = \lambda + \eta_{xy} + R_H + R_{CS}$$

where λ is the auto-relaxation rate, R_{CS} is the relaxation rate from the chemical exchange contribution, and R_H is the relaxation ray due to the DD coupling with remote protons. η_{xy} is the transverse cross-correlated relaxation rate and can be calculated as:[137-140]

$$R_\beta - R_\alpha = 2\eta_{xy} = 2p\delta_N(4J(0) + 3J(\omega_N))(3\cos^2\theta - 1)$$

where p is the DD coupling between an amide ^{1}H and ^{15}N,

$$p = \frac{\mu_0 \gamma_H \gamma_N h}{16\pi^2\sqrt{2r_{HN}^3}}$$

and δ_N is the CSA of the ^{15}N nucleus,

$$\delta_N = \frac{\gamma_N B_0 \Delta\delta_N}{3\sqrt{2}}$$

where γ_N and γ_H are the gyromagnetic ratios of the ^{1}H and ^{15}N respectively, *h* is the Plank constant, r_{HN} is the internuclear H-N distance, μ_0 is the vacuum permeability constant, $\Delta\delta_N$ is the difference between the two principle component axis of the ^{15}N chemical shift tensor, and the J(ω) term is the spectral density function at frequency ω given by:

$$J(\omega) = \frac{0.4\tau_c}{[1 + (\tau_c\omega)^2]}$$

As the above formulae show, the rotational correlation time is contained with the spectral density function and can be calculated by measuring the relaxation rates for spin states α and β.

To determine accurate τ_c, [^{15}N, ^{1}H]-TRACT was collected at a time delay from τ = 0 ms to τ = 100 ms with 4 ms intervals. The pulse program that was used for these experiments was an adapted version published by Lee, D, et al. [141] The data were processed and integrated in nmrPipe over a range of 9.6 ppm to 10 ppm, to which a linear baseline correction was applied with the nmrPipe function *BASE* and a defined node list was applied to the noise. The range that was integrated was selected as it comprises the Trp549 indole amine resonance, and only this was integrated since integration over the

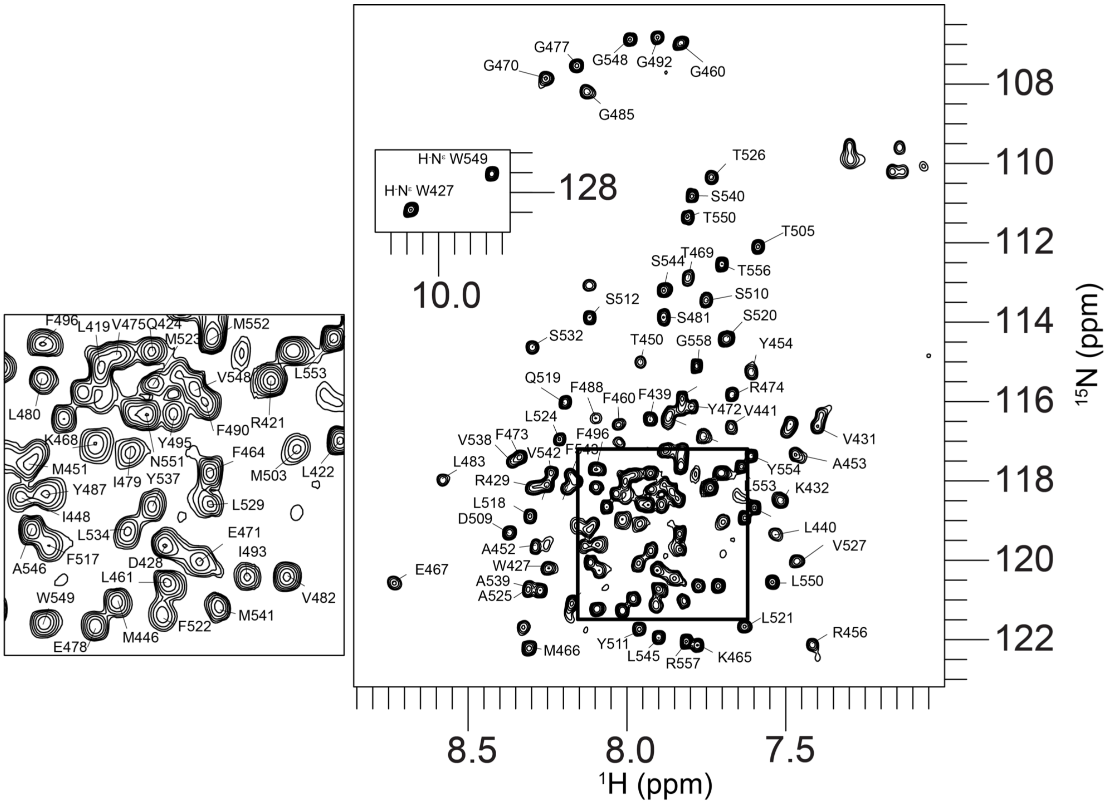

Figure 5.1 The hTRPV1-SD TROSY-HSQC. The spectrum from hTRPV1-SD shows highly resolved resonances for a membrane protein, which was used to make resonance assignments for further experimental analysis and structural calculations.

entire amino region may inflate the effective correlation time. [142] The integrated data was fit using *MATLAB R2015a*'s *nlinfit* handle with a monoexponential decay function, $f(t) = Ae^{-\beta t}$, where A is a maximum, t is the time delay, and β is the relaxation decay constant in Hz. The relaxation decays for the α and β state of exclusively the Trp549 indole amine resonance to mitigate exchange effects and the calculated τ_c is a lower limit of the effective rotational correlation time due to the rigid body assumption as described previously by Lee, D. et al. [141]

5.2.6 Calculation of Amide Proton Temperature Coefficients

The δ_{HN} chemical shift was calculated as the as $\delta_{HN} = \delta_{HN\,i} - \delta_{HN\,f}$ where the $\delta_{HN\,i}$ corresponds to the chemical shift at the given temperature (i) in the array from 288 K to 323 K and $\delta_{HN\,f}$ corresponds to the final temperature, 323 K. The derivative of the δ_{HN} with respect to the temperature (K) is the temperature coefficient ($\Delta\delta/\Delta T$ (ppb/K)). Calculation of $\Delta\delta/\Delta T$ was done for 66 residues in the WT-hTRPV1-SD and 52 residues for the Arg557Ala hTRPV1-SD mutant; it should that the assigned resonances correspond to the most resolved and well assigned residues in each of the spectra in the temperature titration. From the resonance positions, the difference in $\Delta\delta/\Delta T$ of the WT- and Arg557Ala-hTRPV1-SD was labeled as $\Delta\Delta\delta/\Delta T$ (ppb/K, not shown). A cutoff value of ±0.25 (ppb/K) was used to highlight residues with significant differences in flexibility between the hTRPV1-SD and Arg557Ala mutant as noted from amide proton temperature coefficient analysis.[143]

5.3 Results

5.3.1 TRPV1 Ligand-sensing Domain Solution NMR Resonance Assignment

Chemical shift resonance assignments in Figure 5.1 and the resonance assignment strip plot Figure 5.2 show high quality NMR data with highly resolved resonances. From this data, 87% of the backbone was assigned.

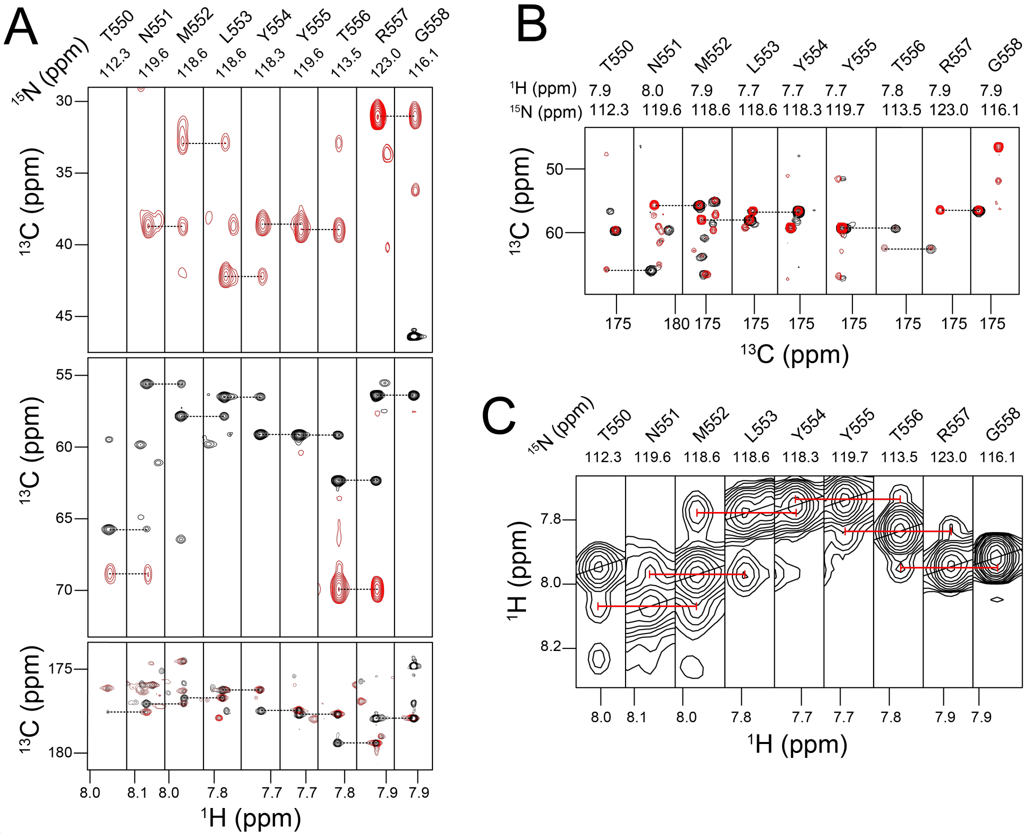

Figure 5.2 The hTRPV1-SD assignment strip. A) Backbone resonance assignment of T550 to G558 in S4 helix, shown with HNCA (black) and HNCACB (red), 4D HNCACO (B, black), 4D HNCOCA (B, red), and 15N-edited NOESY-TROSY C.

5.3.2 Secondary Structure of the hTRPV1-SD at Elevated Temperature

The secondary structure of the hTRPV1-SD was determined from experimental backbone chemical shift data analyzed in TALOS-N.[33] The per residue secondary structure probability of hTRPV1-SD is shown in Figure 5.3. The data suggest a transmembrane α-helix topology for the isolated hTRPV1-SD that is consistent with that determined from the cryo-EM TRPV1 structures.

5.3.3 The hTRPV1-SD Undergoes Reversible Temperature-dependent Conformational Change

In addition to functioning as a vanilloid receptor, TRPV1 functions as a heat sensor, a characteristic where the open probability of the ion channel increases with elevated temperature. Electrophysiology data from a number of groups suggest that the mid-point of temperature activation (T_{50}) is ~40-50 °C. [144-146] These previous studies also suggest that TRPV1 at 20 °C and 50 °C resides predominantly in resting (closed) and activated (open) states, respectively. To investigate a potential role of the hTRPV1-SD in thermosensitivity, NMR, and CD spectra were recorded at different temperatures (20 °C and 50 °C) that would be expected to correspond to distinct conformational states (Figure 5.3). Solution NMR is particularly well suited for temperature-dependent mechanistic biomolecular studies in that it provides atomic level information across a wide range of temperatures. The ^{1}H-^{15}N TROSY-HSQC NMR spectra of hTRPV1-SD at these two temperatures provide qualitative insight into the temperature sensitivity of this domain. First, from the proton dimension dispersion and the resonance resolution, the data are consistent with the hTRPV1-SD remaining folded over this temperature range. Second, there is significant temperature dependent chemical shift perturbation between the spectra

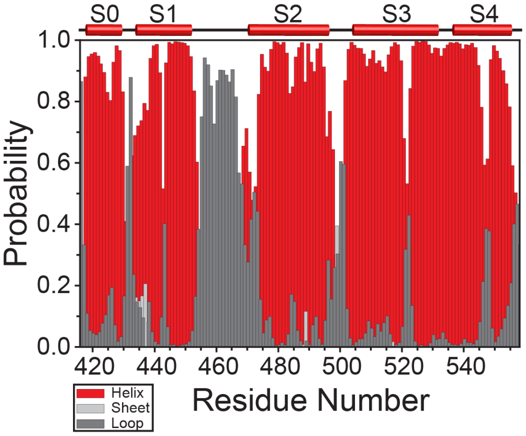

Figure 5.3 Secondary structure analysis from TALOS-N. The secondary structure prediction from assigned backbone resonances were computed using TALOS-N corresponding to four transmembrane α-helices and 1 pre transmembrane α-helix.

at 20 °C and 50 °C, which is consistent with a potential temperature-induced conformational change. Third, the temperature dependent spectral changes are completely reversible (data not shown). Additionally, CD data are consistent with the hTRPV1-SD temperature dependent change which is also reversible (data not shown). It

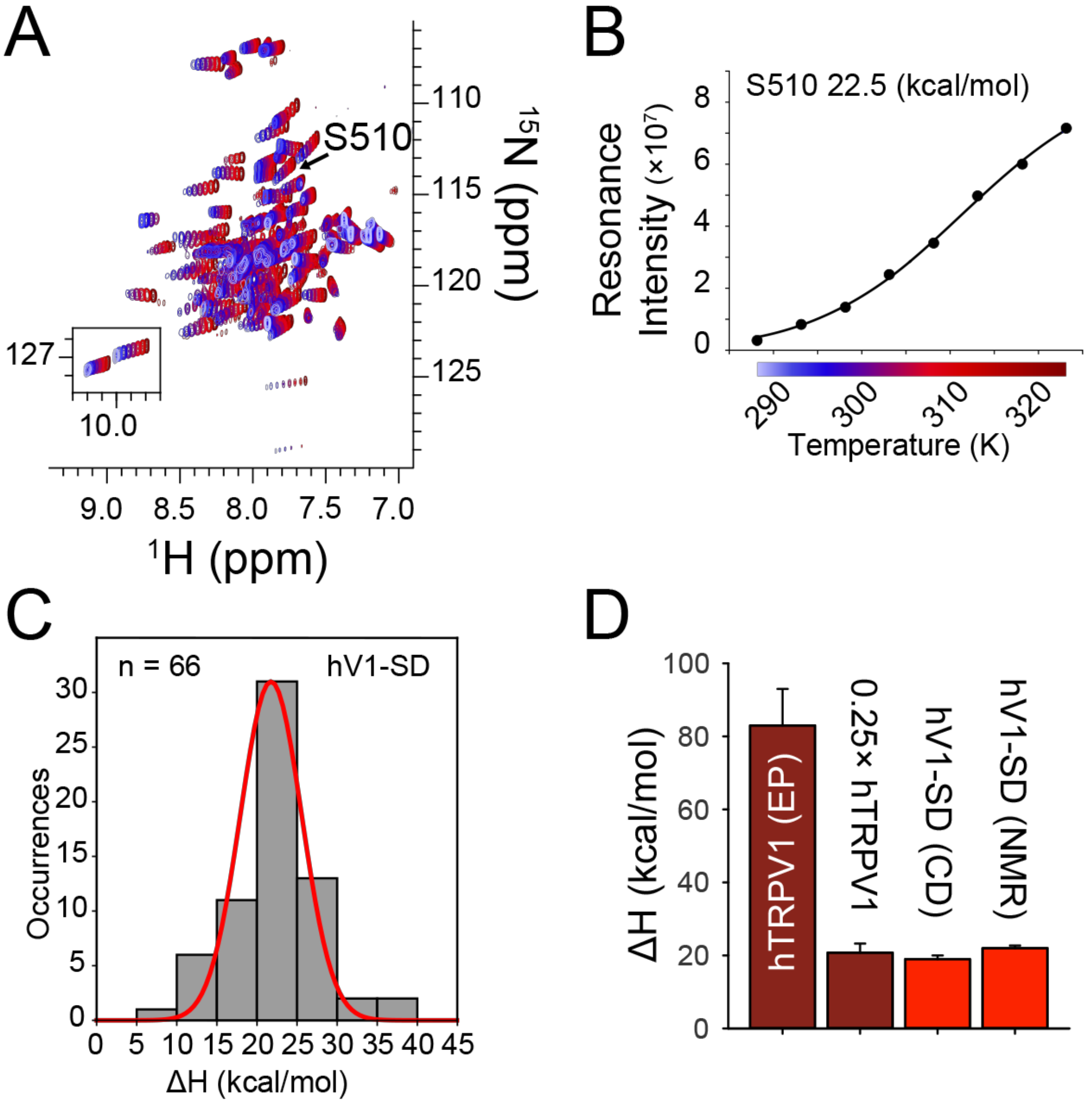

Figure 5.4Thermodynamic analyses from a temperature sensitive protein. Individual NMR resonance intensity changes from (A) as a function of temperature and fit to a modified van't Hoff model (B). The average enthalpy (C) from NMR intensity fits over the ensemble of the amino acid intensities agree with enthalpy from electrophysiology and circular dichroism (D); error bars are standard errors of the mean.

is notable that the hTRPV1-SD CD spectra maintain significant α-helical spectral features throughout the temperature change. The reversibility of the NMR and CD spectra indicate that the system is suitable for thermodynamic investigations into hTRPV1-SD thermosensitivity and the spectra quality indicate that the isolated sensing-domain remains folded in this temperature range.

5.3.4 hTRPV1-SD Resonance Intensities Were Used to Investigate the Thermodynamics

The resonance intensities measured from the temperature titration was used to extract the enthalpy of the transition from activated to inactivated states. In Figure 5.3A, we used NMR to measure TROSY-HSQC's at temperatures from 15-50 °C. With the assignments of these amino acids, Figure 5.3B, we observed that the intensity changes followed a sigmoidal trend that we fit to the modified van't Hoff described in the methods. With this in mind, we measured the intensities of 66 amino acid resonances and fit each of these resonance intensities to the same sigmoidal function, which when grouped in a histogram displays a well-defined Gaussian shape suggestive that the ensemble average of the domain contributes to the overall enthalpy (Figure 5.3C). The average ΔH correlates well to the measurements (Figure 5.3D) from circular dichroism on the same protein and from full length TRPV1 in electrophysiology studies that measure the conductance from TRPV1 currents.

5.3.5 [^{15}N, ^{1}H]-TRACT (TROSY for rotational correlation times) Measurements for Accurate Paramagnetic Relaxation Enhancement Measurements

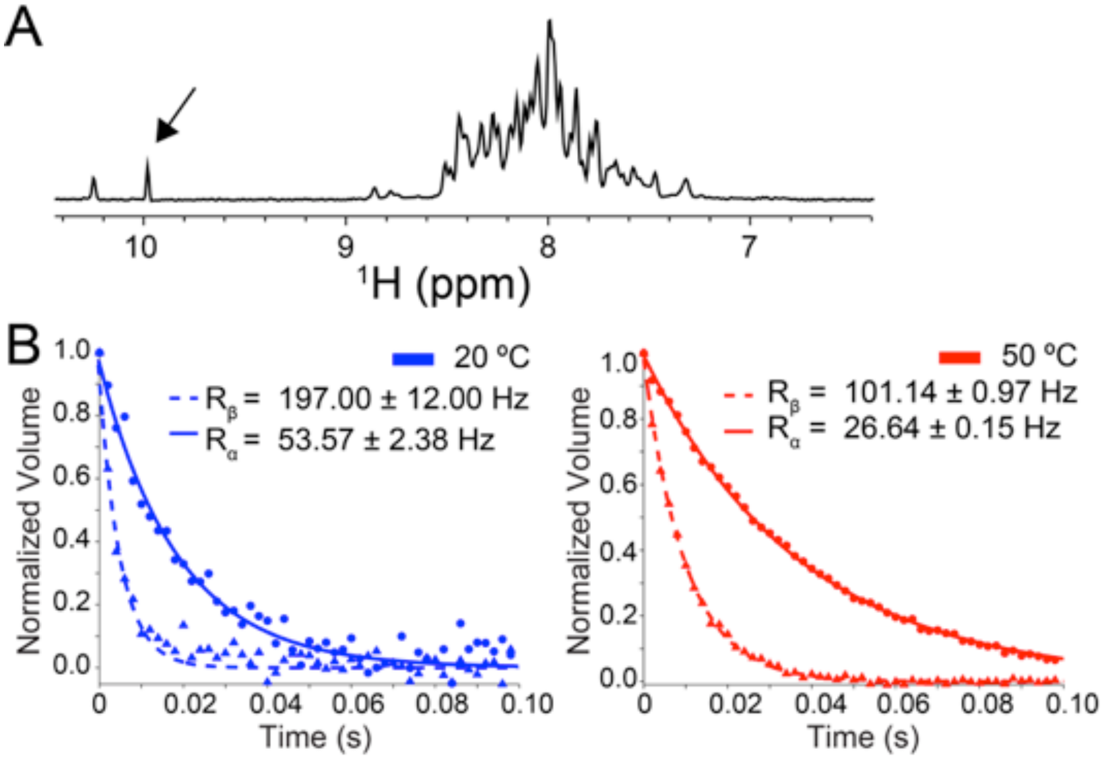

Figure 5.5 Determining the effective hTRPV1-SD rotational correlation time by NMR TRACT experiment. τ_c was measured at both 20 °C and 50 °C from TRACT measurements which utilize the relaxation rate difference between TROSY and Anti-TROSY 1H-15N correlated resonances. The indole amine from the S4 helix residue W549, highlighted with an arrow in (A), was used for analysis in this experiment due to potential artifacts that can arise from dynamic regions in the protein. In (B), the relaxation rates for both states, TROSY and Anti-TROSY, of the amides are fit to a monoexponential decay from which the rates are used in subsequent calculations relating the difference between these two states to the τ_c. (see Methods for additional information).

The rotational correlation (τ_c) time of a protein is required for accurate PRE distance measurements and is temperature dependent. The hTRPV1-SD effective τ_c was directly measured at each temperature using [^{15}N, ^{1}H]-TRACT (TROSY for rotational correlation times) NMR experiments. [141] With only the Trp549 (in the S4 helix) (Figure 5.4A) tryptophan indole amine (a non-exchanging amine) resonance, the hTRPV1-SD rotational correlation times at 20 °C and 50 °C (Figure 5.4B) were calculated to be 49 ± 3 ns and 25.6 ± 0.1 ns, respectively.

In the final manuscript, we use PRE-measurements to model a transition from one state to a second state with conformational change with temperature dependent mechanism.

5.3.6 Arg557Ala mutation affects the thermodynamics of the TRPV1 ligand-sensing domain.

It has been hypothesized that a change in residue heat capacity could drive the gating or activation of the channel caused by solvent exposure from a buried amino acid side chain.[147] In the full manuscript, we used evidence from NOESY data to show that Arg557 becomes more solvent exposed at high temperatures. Mutating Arg557 to Ala reduced this solvent exposure.

The Arg557Ala mutation caused a temperature dependent resonance intensity change similar to that of the WT. Because of differences between WT and mutant spectra, only 52 distinct resonances were used in the analysis. The representative plot of Ser512 in Figure 5.3B exhibits a sigmoidal shape consistent with a two-state conformational change analogous to WT hTRPV1-SD. Detailed analysis of the resonances (including Ser 512) for the Arg557Ala hTRPV1-SD show an average enthalpy (not shown) with a slightly decreased magnitude of 20.9 ± 0.9 kcal/mol and a T_{50} value of 45 ± 3 °C, which is significantly shifted relative to the WT protein.

5.3.6 Temperature Coefficients for the Mutant Arg557Ala Indicate Allosteric Effects to Protein Dynamics

It is well established that there is a temperature dependence on the amide chemical shift in proteins called the temperature coefficient, $\Delta\delta/\Delta T$. The amide chemical shift $\Delta\delta/\Delta T$ is sensitive to hydrogen bond formation as well as temperature dependent loss of structure from thermal expansion and this change in chemical shift as a function of temperature is discrete for individual amino acids.[37, 143] The $\Delta\delta/\Delta T$ deviates from linearity more or less in magnitude depending on the population of states the protein is dynamically sampling. Indeed, the $\Delta\delta/\Delta T$ is a rich source of global and local stability and the nonlinearity of $\Delta\delta/\Delta T$ can be used to inform on atomically explicit local dynamics reflective of fast exchange with ground state and a less populated states. [143, 148, 149]

The hTRPV1-SD structural dynamics between the WT and Arg557Ala were analyzed using the difference in amide proton temperature coefficients ($\Delta\Delta\delta/\Delta T$). The $\Delta\Delta\delta/\Delta T$ data suggests that there are allosteric effects that correspond to gain and loss of structure dispersed across the ligand-sensing domain. Amino acid residues Phe473, Tyr487, and Ser510 show a large positive $\Delta\Delta\delta/\Delta T$ value and residues Ala452, Asp471, and Thr526 show a large change of ± 0.25 ppb/K.

5.4 Discussion

The data shown in this dissertation will be published alongside other biochemical and structural data showing outcomes of the ligand binding studies that indicate that probing the thermodynamics of the hTRPV1-SD and temperature dependent effects of this domain show new insight into TRPV1 thermosensitivity. Our approach to investigate the thermosensitivity of TRPV1 makes use of an isolated and evolutionarily conserved structural domain probed by established solution NMR and far-UV CD methods.

The NMR spectra from hTRPV1-SD show well-structured spectra with uniform resonance intensities and good chemical shift dispersion. The quality of the spectra allowed for chemical shift assignments for 87% of the amino acid resonances. From the resonance assignments, we were able to extract enthalpy from resonance intensities that correlate with other experiments on hTRPV1-SD and the full-length channel. This suggests that the observed state change from the NMR measurements are consistent with other techniques and we show the first evidence of an isolated temperature sensitive domain in TRPV1.

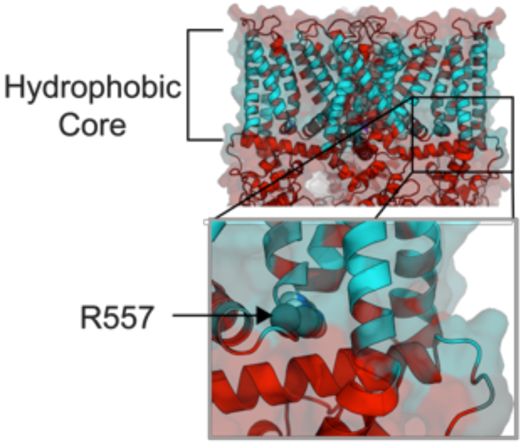

Figure 5.6 The Arg557 becomes more solvent exposed with higher temperature. We propose that the buried Arg557 becomes solvent exposed at higher temperatures by translation of the S4 α-helix.

The data presented herein will be useful in explaining the mechanism of temperature regulation and activation with TRP channels in general. The current mechanistic hypothesis suggests that exposure of hydrophilic residues to solvent leads to a positive heat capacity change that can drive the channel to open (Figure5.5). A putative mechanism leading to Arg557 exposure could be movement intracellularly of the S4 α-helix or a possible 3_{10} to α-helix transition that would effectively lengthen the bottom portion of S4 and expose Arg557. The resting state of TRPV1 (PDB: 5IRZ) does show a 3_{10} helix in the intracellular side of S4[150], however it is still undetermined whether the SD from TRP channels in the vanilloid family transitions between states during the gating of the channel.

Our data support the general observation that the sensing domain contains portions of the molecular determinants that gate the full channel, but additional evidence is needed to make these hypotheses conclusive. For example, PRE or residual dipolar coupling measurements at different temperatures could be modeled to show the transition from active state hTRPV1-SD to inactive state.

5.5 Supplemental Information

5.5.1 MATLAB and Shell Scripts

-- TRACT Analysis ---

```
%WVH 20141126 original

% NS modified

%
%TRACT NMR ANALYSIS (REF1)


disp('Program to analyze TRACT DATA--WVH & NS 2014')
disp('This program has been modified to only ask for the decay constant from fitting data, which should be in Hz if plotted as a function of seconds and not milliseconds' )
disp(' ')
%
%________________________________INPUTS______________________________________
B0_MHz=input('What is the field strength that the experiments were run at (MHz):  ');
Ra=input('What is the decay constant alpha in Hz');
Rb=input('What is the decay constant beta in Hz (hint, it should be a larger value)');
disp(' ')
B0_MHz;
B0=0.0235*B0_MHz;

RbRa=Rb-Ra;
%_______________________________CONSTANTS______________________________
```

```
mu0=4*pi*1E-7;           %vacuum permeability, magnetic constant (Newton/(Amp*Amp))
GamH=42.576*2*pi*1E6;  %1H Gyromagnetic Ratio (rad/(sec*Tesla)
GamN=-4.3156*2*pi*1E6; %15N Gyromagnetic Ratio (rad/(sec*Tesla)
h=6.6206957E-34;          %Plank's constant (m^2kg/s)
rNH=1.02*0.0000000001;     %Radius of NH bond, in meters) (1.02 Angstroms) REF2
DeldelN=0.00016;          %160ppm
p=(mu0*GamH*GamN*h)/(16*(pi^2)*sqrt(2)*(rNH^3));
%p is the DD coupling between 1H and 15N of the 15N-1H moiety
delN=GamN*B0*DeldelN/(3*sqrt(2));      %CSA of the 15N nucleus
Radian=degtorad(17);                  %theta=17 degrees REF3

%______________FIT for Rotational Correlation Time____________________

g = @(f) (2*p*delN*(4*0.4*f+3*0.4*f/(1+(f*GamN*B0)^2))*(3*cos(Radian)^2-1))-RbRa;
tau = lsqnonlin(g,5); %NS suggests nonlinear least squares fitting
tc = tau*1E9;        %Scale tc from seconds to nanoseconds

disp(['The alpha state relaxation rate is ', num2str(Ra),' Hz'])
disp(['The beta state relaxation rate is ', num2str(Rb),' Hz'])
disp(['Rb-Ra = ',num2str(RbRa),'Hz'])

disp(' ')
disp(['For a field strength of ',num2str(B0), ' Tesla,'])
disp(['the rotational correlation time is ',num2str(tc), ' ns'])

%REF1:D. Lee, C. Hilty, G. Wider, K. Wuthrich, Effective rotational correlation times of proteins from
NMR relaxation interference, J. Mag. Reson. 178(2006) 72-76

%REF2: J.E. Roberts, G.S. Harbison, M.G. Munowitz, J. Herzfeld, R.G. Griffin, Measurement of
heteronuclear bond distances in polycrystalline solids by solid-State NMR Techniques, J. Am. Chem. Soc.
109 (1987) 4163ñ4169.

%REF3: D. Fushman, N. Tjandra, D. Cowburn, Direct measurement of 15N chemical shift anisotropy in
solution, J. Am. Chem. Soc. 120 (1998) 10947 10952.
```

--- Thermodynamic Fitting to HSQC Intensities ---

```
clear all
clc
close all

warning('off')
files=dir('*.txt');
j=readtable(files(1).name,'Delimiter','\t');
n=size(files);

t=[15 20 25 30 35 40 45 50];
r = 1.9872036E-3;

% fit=@(b,x) 1+(b(1)-b(2))*exp(b(3)./(r.*x).*(x./b(4)-1))./(1+exp(b(3)./(r*x).*(x./b(4)-1)));
fit=@(b,x) -b(1).*x+b(2);
xf=linspace(min(t),max(t))+273.15;
figure(1)
```

```
for i=1:n(1);
    hold on
    tmp=readtable(files(i).name,'Delimiter','\t');
    a=tmp.Height;
    [xData yData]=prepareCurveData(1./(t+273.15),log(a));
    beta = nlinfit(xData,yData,fit,[ 0 0]);
    plot(xData,yData,'o',1./xf,fit(beta,1./xf))
    delh(:,i)=beta(1)*r;
    dels(:,i)=beta(2)*r;
end
xlabel('1/T (K)')
ylabel('ln(Intensity)')
title('vant Hoff Plot')
figure(2)
H=histogram(delh)
H.BinWidth=2.5;
xlabel('\Delta H (kcal/mol)')
ylabel('Occurances')
title('Enthalpy')
xlim([0,50])

figure(3)
% histogram(dels*1000)
H=histogram(dels*1000)
H.BinWidth=5;
xlabel('\DeltaS (Cal/mol/K)')
ylabel('Occurances')
title('Entropy')

%%
for i=1:n(1);
    hold on
    tmp=readtable(files(i).name,'Delimiter','\t');
    a=tmp.Height;
    b(:,i)=a;
    [xData yData]=prepareCurveData(t+273.15,a);
    [deltaH,Tm,beta]=NMR_intensity_fit(t+273.15,a);
    plot(xData,a,'o', xfit2,fit(beta,xfit2));
    delh(:,i)=deltaH;
    tm(:,i)=Tm;
end
xlabel('T (K)')
ylabel('NMR Intensities')

%%

Delta_H=delh;
clear fit
a=length(find(Delta_H>5 & Delta_H<10));
b=length(find(Delta_H>10 & Delta_H<15));
c=length(find(Delta_H>15 & Delta_H<20));
d=length(find(Delta_H>20 & Delta_H<25));
e=length(find(Delta_H>25 & Delta_H<30));
f=length(find(Delta_H>30 & Delta_H<35));
g=length(find(Delta_H>35 & Delta_H<40));
```

```
h=length(find(Delta_H>40 & Delta_H<45));
x=linspace(0,45,10)+2.5;
y=[0 a b c d e f g h 0];
rng default
figure(99)
hold on
[xData yData]=prepareCurveData(x,y);
f=fit(xData,yData,'gauss1');
fit=@(g,x) g(1).*exp(-((x-g(2))./g(3)).^2);
beta0=[f.a1 f.b1 f.c1];
[beta,R,J,CovB,MSE]=nlinfit(xData,yData,fit,beta0);
% standev=sqrt(diag(CovB)); %no
standev=beta(3); %yes
SEM=standev/sqrt(n(1));
SSresidual=sum(R.^2);
SStotal=sum((y-mean(y)).^2);
rsquare=1-(SSresidual/SStotal);
bar(x,y,1);
p=plot(f);
legend([p],['\Delta H =  ' sprintf('%.2f',beta(2)) '  \pm  ' sprintf('%.2f',SEM) ' kcal/mol ' ],'Location','Best');
xlabel('\DeltaH (kcal/mol)')
ylabel('Occurences')
set(gca,'TickDir','out')
% print('-painters','-deps','histogram_fit_delta_H_v2')
% print -painters -dpdf -r800 histogram_fit_delta_H_v2.eps
```

---NEEDS---
#The above script needs a function named NMR_intesity_fit.m

```
function [ deltaH, Tm,beta ] = NMR_intensity_fit( temp,intensity )
%Delta H extraction from NMR intensities
%   This is a script that uses a modified Van't Hoft equation to extract thermodynamic values from NMR
intensities from a TROSY-HSQC. Thetemperature data must be in Kelvin scale.

% r is equal to 1.9872036E-3 kcal/mol
% The initial guess for the Delta H is 10 kcal/mol
% The initial guess for the Tm is 300 K
% Initial guesses for the max and minimum are defined from the input data
% as the max and min of the input

[xData, yData]=prepareCurveData(temp,intensity);

r = 1.9872036E-3;

fit=@(b,x) 1+(b(1)-b(2))*exp(b(3)./(r.*x).*(x./b(4)-1))./(1+exp(b(3)./(r*x).*(x./b(4)-1)));

beta0=[max(yData) min(yData) 10 300];


[beta,R,J,CovB,MSE]=nlinfit(xData,yData,fit,beta0);
```

```
deltaH = beta(3);
Tm = beta(4);

end
```

--- TRACT Spectral Integration and Analysis ---

```
#!/bin/csh



## tauList is the array number for the interleaved spectra.
set tauList = (1 2 3 4 5 6 7 8 9 10 11 12 13 14 15 16 17 18 19 20 21 22 23 24 25 26 27 28 29 30 31 32 33
34 35 36 37 38 39 40 41 42 43 44 45 46 47 48 49 50 51 52 53 54 55 56 57 58 59 60 61 62 63 64 65 66 67
68 69 70 71 72 73 74 75 76 77 78 79 80 81 82 83 84 85 86 87 88 89 90 91 92 93 94 95 96 97 98 99 100)

# Processing functions specific for nmrPipe processing
set nodelist = ( 5ppm )

set lbHz    =  1.0
set p0      =  65.0
set p1      =  0.0
set c       =  0.5

set extX1   = 12ppm
set extXN   = 6ppm
set integX1 = 8.5ppm
set integXN = 7.6ppm
set noiseX1 = 6ppm
set noiseXN = 5ppm

#
#----------------Normal-Proc----------------------------------------

nmrPipe -in test.fid \
| nmrPipe -fn POLY -time                              \
#| nmrPipe  -fn EM -lb $lbHz -c $c                    \
| nmrPipe  -fn SP -off 0.5 -end 0.98 -pow 2 -c 0.5     \
| nmrPipe  -fn ZF  -zf 4 -auto                        \
| nmrPipe  -fn FT                                 \
#| nmrPipe -fn BASE -first -last -nl $extX1 $extXN -nw 3      \
| nmrPipe -fn BASE -nl $nodelist                      \
| nmrPipe  -fn EXT -x1 $extX1 -xn $extXN -sw -verb    \
| nmrPipe  -fn PS -p0 $p0 -p1 $p1 -di                 \
#| nmrPipe  -fn POLY -auto -ord 1                         \
   -verb -ov -out test.ft1

#----------------------Integration---------------------------------

nmrPipe -in test.fid \
| nmrPipe  -fn EM -lb $lbHz -c $c                     \
| nmrPipe  -fn ZF  -zf 4 -auto                        \
| nmrPipe  -fn FT                                 \
```

```
#| nmrPipe -fn BASE -first -last -nl $extX1 $extXN -nw 3      \
| nmrPipe -fn BASE -nl $nodelist                        \
| nmrPipe  -fn EXT -x1 $integX1 -xn $integXN -sw -verb    \
| nmrPipe  -fn PS -p0 $p0 -p1 $p1 -di                \
#| nmrPipe  -fn POLY -auto -ord 2                          \
| nmrPipe  -fn INTEG -x1 $integX1 -xn $integXN               \
   -verb -ov -out integrals.ft1

#Convert the integrated spectrum to txt file.
pipe2txt.tcl integrals.ft1 > integrals.txt

readROI -in test.ft1 -ndim 2 -out None -vec vRMS -noverb -silent \
        -x X_AXIS $noiseX1 $noiseXN -y Y_AXIS 0% 100% > noise.txt

echo "Created test.ft1 Noise: `cat noise.txt`"

split2D.com -in test.ft1 -outDir ft -outName test%03d.ft1 -tau $tauList

if (-e tau.list) then
   /bin/rm tau.list
endif

foreach f (ft/test*.ft1)
   set tau = (`getParm -in $f -parm FDTAU`)

   echo $f $tau
   echo $tau >> tau.list
end
```

CHAPTER 6

Conclusions and Future Work

The work in this dissertation advances understanding in function and regulation of TRP channels through investigations using NMR, MST, biochemistry, and computation. Biological temperature sensation is complex without a clear mechanism of action. TRP channels–with TRPM8 and TRPV1 as the cold and hot sensors, respectively–are equally confounding. Despite active research in trying to understand how these two proteins function, the exact mechanism driving temperature sensation is unknown.

In Chapter 1, the mechanism of action for voltage-gated ion channels was discussed and from this the evolutionarily conserved α-helical bundle that makes up the sensing domain (SD) was proposed as the switch that drives gating in these TRP channels. This arose, not only from an evolutionary standpoint, but also from data showing that ligand binding can drive these channels to open such that menthol and capsaicin are thought to bind to SD of TRPM8 and TRPV1.[66, 103, 151, 152] TRPM8 and TRPV1 are both polymodally modulated through the activation by multiple stimuli, including the membrane protein PIRT.[11, 14, 16, 17, 61, 62, 65] By investigating how the SD is regulated and activated, it was hoped that a temperature sensing mechanism will arise.

In this Chapter 2, the human TRPM8-SD was investigated with new evidence that a modulatory protein named hPIRT controls access of PIP_2 to the hTRPM8 tetramer by competitively binding the SD. Furthermore, from evidence that calmodulin regulates TRPM8 and TRPV1, and that calmodulin is highly involved in PIP_2 regulation,[10, 22, 27, 90, 153] a predicted calmodulin binding site in hPIRT was tested with MST and NMR in Chapter 3. The mechanism of action for hPIRT investigation suggested here integrates how calmodulin downregulates hTRPM8 by sequestering Ca^{2+} and how hPIRT regulates hTRPM8 by shuttling PIP_2 to the hTRPM8 tetramer. More research will be needed to investigate exactly how calmodulin and hPIRT work together to regulate hTRPM8, and possibly other TRP channels.

In Chapter 4, an hPIRT structure was predicted by combining Rosetta applications and using sparse experimental restraints. This structure was used to highlight regions of hPIRT that bind to PIP_2 and hTRPM8-SD. This structure helps explain how PIP_2 might be shuttled to two PIP_2 binding sites in TRPM8, and potentially helps show how calmodulin proximity to the TRPM8-SD can sequester Ca^{2+}.

In Chapter 5, the structurally homologous heat sensing TRPV1 was investigated with NMR to quantify its temperature sensitivity. The isolated hTRPV1-SD function was quantified as approximately equal to ¼ of the overall tetramer in vivo. This was done by using NMR to assign the backbone amide resonances and then using those resonance identities to assign multiple spectra in a temperature array. From these spectra, the resonance properties were used to quantify thermodynamics and investigate its temperature sensitivity. The results show that NMR is a powerful tool to study challenging systems where measurements on both the resting and active state may be inaccessible. A similar investigation with TRPM8 may be challenging due to the inherent loss of signal and resolution in solution NMR with decreasing temperature. To measure the active state of TRPM8-SD the temperature likely needs to go below 10 °C as its half maximal temperature activation is ca. 18 °C.[103, 154] However, if the spectral quality from hTRPM8-SD are as high as hTRPV1-SD, then the active state would be accessible with NMR. Future studies on the hTRPV1-SD would benefit from fully assigned NOE distance restraints and residual dipolar couplings, which can be used for structural studies to determine a resting state structure using traditional approaches like Xplor-NIH. Combining these assignments and an NMR structure with NMR studies to measure dynamics such as Carr-Purcell-Meiboom-Gill (CPMG) could be used to understand the dynamics between the active and resting state.[155]

The data presented in this dissertation establishes new insight into TRP channel modulation. The isolated systems allowed for direct binding and functional investigations with NMR and MST. With NMR, amino acid specific information was gained providing evidence of hPIRT binding sites binds for PIP_2, TRPM8-SD, and calmodulin. Using state of the art Rosetta tools, the hPIRT structure was predicted and PIP_2 was docked with experimental guidance. Additionally, the temperature sensitivity of the TRPV1-SD was investigated with NMR providing a new route to investigate TRP channel mechanisms of regulation. All of these data increases our understanding of TRP channel modulations.

REFERENCES

1. Jensen, M.O., V. Jogini, D.W. Borhani, A.E. Leffler, R.O. Dror, and D.E. Shaw, Mechanism of voltage gating in potassium channels. *Science*, 2012. 336(6078): p. 229-33.

2. Proudfoot, C.J., E.M. Garry, D.F. Cottrell, R. Rosie, H. Anderson, D.C. Robertson, S.M. Fleetwood-Walker, and R. Mitchell, Analgesia mediated by the TRPM8 cold receptor in chronic neuropathic pain. *Curr. Biol.*, 2006. 16(16): p. 1591-605.

3. Tsavaler, L., M.H. Shapero, S. Morkowski, and R. Laus, Trp-p8, a novel prostate-specific gene, is up-regulated in prostate cancer and other malignancies and shares high homology with transient receptor potential calcium channel proteins. *Cancer Research*, 2001. 61(9): p. 3760-3769.

4. Zhang, L. and G.J. Barritt, Evidence that TRPM8 is an androgen-dependent Ca2+ channel required for the survival of prostate cancer cells. *Cancer Research*, 2004. 64(22): p. 8365-73.

5. Ma, S., H. Yu, Z. Zhao, Z. Luo, J. Chen, Y. Ni, R. Jin, L. Ma, P. Wang, Z. Zhu, L. Li, J. Zhong, D. Liu, B. Nilius, and Z. Zhu, Activation of the cold-sensing TRPM8 channel triggers UCP1-dependent thermogenesis and prevents obesity. *J. Mol. Cell Biol.*, 2012. 4(2): p. 88-96.

6. Rossi, H.L., A.C. Jenkins, J. Kaufman, I. Bhattacharyya, R.M. Caudle, and J.K. Neubert, Characterization of bilateral trigeminal constriction injury using an operant facial pain assay. *Neuroscience*, 2012. 224: p. 294-306.

7. Andersson, D.A., H.W.N. Chase, and S. Bevan, TRPM8 activation by menthol, icilin, and cold is differentially modulated by intracellular pH. *J Neurosci*, 2004. 24(23): p. 5364-5369.

8. Morenilla-Palao, C., M. Pertusa, V. Meseguer, H. Cabedo, and F. Viana, Lipid raft segregation modulates TRPM8 channel activity. *Journal of Biological Chemistry*, 2009. 284(14): p. 9215-24.

9. Liu, B. and F. Qin, Functional control of cold- and menthol-sensitive TRPM8 ion channels by phosphatidylinositol 4,5-bisphosphate. *J Neurosci*, 2005. 25(7): p. 1674-81.

10. Sarria, I., J. Ling, M.X. Zhu, and J.G. Gu, TRPM8 acute desensitization is mediated by calmodulin and requires PIP(2): distinction from tachyphylaxis. *J Neurophysiol*, 2011. 106(6): p. 3056-66.

11. Tang, Z.X., A. Kim, T. Masuch, K. Park, H.J. Weng, C. Wetzel, and X.Z. Dong, Pirt functions as an endogenous regulator of TRPM8. *Nature Communications*, 2013. 4.

12. Andersson, D.A., M. Nash, and S. Bevan, Modulation of the cold-activated channel TRPM8 by lysophospholipids and polyunsaturated fatty acids. *J Neurosci*, 2007. 27(12): p. 3347-55.

13. Vanden Abeele, F., A. Zholos, G. Bidaux, Y. Shuba, S. Thebault, B. Beck, M. Flourakis, Y. Panchin, R. Skryma, and N. Prevarskaya, Ca2+-independent phospholipase A2-dependent gating of TRPM8 by lysophospholipids. *Journal of Biological Chemistry*, 2006. 281(52): p. 40174-82.

14. Kim, A.Y., Z. Tang, Q. Liu, K.N. Patel, D. Maag, Y. Geng, and X. Dong, Pirt, a phosphoinositide-binding protein, functions as a regulatory subunit of TRPV1. *Cell*, 2008. 133(3): p. 475-85.

15. UniProt, C., UniProt: a hub for protein information. *Nucleic Acids Research*, 2015. 43(Database issue): p. D204-12.

16. Patel, K.N., Q. Liu, S. Meeker, B.J. Undem, and X. Dong, Pirt, a TRPV1 modulator, is required for histamine-dependent and -independent itch. *PLoS One*, 2011. 6(5): p. e20559.

17. Wang, C., Z. Wang, Y. Yang, C. Zhu, G. Wu, G. Yu, T. Jian, N. Yang, H. Shi, M. Tang, Q. He, L. Lan, Q. Liu, Y. Guan, X. Dong, J. Duan, and Z. Tang, Pirt contributes to uterine contraction-induced pain in mice. *Molecular Pain*, 2015. 11: p. 57.

18. Gao, X.F., J.F. Feng, W. Wang, Z.H. Xiang, X.J. Liu, C. Zhu, Z.X. Tang, X.Z. Dong, and C. He, Pirt reduces bladder overactivity by inhibiting purinergic receptor P2X3. *Nature Communications*, 2015. 6: p. 7650.

19. Guo, W., Q.Q. Sui, X.F. Gao, J.F. Feng, J. Zhu, C. He, G.E. Knight, G. Burnstock, and Z. Xiang, Co-localization of Pirt protein and P2X2 receptors in the mouse enteric nervous system. *Purinergic Signal*, 2016. 12(3): p. 489-96.

20. Cheng, H., X. Jiang, and X. Han, Alterations in lipid homeostasis of mouse dorsal root ganglia induced by apolipoprotein E deficiency: a shotgun lipidomics study. *Journal of Neurochemistry*, 2007. 101(1): p. 57-76.

21. Hansen, S.B., Lipid agonism: The PIP2 paradigm of ligand-gated ion channels. *Biochim. Biophys. Acta*, 2015. 1851(5): p. 620-8.

22. McLaughlin, S., J. Wang, A. Gambhir, and D. Murray, PIP(2) and proteins: interactions, organization, and information flow. *Annual Review of Biophysics and Biomolecular Structure*, 2002. 31: p. 151-75.

23. van den Bogaart, G., K. Meyenberg, H.J. Risselada, H. Amin, K.I. Willig, B.E. Hubrich, M. Dier, S.W. Hell, H. Grubmuller, U. Diederichsen, and R. Jahn,

Membrane protein sequestering by ionic protein-lipid interactions. *Nature*, 2011. 479(7374): p. 552-5.

24. Hansen, S.B., X. Tao, and R. MacKinnon, Structural basis of PIP2 activation of the classical inward rectifier K+ channel Kir2.2. *Nature*, 2011. 477(7365): p. 495-8.

25. Chen, L., Q. Zhang, Y. Qiu, Z. Li, Z. Chen, H. Jiang, Y. Li, and H. Yang, Migration of PIP2 lipids on voltage-gated potassium channel surface influences channel deactivation. *Sci Rep*, 2015. 5: p. 15079.

26. Brauchi, S., G. Orta, C. Mascayano, M. Salazar, N. Raddatz, H. Urbina, E. Rosenmann, F. Gonzalez-Nilo, and R. Latorre, Dissection of the components for PIP2 activation and thermosensation in TRP channels. *Proc. Natl. Acad. Sci.*, 2007. 104(24): p. 10246-51.

27. Gambhir, A., G. Hangyas-Mihalyne, I. Zaitseva, D.S. Cafiso, J. Wang, D. Murray, S.N. Pentyala, S.O. Smith, and S. McLaughlin, Electrostatic sequestration of PIP2 on phospholipid membranes by basic/aromatic regions of proteins. *Biophysical Journal*, 2004. 86(4): p. 2188-207.

28. Ufret-Vincenty, C.A., R.M. Klein, L. Hua, J. Angueyra, and S.E. Gordon, Localization of the PIP2 sensor of TRPV1 ion channels. *Journal of Biological Chemistry*, 2011. 286(11): p. 9688-98.

29. Hille, B., E.J. Dickson, M. Kruse, O. Vivas, and B.C. Suh, Phosphoinositides regulate ion channels. *Biochim Biophys Acta*, 2015. 1851(6): p. 844-56.

30. Han, B., K. He, C. Cai, Y. Tang, L. Yang, S.H. Heinemann, T. Hoshi, and S. Hou, Human EAG channels are directly modulated by PIP2 as revealed by electrophysiological and optical interference investigations. *Sci Rep*, 2016. 6: p. 23417.

31. She, J., J. Guo, Q. Chen, W. Zeng, Y. Jiang, and X.C. Bai, Structural insights into the voltage and phospholipid activation of the mammalian TPC1 channel. *Nature*, 2018.

32. Rohacs, T., C.M. Lopes, I. Michailidis, and D.E. Logothetis, PI(4,5)P2 regulates the activation and desensitization of TRPM8 channels through the TRP domain. *Nature Neuroscience*, 2005. 8(5): p. 626-34.

33. Shen, Y. and A. Bax, Protein structural information derived from NMR chemical shift with the neural network program TALOS-N. *Methods Mol Biol*, 2015. 1260: p. 17-32.

34. Williamson, M.P., Using chemical shift perturbation to characterise ligand binding. *Progress in Nuclear Magnetic Resonance Spectroscopy*, 2013. 73: p. 1-16.

35. Iwahara, J., C. Tang, and G. Marius Clore, Practical aspects of (1)H transverse paramagnetic relaxation enhancement measurements on macromolecules. *J Magn Reson*, 2007. 184(2): p. 185-95.

36. Bax, A., Weak alignment offers new NMR opportunities to study protein structure and dynamics. *Protein Sci*, 2003. 12(1): p. 1-16.

37. Hong, J., Q. Jing, and L. Yao, The protein amide (1)H(N) chemical shift temperature coefficient reflects thermal expansion of the N-H...O=C hydrogen bond. *J Biomol NMR*, 2013. 55(1): p. 71-8.

38. Lakomek, N.A., J.D. Kaufman, S.J. Stahl, J.M. Louis, A. Grishaev, P.T. Wingfield, and A. Bax, Internal dynamics of the homotrimeric HIV-1 viral coat protein gp41 on multiple time scales. *Angew Chem Int Ed Engl*, 2013. 52(14): p. 3911-5.

39. Cavanagh, J.F., W. J.; Palmer III, A. G.; Rance, M.; Skelton, N. J., *Protein NMR Spectroscopy: Principles and Practice (Second Edition)*. 2007: Elsevier Academic Press.

40. Cierpicki, T. and J.H. Bushweller, Charged gels as orienting media for measurement of residual dipolar couplings in soluble and integral membrane proteins. *J Am Chem Soc*, 2004. 126(49): p. 16259-66.

41. Fitzkee, N.C. and A. Bax, Facile measurement of (1)H-(1)5N residual dipolar couplings in larger perdeuterated proteins. *J Biomol NMR*, 2010. 48(2): p. 65-70.

42. Vranken, W.F., W. Boucher, T.J. Stevens, R.H. Fogh, A. Pajon, M. Llinas, E.L. Ulrich, J.L. Markley, J. Ionides, and E.D. Laue, The CCPN data model for NMR spectroscopy: development of a software pipeline. *Proteins*, 2005. 59(4): p. 687-96.

43. Bouty, E., CH. SORET. — Sur l'état d'équilibre que prend, au point de vue de sa concentration, une dissolution saline primitivement homogène, dont deux parties sont portées à des températures différentes; Archives de Genève, 3e periode, t. II, p. 48; 1879. *Journal de Physique Théorique et Appliquée*, 1880. 9(1): p. 331-332.

44. Jerabek-Willemsen, M., C.J. Wienken, D. Braun, P. Baaske, and S. Duhr, Molecular interaction studies using microscale thermophoresis. *Assay and Drug Development Technologies*, 2011. 9(4): p. 342-53.

45. Wienken, C.J., P. Baaske, U. Rothbauer, D. Braun, and S. Duhr, Protein-binding assays in biological liquids using microscale thermophoresis. *Nature Communications*, 2010. 1: p. 100.

46. Simons, K.T., C. Kooperberg, E. Huang, and D. Baker, Assembly of protein tertiary structures from fragments with similar local sequences using simulated annealing and Bayesian scoring functions. *J Mol Biol*, 1997. 268(1): p. 209-25.

47. Nguyen, E.D., C. Norn, T.M. Frimurer, and J. Meiler, Assessment and challenges of ligand docking into comparative models of G-protein coupled receptors. *PLoS One*, 2013. 8(7): p. e67302.

48. Kroncke, B.M., W.D. Van Horn, J. Smith, C. Kang, R.C. Welch, Y. Song, D.P. Nannemann, K.C. Taylor, N.J. Sisco, A.L. George, Jr., J. Meiler, C.G. Vanoye, and C.R. Sanders, Structural basis for KCNE3 modulation of potassium recycling in epithelia. *Science Advances*, 2016. 2(9): p. e1501228.

49. Mittendorf, K.F., B.M. Kroncke, J. Meiler, and C.R. Sanders, The homology model of PMP22 suggests mutations resulting in peripheral neuropathy disrupt transmembrane helix packing. *Biochemistry*, 2014. 53(39): p. 6139-41.

50. Song, Y., F. DiMaio, R.Y. Wang, D. Kim, C. Miles, T. Brunette, J. Thompson, and D. Baker, High-resolution comparative modeling with RosettaCM. *Structure*, 2013. 21(10): p. 1735-42.

51. DiMaio, F., A. Leaver-Fay, P. Bradley, D. Baker, and I. Andre, Modeling symmetric macromolecular structures in Rosetta3. *PLoS One*, 2011. 6(6): p. e20450.

52. Vernon, R., Y. Shen, D. Baker, and O.F. Lange, Improved chemical shift based fragment selection for CS-Rosetta using Rosetta3 fragment picker. *J Biomol NMR*, 2013. 57(2): p. 117-27.

53. Lange, O.F. and D. Baker, Resolution-adapted recombination of structural features significantly improves sampling in restraint-guided structure calculation. *Proteins: Structure, Function, and Bioinformatics*, 2012. 80(3): p. 884-895.

54. Rohl, C.A. and D. Baker, De Novo Determination of Protein Backbone Structure from Residual Dipolar Couplings Using Rosetta. *Journal of the American Chemical Society*, 2002. 124(11): p. 2723-2729.

55. Reichel, K., O. Fisette, T. Braun, O.F. Lange, G. Hummer, and L.V. Schafer, Systematic evaluation of CS-Rosetta for membrane protein structure prediction with sparse NOE restraints. *Proteins*, 2017. 85(5): p. 812-826.

56. Akimoto, M., Z. Zhang, S. Boulton, R. Selvaratnam, B. VanSchouwen, M. Gloyd, E.A. Accili, O.F. Lange, and G. Melacini, A mechanism for the auto-inhibition of hyperpolarization-activated cyclic nucleotide-gated (HCN) channel opening and its relief by cAMP. *J Biol Chem*, 2014. 289(32): p. 22205-20.

57. Alford, R.F., A. Leaver-Fay, J.R. Jeliazkov, M.J. O'Meara, F.P. DiMaio, H. Park, M.V. Shapovalov, P.D. Renfrew, V.K. Mulligan, K. Kappel, J.W. Labonte, M.S. Pacella, R. Bonneau, P. Bradley, R.L. Dunbrack, Jr., R. Das, D. Baker, B. Kuhlman, T. Kortemme, and J.J. Gray, The Rosetta All-Atom Energy Function for

Macromolecular Modeling and Design. *J Chem Theory Comput*, 2017. 13(6): p. 3031-3048.

58. Kim, D.E., D. Chivian, and D. Baker, Protein structure prediction and analysis using the Robetta server. *Nucleic Acids Research*, 2004. 32(Web Server issue): p. W526-31.

59. Simons, T.K., R. Bonneau, I. Ruczinski, and D. Baker, Ab initio protein structure prediction of CASP III targets using ROSETTA. *Proteins*, 1999. 37(3): p. 171-176.

60. Alford, R.F., J. Koehler Leman, B.D. Weitzner, A.M. Duran, D.C. Tilley, A. Elazar, and J.J. Gray, An Integrated Framework Advancing Membrane Protein Modeling and Design. *PLoS Comput Biol*, 2015. 11(9): p. e1004398.

61. Hilton, J.K., T. Salehpour, N.J. Sisco, P. Rath, and W.D. Van Horn, Phosphoinositide-interacting regulator of TRP (PIRT) has opposing effects on human and mouse TRPM8 ion channels. *Journal of Biological Chemistry*, 2018. 293(24): p. 9423-9434.

62. Tang, M., G.Y. Wu, X.Z. Dong, and Z.X. Tang, Phosphoinositide interacting regulator of TRP (Pirt) enhances TRPM8 channel activity in vitro via increasing channel conductance. *Acta Pharmacol Sin*, 2016. 37(1): p. 98-104.

63. Hilton, J.K., P. Rath, C.V. Helsell, O. Beckstein, and W.D. Van Horn, Understanding thermosensitive transient receptor potential channels as versatile polymodal cellular sensors. *Biochemistry*, 2015. 54(15): p. 2401-13.

64. Yin, Y., M. Wu, L. Zubcevic, W.F. Borschel, G.C. Lander, and S.Y. Lee, Structure of the cold- and menthol-sensing ion channel TRPM8. *Science*, 2018. 359(6372): p. 237-241.

65. Wang, C., L. Gu, Y. Ruan, T. Gegen, L. Yu, C. Zhu, Y. Yang, Y. Zhou, G. Yu, and Z. Tang, Pirt Together with TRPV1 Is Involved in the Regulation of Neuropathic Pain. *Neural Plasticity*, 2018. 2018: p. 4861491.

66. Rath, P., J.K. Hilton, N.J. Sisco, and W.D. Van Horn, Implications of Human Transient Receptor Potential Melastatin 8 (TRPM8) Channel Gating from Menthol Binding Studies of the Sensing Domain. *Biochemistry*, 2016. 55(1): p. 114-24.

67. Czisch, M. and R. Boelens, Sensitivity enhancement in the TROSY experiment. *Journal of Magnetic Resonance*, 1998. 134(1): p. 158-60.

68. Delaglio, F., S. Grzesiek, G.W. Vuister, G. Zhu, J. Pfeifer, and A. Bax, NMRPipe: a multidimensional spectral processing system based on UNIX pipes. *Journal of Biomolecular NMR*, 1995. 6(3): p. 277-93.

69. Kazimierczuk, K. and V.Y. Orekhov, Accelerated NMR spectroscopy by using compressed sensing. *Angew. Chem. Int. Ed.*, 2011. 50(24): p. 5556-9.

70. Shen, Y. and A. Bax, Protein backbone and sidechain torsion angles predicted from NMR chemical shifts using artificial neural networks. *Journal of Biomolecular NMR*, 2013. 56(3): p. 227-41.

71. Barrett, P.J., Y. Song, W.D. Van Horn, E.J. Hustedt, J.M. Schafer, A. Hadziselimovic, A.J. Beel, and C.R. Sanders, The amyloid precursor protein has a flexible transmembrane domain and binds cholesterol. *Science*, 2012. 336(6085): p. 1168-71.

72. Yarov-Yarovoy, V., J. Schonbrun, and D. Baker, Multipass membrane protein structure prediction using Rosetta. *Proteins*, 2006. 62(4): p. 1010-25.

73. Dragoni, I., E. Guida, and P. McIntyre, The cold and menthol receptor TRPM8 contains a functionally important double cysteine motif. *Journal of Biological Chemistry*, 2006. 281(49): p. 37353-60.

74. Lemmon, G. and J. Meiler, Rosetta Ligand docking with flexible XML protocols. *Methods in Molecular Biology*, 2012. 819: p. 143-55.

75. Miteva, M.A., F. Guyon, and P. Tuffery, Frog2: Efficient 3D conformation ensemble generator for small compounds. *Nucleic Acids Research*, 2010. 38(Web Server issue): p. W622-7.

76. Jones, D.T., Protein secondary structure prediction based on position-specific scoring matrices. *Journal of Molecular Biology*, 1999. 292(2): p. 195-202.

77. Buchan, D.W., F. Minneci, T.C. Nugent, K. Bryson, and D.T. Jones, Scalable web services for the PSIPRED Protein Analysis Workbench. *Nucleic Acids Research*, 2013. 41(Web Server issue): p. W349-57.

78. van den Bogaart, G., K. Meyenberg, U. Diederichsen, and R. Jahn, Phosphatidylinositol 4,5-bisphosphate increases Ca2+ affinity of synaptotagmin-1 by 40-fold. *J Biol Chem*, 2012. 287(20): p. 16447-53.

79. Chen, V.B., W.B. Arendall, 3rd, J.J. Headd, D.A. Keedy, R.M. Immormino, G.J. Kapral, L.W. Murray, J.S. Richardson, and D.C. Richardson, MolProbity: all-atom structure validation for macromolecular crystallography. *Acta Crystallogr D Biol Crystallogr*, 2010. 66(Pt 1): p. 12-21.

80. Barad, B.A., N. Echols, R.Y. Wang, Y. Cheng, F. DiMaio, P.D. Adams, and J.S. Fraser, EMRinger: side chain-directed model and map validation for 3D cryo-electron microscopy. *Nat Methods*, 2015. 12(10): p. 943-6.

81. Schrodinger, LLC, *The PyMOL Molecular Graphics System, Version 1.8*. 2015.

82. Bandell, M., A.E. Dubin, M.J. Petrus, A. Orth, J. Mathur, S.W. Hwang, and A. Patapoutian, High-throughput random mutagenesis screen reveals TRPM8 residues specifically required for activation by menthol. *Nature Neuroscience*, 2006. 9(4): p. 493-500.

83. Sun, J. and R. MacKinnon, Cryo-EM Structure of a KCNQ1/CaM Complex Reveals Insights into Congenital Long QT Syndrome. *Cell*, 2017. 169(6): p. 1042-1050 e9.

84. Zhang, H., L.C. Craciun, T. Mirshahi, T. Rohács, C.M.B. Lopes, T. Jin, and D.E. Logothetis, PIP2 Activates KCNQ Channels, and Its Hydrolysis Underlies Receptor-Mediated Inhibition of M Currents. *Neuron*, 2003. 37(6): p. 963-975.

85. Loussouarn, G., K.H. Park, C. Bellocq, I. Baro, F. Charpentier, and D. Escande, Phosphatidylinositol-4,5-bisphosphate, PIP2, controls KCNQ1/KCNE1 voltage-gated potassium channels: a functional homology between voltage-gated and inward rectifier K+ channels. *EMBO J*, 2003. 22(20): p. 5412-21.

86. Hilgemann, D.W., S. Feng, and C. Nasuhoglu, The Complex and Intriguing Lives of PIP2 with Ion Channels and Transporters. *Sci Signal.*, 2001. 2001(111): p. re19.

87. McLaughlin, S. and D. Murray, Plasma membrane phosphoinositide organization by protein electrostatics. *Nature*, 2005. 438: p. 605.

88. Laux, T., K. Fukami, M. Thelen, T. Golub, D. Frey, and P. Caronia, Gap43, Marcks, and Cap23 Modulate Pi(4,5p)2 at Plasmalemmal Rafts, and Regulate Cell Cortex Actin Dynamics through a Common Mechanism. *J. Cell Biol.*, 2000. 149(7): p. 1455-1472.

89. Veldhuis, N.A., D.P. Poole, M. Grace, P. McIntyre, and N.W. Bunnett, The G protein-coupled receptor-transient receptor potential channel axis: molecular insights for targeting disorders of sensation and inflammation. *Pharmacol Rev*, 2015. 67(1): p. 36-73.

90. Grycova, L., B. Holendova, Z. Lansky, L. Bumba, M. Jirku, K. Bousova, and J. Teisinger, Ca(2+) binding protein S100A1 competes with calmodulin and PIP2 for binding site on the C-terminus of the TPRV1 receptor. *ACS Chem Neurosci*, 2015. 6(3): p. 386-92.

91. Bae, C., C. Anselmi, J. Kalia, A. Jara-Oseguera, C.D. Schwieters, D. Krepkiy, C. Won Lee, E.H. Kim, J.I. Kim, J.D. Faraldo-Gomez, and K.J. Swartz, Structural insights into the mechanism of activation of the TRPV1 channel by a membrane-bound tarantula toxin. *Elife*, 2016. 5.

92. Halling, D.B., B.J. Liebeskind, A.W. Hall, and R.W. Aldrich, Conserved properties of individual Ca2+-binding sites in calmodulin. *Proc Natl Acad Sci U S A*, 2016. 113(9): p. E1216-25.

93. Singh, A.K., L.L. McGoldrick, E.C. Twomey, and A.I. Sobolevsky, Mechanism of calmodulin inactivation of the calcium-selective TRP channel TRPV6. *Sci Adv*, 2018. 4(8): p. eaau6088.

94. Kovalevskaya, N.V., M. van de Waterbeemd, F.M. Bokhovchuk, N. Bate, R.J. Bindels, J.G. Hoenderop, and G.W. Vuister, Structural analysis of calmodulin binding to ion channels demonstrates the role of its plasticity in regulation. *Pflugers Arch*, 2013. 465(11): p. 1507-19.

95. Di Scala, C., C.J. Baier, L.S. Evans, P.T.F. Williamson, J. Fantini, and F.J. Barrantes, Relevance of CARC and CRAC Cholesterol-Recognition Motifs in the Nicotinic Acetylcholine Receptor and Other Membrane-Bound Receptors. *Curr Top Membr*, 2017. 80: p. 3-23.

96. Fantini, J. and F.J. Barrantes, How cholesterol interacts with membrane proteins: an exploration of cholesterol-binding sites including CRAC, CARC, and tilted domains. *Frontiers in Physiology*, 2013. 4: p. 31.

97. Shuker, S.B., P.J. Hajduk, R.P. Meadows, and S.W. Fesik, Discovering High-Affinity Ligands for Proteins: SAR by NMR. *Science*, 1996. 274(5292): p. 1531-1534.

98. Yap, K.L., J. Kim, K. Truong, M. Sherman, T. Yuan, and M. Ikura, *Journal of Structural and Functional Genomics*, 2000. 1(1): p. 8-14.

99. Rhoads, A.R. and F. Friedberg, Sequence motifs for calmodulin recognition. *The FASEB Journal*, 1997. 11(5): p. 331-340.

100. Autzen, H.E., A.G. Myasnikov, M.G. Campbell, D. Asarnow, D. Julius, and Y. Cheng, Structure of the human TRPM4 ion channel in a lipid nanodisc. *Science*, 2018. 359(6372): p. 228-232.

101. Faouzi, M. and R. Penner, Trpm2. *Handb Exp Pharmacol*, 2014. 222: p. 403-26.

102. Hofmann, T., V. Chubanov, T. Gudermann, and C. Montell, TRPM5 Is a Voltage-Modulated and Ca2+-Activated Monovalent Selective Cation Channel. *Current Biology*, 2003. 13(13): p. 1153-1158.

103. McKemy, D.D., W.M. Neuhausser, and D. Julius, Identification of a cold receptor reveals a general role for TRP channels in thermosensation. *Nature*, 2002. 416(6876): p. 52-8.

104. van de Graaf, S.F., I. Boullart, J.G. Hoenderop, and R.J. Bindels, Regulation of the epithelial Ca2+ channels TRPV5 and TRPV6 by 1alpha,25-dihydroxy Vitamin D3 and dietary Ca2+. *The Journal of Steroid Biochemistry and Molecular Biology*, 2004. 89-90(1-5): p. 303-8.

105. Joo, K.W., U.S. Jeon, G.H. Kim, J. Park, Y.K. Oh, Y.S. Kim, C. Ahn, S. Kim, S.Y. Kim, J.S. Lee, and J.S. Han, Antidiuretic action of oxytocin is associated with increased urinary excretion of aquaporin-2. *Nephrology Dialysis Transplantation*, 2004. 19(10): p. 2480-6.

106. Sasaki, S., Is oxytocin a player in antidiuresis? *Journal of the American Society of Nephrology*, 2008. 19(2): p. 189-90.

107. Hirst, S.J., N. Alexander, H.S. McHaourab, and J. Meiler, RosettaEPR: an integrated tool for protein structure determination from sparse EPR data. *J Struct Biol*, 2011. 173(3): p. 506-14.

108. Alexander, N., M. Bortolus, A. Al-Mestarihi, H. McHaourab, and J. Meiler, De novo high-resolution protein structure determination from sparse spin-labeling EPR data. *Structure*, 2008. 16(2): p. 181-95.

109. Schwieters, C.D., G.A. Bermejo, and G.M. Clore, Xplor-NIH for molecular structure determination from NMR and other data sources. *Protein Sci*, 2018. 27(1): p. 26-40.

110. Raman, S., O.F. Lange, P. Rossi, M. Tyka, X. Wang, J. Aramini, G. Liu, T.A. Ramelot, A. Eletsky, T. Szyperski, M.A. Kennedy, J. Prestegard, G.T. Montelione, and D. Baker, NMR structure determination for larger proteins using backbone-only data. *Science*, 2010. 327(5968): p. 1014-8.

111. Leman, J.K., R. Mueller, M. Karakas, N. Woetzel, and J. Meiler, Simultaneous prediction of protein secondary structure and transmembrane spans. *Proteins*, 2013. 81(7): p. 1127-40.

112. Thompson, J.M., N.G. Sgourakis, G. Liu, P. Rossi, Y. Tang, J.L. Mills, T. Szyperski, G.T. Montelione, and D. Baker, Accurate protein structure modeling using sparse NMR data and homologous structure information. *Proc Natl Acad Sci U S A*, 2012. 109(25): p. 9875-80.

113. Mesleh, M.F., G. Veglia, T.M. DeSilva, F.M. Marassi, and S.J. Opella, Dipolar Waves as NMR Maps of Protein Structure. *Journal of the American Chemical Society*, 2002. 124(16): p. 4206-4207.

114. Leaver-Fay, A., M.J. O'Meara, M. Tyka, R. Jacak, Y. Song, E.H. Kellogg, J. Thompson, I.W. Davis, R.A. Pache, S. Lyskov, J.J. Gray, T. Kortemme, J.S. Richardson, J.J. Havranek, J. Snoeyink, D. Baker, and B. Kuhlman, Scientific benchmarks for guiding macromolecular energy function improvement. *Methods Enzymol*, 2013. 523: p. 109-43.

115. Minch, M.J., An Introduction to Hydrogen Bonding (Jeffrey, George A.). *Journal of Chemical Education*, 1999. 76(6).

116. Ovchinnikov, S., H. Park, D.E. Kim, F. DiMaio, and D. Baker, Protein structure prediction using Rosetta in CASP12. *Proteins*, 2018. 86 Suppl 1: p. 113-121.

117. Park, H., S. Ovchinnikov, D.E. Kim, F. DiMaio, and D. Baker, Protein homology model refinement by large-scale energy optimization. *Proc Natl Acad Sci U S A*, 2018. 115(12): p. 3054-3059.

118. Dolinsky, T.J., J.E. Nielsen, J.A. McCammon, and N.A. Baker, PDB2PQR: an automated pipeline for the setup of Poisson-Boltzmann electrostatics calculations. *Nucleic Acids Res*, 2004. 32(Web Server issue): p. W665-7.

119. Caterina, M.J., M.A. Schumacher, M. Tominaga, T.A. Rosen, J.D. Levine, and D. Julius, The capsaicin receptor: a heat-activated ion channel in the pain pathway. *Nature*, 1997. 389(6653): p. 816-24.

120. Tominaga, M., M.J. Caterina, A.B. Malmberg, T.A. Rosen, H. Gilbert, K. Skinner, B.E. Raumann, A.I. Basbaum, and D. Julius, The Cloned Capsaicin Receptor Integrates Multiple Pain-Producing Stimuli. *Neuron*, 1998. 21(3): p. 531-543.

121. Klein, R.M., C.A. Ufret-Vincenty, L. Hua, and S.E. Gordon, Determinants of molecular specificity in phosphoinositide regulation. Phosphatidylinositol (4,5)-bisphosphate (PI(4,5)P2) is the endogenous lipid regulating TRPV1. *J Biol Chem*, 2008. 283(38): p. 26208-16.

122. Julius, D., TRP channels and pain. *Annu. Rev. Cell. Dev. Biol.*, 2013. 29: p. 355-84.

123. Moran, M.M., M.A. McAlexander, T. Biro, and A. Szallasi, Transient receptor potential channels as therapeutic targets. *Nat Rev Drug Discov*, 2011. 10(8): p. 601-20.

124. Rudd, R.A., P. Seth, F. David, and L. Scholl, Increases in Drug and Opioid-Involved Overdose Deaths - United States, 2010-2015. *MMWR Morb Mortal Wkly Rep*, 2016. 65(5051): p. 1445-1452.

125. Razavi, R., Y. Chan, F.N. Afifiyan, X.J. Liu, X. Wan, J. Yantha, H. Tsui, L. Tang, S. Tsai, P. Santamaria, J.P. Driver, D. Serreze, M.W. Salter, and H.M. Dosch, TRPV1 sensory neurons control beta cell stress and islet inflammation in autoimmune diabetes. *Cell*, 2006. 127(6): p. 1123-35.

126. Stock, K., J. Kumar, M. Synowitz, S. Petrosino, R. Imperatore, E.S. Smith, P. Wend, B. Purfurst, U.A. Nuber, U. Gurok, V. Matyash, J.H. Walzlein, S.R. Chirasani, G. Dittmar, B.F. Cravatt, S. Momma, G.R. Lewin, A. Ligresti, L. De Petrocellis, L. Cristino, V. Di Marzo, H. Kettenmann, and R. Glass, Neural precursor cells induce cell death of high-grade astrocytomas through stimulation of TRPV1. *Nat. Med.*, 2012. 18(8): p. 1232-8.

127. Fernandes, E.S., L. Liang, S.J. Smillie, F. Kaiser, R. Purcell, D.W. Rivett, S. Alam, S. Howat, H. Collins, S.J. Thompson, J.E. Keeble, Y. Riffo-Vasquez, K.D. Bruce, and S.D. Brain, TRPV1 deletion enhances local inflammation and accelerates the onset of systemic inflammatory response syndrome. *J. Immunol.*, 2012. 188(11): p. 5741-51.

128. Riera, C.E., M.O. Huising, P. Follett, M. Leblanc, J. Halloran, R. Van Andel, C.D. de Magalhaes Filho, C. Merkwirth, and A. Dillin, TRPV1 pain receptors regulate longevity and metabolism by neuropeptide signaling. *Cell*, 2014. 157(5): p. 1023-36.

129. Lee, L.Y. and Q. Gu, Role of TRPV1 in inflammation-induced airway hypersensitivity. *Curr Opin Pharmacol*, 2009. 9(3): p. 243-9.

130. Mistretta, F., N.M. Buffi, G. Lughezzani, G. Lista, A. Larcher, N. Fossati, A. Abrate, P. Dell'Oglio, F. Montorsi, G. Guazzoni, and M. Lazzeri, Bladder cancer and urothelial impairment: the role of TRPV1 as potential drug target. *Biomed Res Int*, 2014. 2014: p. 987149.

131. Suri, A. and A. Szallasi, The emerging role of TRPV1 in diabetes and obesity. *Trends Pharmacol Sci*, 2008. 29(1): p. 29-36.

132. Motter, A.L. and G.P. Ahern, TRPV1-null mice are protected from diet-induced obesity. *FEBS Lett.*, 2008. 582(15): p. 2257-62.

133. Yang, F., X. Xiao, W. Cheng, W. Yang, P. Yu, Z. Song, V. Yarov-Yarovoy, and J. Zheng, Structural mechanism underlying capsaicin binding and activation of the TRPV1 ion channel. *Nat. Chem. Biol.*, 2015. 11(7): p. 518-24.

134. Voets, T., TRP channels and thermosensation. *Handb. Exp. Pharmacol.*, 2014. 223: p. 729-41.

135. Qu, X., M. Mayzel, J.F. Cai, Z. Chen, and V. Orekhov, Accelerated NMR spectroscopy with low-rank reconstruction. *Angew Chem Int Ed Engl*, 2015. 54(3): p. 852-4.

136. Findeisen, M., T. Brand, and S. Berger, A 1H-NMR thermometer suitable for cryoprobes. *Magnetic Resonance in Chemistry*, 2007. 45(2): p. 175-8.

137. Kontaxis, G., N. Müller, and H. Sterk, Cross correlation between dipolar and chemical-shift anisotropy interaction: Application to anisotropic rotational diffusion. *Journal of Magnetic Resonance (1969)*, 1991. 92(2): p. 332-341.

138. Goldman, M., Interference effects in the relaxation of a pair of unlike nuclei. *Journal of Magnetic Resonance (1969)*, 1984. 60(3): p. 437-452.

139. Renner, C. and T.A. Holak, Separation of anisotropy and exchange broadening using (15)N CSA-(15)N-(1)H dipole-dipole relaxation cross-correlation experiments. *J Magn Reson*, 2000. 145(2): p. 192-200.

140. Pervushin, K., R. Riek, G. Wider, and K. Wuthrich, Attenuated T2 relaxation by mutual cancellation of dipole-dipole coupling and chemical shift anisotropy indicates an avenue to NMR structures of very large biological macromolecules in solution. *Proceedings of the National Academy of Sciences*, 1997. 94(23): p. 12366-12371.

141. Lee, D., C. Hilty, G. Wider, and K. Wuthrich, Effective rotational correlation times of proteins from NMR relaxation interference. *Journal of Magnetic Resonance*, 2006. 178(1): p. 72-6.

142. Gautier, A., H.R. Mott, M.J. Bostock, J.P. Kirkpatrick, and D. Nietlispach, Structure determination of the seven-helix transmembrane receptor sensory rhodopsin II by solution NMR spectroscopy. *Nat Struct Mol Biol*, 2010. 17(6): p. 768-74.

143. Doyle, C.M., J.A. Rumfeldt, H.R. Broom, A. Sekhar, L.E. Kay, and E.M. Meiering, Concurrent Increases and Decreases in Local Stability and Conformational Heterogeneity in Cu, Zn Superoxide Dismutase Variants Revealed by Temperature-Dependence of Amide Chemical Shifts. *Biochemistry*, 2016. 55(9): p. 1346-61.

144. Yang, F., Y. Cui, K. Wang, and J. Zheng, Thermosensitive TRP channel pore turret is part of the temperature activation pathway. *Proc. Natl Acad. Sci. USA*, 2010. 107(15): p. 7083-8.

145. Yao, J., B. Liu, and F. Qin, Modular thermal sensors in temperature-gated transient receptor potential (TRP) channels. *Proc. Natl Acad. Sci. USA*, 2011. 108(27): p. 11109-14.

146. Liu, B., K. Hui, and F. Qin, Thermodynamics of Heat Activation of Single Capsaicin Ion Channels VR1. *Biophysical Journal*, 2003. 85(5): p. 2988-3006.

147. Chowdhury, S., B.W. Jarecki, and B. Chanda, A molecular framework for temperature-dependent gating of ion channels. *Cell*, 2014. 158(5): p. 1148-58.

148. Baxter, N.J., L.L. Hosszu, J.P. Waltho, and M.P. Williamson, Characterisation of low free-energy excited states of folded proteins. *J Mol Biol*, 1998. 284(5): p. 1625-39.

149. Williamson, M.P., Many residues in cytochrome c populate alternative states under equilibrium conditions. *Proteins*, 2003. 53(3): p. 731-9.

150. Gao, Y., E. Cao, D. Julius, and Y. Cheng, TRPV1 structures in nanodiscs reveal mechanisms of ligand and lipid action. *Nature*, 2016. 534(7607): p. 347-51.

151. Gavva, N.R., L. Klionsky, Y. Qu, L. Shi, R. Tamir, S. Edenson, T.J. Zhang, V.N. Viswanadhan, A. Toth, L.V. Pearce, T.W. Vanderah, F. Porreca, P.M. Blumberg, J. Lile, Y. Sun, K. Wild, J.C. Louis, and J.J. Treanor, Molecular determinants of vanilloid sensitivity in TRPV1. *J. Biol. Chem.*, 2004. 279(19): p. 20283-95.

152. Elokely, K., P. Velisetty, L. Delemotte, E. Palovcak, M.L. Klein, T. Rohacs, and V. Carnevale, Understanding TRPV1 activation by ligands: Insights from the binding modes of capsaicin and resiniferatoxin. *Proc Natl Acad Sci U S A*, 2016. 113(2): p. E137-45.

153. Wang, J., A. Arbuzova, G. Hangyas-Mihalyne, and S. McLaughlin, The effector domain of myristoylated alanine-rich C kinase substrate binds strongly to phosphatidylinositol 4,5-bisphosphate. *Journal of Biological Chemistry*, 2001. 276(7): p. 5012-9.

154. Reid, G. and M.-L. Flonta, Ion channels activated by cold and menthol in cultured rat dorsal root ganglion neurones. *Neuroscience Letters*, 2002. 324(2): p. 164-168.

155. Mittermaier, A.K. and L.E. Kay, Observing biological dynamics at atomic resolution using NMR. *Trends Biochem Sci*, 2009. 34(12): p. 601-11.

APPENDIX A

PERMISSION STATEMENTS FROM CO-AUTHORS

Permission for including co-authored material in this dissertation was obtained from co-authors, Minjoo Kim.